VUV Emission and Absorption Spectroscopy with a Multichannel Near Normal Incidence Spectrometer

A thesis for the degree of Master of Science

submitted to

Centre for Laser Plasma Research
School of Physical Sciences

DUBLIN CITY
UNIVERSITY
Ollscoil Chathair Bhaile Átha Cliath

by

Lee J. Dardis B.Sc.

Research Supervisor

Dr. John Costello

July 1998.

I hereby certify that the material, which I now submit for assessment on the programme of study leading to the award of Mater of Science is entirely my own work and has not been taken from the work of others save and to the extent that such work has been cited and acknowledged within the text of my own work

Signed :   *Lee Dardis*

L J Dardis

Date :   30|3|13

ID number   95970649

Table of contents

Acknowledgements.

Abstract

An experiment for vacuum UV emission and photoabsorption spectroscopy using a normal incidence multi-channel spectrometer is described Two detection configurations were used in the experiments, one a Channel Electron Multiplier Array with Photo Diode Array readout (CEMA / PDA), the other a directly illuminated back thinned Charge Coupled Device (CCD)

Emission spectra of plasmas of a number of low and high Z target materials were recorded covering the majority of the vacuum UV spectral region (35 to 200 nm) These experiments were designed mainly to study the nature of the emission (line versus continuum) and it's dependence on atomic number The use of two detection configurations allowed for inter comparisons to be made on resolution, efficiency and dynamic range of the two multi-channel detector and spectrometer systems

Experiments were also performed on photoabsorption by helium gas The spectra thus obtained were used to help characterise the system's application to absorption studies around the He principal series limit at ~ 50 43 nm

In addition, for the first time the instrument was used to study photoabsorption using the dual laser plasma technique (DLP) Results on the relative photoabsorption cross sections of barium and barium ions using a samarium continuum back-light are presented which indicate that the instrument is well suited to absorption experiments in the range of 35 to 80 nm where second order of the continuum is mainly absent and the grating is being used close to it's blaze wavelength (80 nm)

Finally, the work concludes with details on the design, construction and preliminary testing of a vacuum-optical beamline which should both improve the aperture matching ability of the instrument and allow spatially resolved studies of the laser plasma light source to be made The spectrometer with the additional spherical mirror was modelled by means of simple geometric optic calculations as well as with ray tracing software in order to estimate improvements in throughput

The following chapter outlines the general properties of plasmas The focus of this chapter is on laser-produced plasmas, their evolution and a number of the main atomic processes dictating their behaviour The laser plasma as a light source for spectroscopy and most especially as a continuum light source for photoabsorption studies is discussed Other applications to date of laser produced continua in e g , photoelectron spectroscopy are listed

1.1   Introduction to laser produced plasmas

A plasma is a quasi-neutral gas of charged and neutral particles Plasmas are dynamic systems for which restoration of neutrality is the dominant physical process A plasma is said to exhibit collective behaviour, i e particles in a plasma which are charged will interact by the Coulomb force [Carroll et al, 1981] Plasmas can be formed by any method that can couple enough energy into a material to permit ionization of the atoms and continue this input of energy to overcome the natural recombination process that occurs thereafter One method of plasma creation involves the use of intense laser light interacting with a material, a so-called laser produced plasma

When a high power pulsed laser is focused to an irradiance of greater than 10^8 W cm ^{2} onto a solid material, a short duration, high density and high temperature plasma is formed The ability to provide a controlled environment for the study of ionized species is principally the reason why the laser produced plasma has been extensively used in atomic spectroscopy The laser plasma allows for highly ionized atomic species and refractory elements to be studied, something which is not readily possible with other methods [Costello et al, 1991] Ion densities of $10^{15} - 10^{18}$ cm ^{3} and effective temperatures in the range of 10 eV - 1 keV (1 eV $\equiv$ 11605 K) are readily achieved with table top lasers At such temperatures, laser plasmas emit copious amounts of vacuum UV (VUV) and extreme UV (XUV) radiation with a duration comparable to that of the exciting laser pulse The following sections outline the initiation and evolution of laser produced plasmas and discusses some of the physical processes occurring within the plasma plume

For collective behaviour to dominate in a plasma, the extent of the Coulomb force on an ionized species must be comparable to the extent of the plasma A parameter that quantifies the effective extent of the Coulomb force around a charged species is the Debye length λ_{Debye} (m) It can also be viewed as a measure of the shielding effect of the species surrounding a charged particle Using Poisson's equation and the fact that the distribution of energies of the plasma species can be modelled by a Boltzmann distribution, it can be shown that,

$$\lambda_{Debye} = \left(\frac{\varepsilon_0 k_B T}{n_e e^2} \right)^{1/2} \qquad \text{(SI units)} \qquad \text{[E 1-1]}$$

where T (K) is the electron temperature, n_e (m^3) is the electron number density, e (C) is the charge on the electron, k_B (J K^1) is Boltzmann's constant and ε_0 (8 8542 * 10^{12} F m^1) is the electric permittivity of free space [Hughes, 1975]

When the Debye length is comparable to the size of the plasma, collective behaviour results in the plasma exhibiting oscillations at some frequency ω_{plasma} (radians s^1) such that,

$$\omega_{plasma} = \left(\frac{n_e e^2}{m_e \varepsilon_0} \right)^{1/2} \qquad \text{(SI units)} \qquad \text{[E 1-2]}$$

where m_e (kg) is the mass of an electron [Hughes, 1975] Similarly, the various ion stages have their own associated frequencies These natural frequencies determine the response of the plasma to radiation incident on it

The dispersion relation for electromagnetic waves travelling through a plasma is given by,

$$\omega^2 = \omega_{plasma}^2 + c^2 k^2 \qquad \text{[E 1-3]}$$

where c (m s^1) is the speed of light in vacuum, and k (k = n-ik, where n and k being the optical constants of the material in question) is the propagation constant describing the materials effect on electromagnetic waves and is in general an

2

imaginary number. Considering the case were $\omega_{plasma} < \omega$, k has a zero imaginary component which results in the electromagnetic wave propagating without losses (ignoring other absorption effects). When $\omega_{plasma} > \omega$, k has a non-zero imaginary component and thus the electromagnetic wave does not propagate and is reflected by the medium. The electron density when $\omega_{plasma} = \omega$ has reached the critical density at which the electromagnetic wave is reflected back from the plasma.

$$n_{critical} = \left(\frac{\varepsilon_0 m_e \omega^2}{e^2} \right) \qquad \text{(SI units)} \qquad \text{[E 1-4]}$$

1.2 Evolution of laser produced plasmas.

The initial stages of plasma formation differ for the case of conductors and insulators. When the electromagnetic field of laser radiation impinges on a metallic target surface, it penetrates only to a very small depth. This is commonly referred to as the skin depth ∂ (m) and has a magnitude, which is a fraction of the wavelength λ (m) being used.

$$\partial = \sqrt{\left(\frac{\pi c \mu_0 \sigma}{\lambda} \right)} \qquad \text{(SI units)} \qquad \text{[E 1-5]}$$

Where μ_0 ($4\pi * 10^{-7}$ H m^{-1}) is the permeability of free space and σ (Ω^{-1} m^{-1}) is the material's electrical conductivity. The strength of the electric field is such that it interacts with the target material's free electrons and in turn heating, evaporation and vaporisation occur rapidly. The plasma thus formed is relatively cold at this stage and in the shape of a thin sheet close to the target's surface. The root mean square (r.m.s.) electric field E (V m^{-1}) is related to the irradiance ϕ (W m^{-2}) by the following relationship.

$$E_{rms} \cong 19.4\sqrt{\phi} \qquad \text{(SI units)} \qquad \text{[E 1-6]}$$

In the case of insulators, the laser photon energy is lower than the ionization potential of the material. Despite this, free electrons can be produced by e.g., multi-photon ionization. Furthermore, easily ionized and free electrons exist at defects and impurities and ionization may proceed via other non-linear effects e.g. Stimulated

3

Brillouin Scattering (SBS) Once free electrons are produced by whatever
generation process, laser radiation is efficiently absorbed and a thin plasma sheet
forms

Following this priming stage, absorption of the laser light by inverse
bremsstrahlung[†] occurs This is a process whereby a photon is absorbed by an
electron in the presence of a neutral atom / ion resulting in the electron being raised
from a lower continuum level to a higher one, thereby increasing it's kinetic energy
Inverse bremsstrahlung provides the dominant process for laser light absorption

In a laser produced plasma an electron density gradient exists and therefore
the plasma frequency as given by [E 1-4] is also a function of position within the
plasma When the incident laser radiation reaches the region in the plasma plume
where $n_e = n_{critical}$, it is reflected back towards the laser At this point, the radiation is
no longer reaching the target surface and therefore plasma production stops Because
the existing plasma material is been continuously driven away from the target surface
the density gradient will reduce to a level were the laser radiation can again reach the
target's surface This process repeats itself for the duration of the laser pulse After
the termination of the excitation laser pulse the plasma continues to expand outwards
away from the target surface adiabatically and cools rapidly

1.3   Atomic processes in plasmas

In a typical plasma, the range of neutral and ionized species present results in
a large number of possible interactions Quite often, when considering specific
plasmas, a small number of these interactions provide the dominant mechanisms for
energy losses and gains One property, which makes the modelling of such a system
easier, is the fact that in many laboratory plasmas, local thermodynamic equilibrium
(LTE) prevails where collisional excitation and ionization are balanced by their
inverse processes – namely, collisional decay and recombination and are the
dominant processes within the plasma In laser plasmas with intermediate electron
densities (typically $n_e < 10^{20}$ cm^3), in general the system is better represented by the

---

[†] Bremsstrahlung German word for 'breaking radiation'

4

collisional-radiative (CR) equilibrium model [Colombant and Tonon, 1973] The relative significance of particular processes resulting in radiative cooling of a plasma plume is strongly dependent on the atomic number of the target material as well as degree of ionization of the plasma These processes can be grouped together into three main groups, bound-bound transitions, bound-free transitions and free-free transitions Each of these occurs with the difference in energy being compensated by a collision or a photon event Only photon generating and loss events are considered in the following discussion   ,

As already stated inverse-bremsstrahlung provides the dominant mechanism in the evolution and growth of a plasma It's inverse process i e bremsstrahlung is important because it is one important mechanism by which continuum emission results Bremsstrahlung refers to the process whereby an electron makes a transition from a higher free electron energy state to a lower one, with the emission of a photon of energy equal to the difference between the two energy levels [E 1-7] The important interactions are those, which occur between electrons and ions, since those between electron-electron and electron-neutral species, do not provide an effective conversion of electron kinetic energy to continuum emission

$$X^{n+} + e^{-}(T_1) \Leftrightarrow X^{n+} + e^{-}(T_2) + h\nu_{continuous} \qquad T_1 > T_2 \qquad [E 1-7]$$

One of the most important processes, which takes place in plasmas – at least in spectroscopic studies – is radiative recombination and it's inverse process of photo-ionization In radiative recombination, the electron recombines with an ion with the emission of a photon possessing energy equal to the energy difference between the initial and final states These processes can occur in single as well as in multiple steps The resulting emission or absorption spectrum has a continuum appearance with a fairly sharp low-frequency cut-off This cut-off is known as the recombination limit, and is the minimum energy required to ionize the atom from the bound state Recombination radiation is generally the dominant mechanism for continuum emission A single step photoionization process (proceeding from left to right) / radiative recombination process (proceeding from right to left) is represented by

$$X^{n+} + h\nu_{continuous} \Leftrightarrow X^{(n+1)+} + e^{-} \qquad [\text{ E 1-8 }]$$
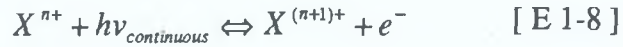
Another process that is of interest in the area of spectroscopy, is photo-excitation and it's inverse process of photo-de-excitation. In this process, an electron makes a transition from a lower bound state to an upper bound state with the absorption of a photon. The resulting spectrum exhibits line structure. In the absence of perturbations the transitions gives rise to a spectral line whose profile depends upon the spontaneous lifetime of the upper state, and on the distribution of velocities of the emitting atoms, which causes a distribution of Doppler shifts. Collisions, electric and magnetic fields all perturb the initial and final states of the emitting atom and the resulting spectral line profile therefore contains valuable information on the conditions within the plasma [Hughes, 1975].

$$h\nu_{line} + X \Leftrightarrow X^{*} \qquad [\text{ E 1-9 }]$$

1.4 Laser produced plasma light sources.

Shortly after the development of the Ruby laser by Maiman [1960] the study of intense laser–matter interaction was born. Early measurements of the spectra emitted by laser produced plasmas showed them to be intense sources of both line [Fawcett *et al,* 1966] and continuum emission [Ehler and Weissler, 1966]. Since then, laser produced plasmas have proven themselves to be both efficient and versatile sources for the study of emission and absorption spectroscopy of highly ionized atoms.

1.4.1 Line emission dominated plasmas.

Spectra of elements in the periodic table lighter than iron and nickel were the focus of special attention during the 1960's and 1970's, the two decades when most of the analysis of the solar spectrum retrieved by space based instruments took place. This was due to the fact that these studies displayed previously unidentified lines which could only be explained by higher ion stages being present in the sun's corona. These new observations motivated studies of higher ion stages along iso-electronic sequences in these lighter elements. Experiments on fusion necessitated studies being

6

formed on the heavier elements in the periodic table Impurity elements in tokamak[†] plasmas resulted in characteristic spectra, which proved to be a useful diagnostic for the estimation of electron densities and temperatures in these plasmas

Line dominated emission from plasmas are important for the following reasons

- They provide a testing ground for theoretical calculations
- They increase our understanding of atomic structure
- In addition, they provide a diagnostic tool for the measurement of plasma parameters, i e temperatures and densities etc

Laser produced plasmas are thus a useful laboratory light source in which the ionization distribution may be somewhat tuned by adjusting the on target irradiance It is well known that both ion stage distribution and the average electron temperature T_e (eV) are dependant on the target irradiance ϕ (W cm^2)

The average electron temperature for incompletely ionized targets of medium to high atomic number elements can be approximated by,

$$T_e = 5\ 2*10^{-6} Z^{1/5} (\lambda^2 \phi)^{3/5} \qquad 10^{11} \geq \phi \geq 10^{13}\ \mathrm{W\ cm}^2 \qquad [\ E\ 1\text{-}10\ ]$$

where λ (μm) is the wavelength of the excitation laser and Z is the atomic number of the parent material [Colombant and Tonon, 1973] This approximation follows from the application of the collisional-radiative (CR) model to laser produced plasmas

Using [E 1-8] the average ion stage can be approximated to,

$$Z \cong \tfrac{2}{3}(AT_e)^{1/3} \qquad T_e \geq 30\ \mathrm{eV} \qquad [\ E\ 1\text{-}11\ ]$$

[†] Tokamak fusion devices rely on the magnetic confinement of a high temperature plasma in a 'doughnut' shape vessel They represent one potential method for the implementation of a fusion energy source

7

where A (a m u) is the atomic mass number of the parent material and T_e (eV) is the average electron temperature [Colombant and Tonon, 1973] If a Nd   YAG laser (λ = 1064 nm) is focused onto aluminium to an irradiance of ~ 10^{12} W cm^2, the average electron temperature (T_e) would be ~ 142 eV The plasma thus formed would contain aluminium ions with an average ion stage of ~ 10 times ionized

It is also well known that the ionization distribution varies with time (i e plasma cools and recombination takes place) Hence by incorporating both time and space resolution in a spectrometer system it is possible to choose, to a reasonably high degree of selectivity, a single ion stage [Costello *et al*, 1991]

1 4 2   Continuum emission dominated plasmas

The line-free continuum emission from a laser produced plasma was first observed and noted by Ehler and Weissler [1966] In these studies a 0 4 J Q-switched Ruby laser was focussed onto a tantalum (Z = 73) target with a pulse duration of ~ 40 ns Both a 0 5 metre normal incidence and a 2 0 metre grazing incidence spectrometer were used to record the resulting emission spectra therefore giving a combined wavelength range between 5 and 400 nm with some overlap between the two instruments A broad band continuum was observed with two principal intensity maxima (at ~ 170 nm and ~ 50 nm) Other high atomic number targets, tungsten (Z = 74) and platinum (Z = 78), were also studied in terms of their emission spectra, and these showed similar line free continua with some small line structure being present on the platinum spectra at ~ 25 nm

The use of rare-earth elements for generation of continua was first reported by Carroll *et al* [1978, 1980] In these investigations, the authors noted that with appropriate targets, laser-produced plasmas can provide clean essentially 'line-free' continua suitable for photoabsorption experiments in the range 4 – 200 nm The rare-earth elements investigated were the group from samarium to ytterbium It was observed that continua from these elements had time duration's which were essentially the same as the excitation laser source (in this case a Q-switched Ruby laser with pulse duration ~ 25 ns) in the XUV region and rising to in excess of 100 ns in the VUV normal incidence region

8

O'Sullivan et al [1982] did further work on the absolute spectral irradiances of laser-produced continua in the range 115 to 200 nm This work showed that the reproducibility of the continuum was as good as or better than the reproducibility of the excitation laser (typically better than 5 %)

In recent years, a lot of interest in laser produced plasmas has been focussed on the generation of ultra short pulses of continuum light These studies have been motivated by the possibility of generating short duration x-ray pulses for pumping short wavelength lasers and for time-resolved studies of materials In work performed by Meighan et al [1997] using 'tabletop' lasers, 'line-free' continuum emission in the XUV was observed from laser produced plasmas of high atomic number elements The targets were irradiated by 248 nm laser pulses of 7 ps (FWHM) duration at a power density of $\sim 10^{13}$ W cm^{2} A streak camera with a time resolution of $\sim$ 100 ps recorded the resulting XUV emission Both the coupling optics and the Mylar$^{®}$ thin film filter used yielded an instrument bandpass of 85 eV centred at 145 eV Results on the broadband XUV emission from a lead plasma yielded an upper limit of FWHM of $\sim$ 750 ps More recent experiments [Meighan et al, 1998] have shown that XUV pulse durations of 100 to 200 ps can be obtained

It is well established that the presence of a weak pre-plasma either formed by an actual pre-pulse or by ASE can dramatically increase the VUV and x-ray emission from the main plasma [Tom and Wood, 1988, Cobble et al, 1991 and Theobald et al, 1994] The main laser pulse interacts with a gaseous plasma instead of the solid target material and so the interaction volume within the short duration laser main pulse is larger in the former case The interaction with the plasma, i e the absorption of laser radiation, the rate of the various atomic relaxation processes, and therefore the plasma emission will change with the changing interaction volume [Steingruber et al, 1996, Teubner et al, 1992, and Kieffer and Chaker, 1994]

1.4.3 The origin of rare-earth continua.

The extent and 'line-free' content of the continuum emission from rare-earth plasmas stems from three processes, recombination radiation, bremstrahlung radiation and unresolved line radiation The relative contribution to the continua from each of these three principal sources depends on the degree of ionization of the plasma as well as the atomic number of the parent material The recombination component of the continuum scales as $\xi^4_{average}$, while the bremstrahlung component scales with $\xi^2_{average}$ where $\xi_{average}$ is the average ion stage which is present in the plasma [O'Sullivan, 1983] When the plasma is sufficiently hot (electron temperatures greater than ~ 50 eV) most of the outer electrons have been stripped away from the atoms and therefore recombination radiation will provide the dominant continuum emission process in the XUV In contrast, bremstrahlung contributes a relatively small amount (~ 20 %) to the overall continuum intensity making it's greatest contribution at longer wavelengths (i e VUV) and generally lower ion stages i e cooler plasmas

However, the latter discussion does not explain the key aspect of the contmuum i e the lack of any significant structure due to discrete transitions within the distribution of ions in the plasma even at high resolution studies [Gohill et al, 1986], [Orth et al, 1986] ($\Delta\lambda$ = ~ 0 05 nm in both cases) The elements which proceed the rare-earth's and those immediately after show strong line emission and therefore factors must exist other than the large atomic number and highly charged species present which contributes to pure contmuum emission from these rare-earth plasmas In order to understand this observation one must consider the following argument

In low ion stages of the elements $62 \leq Z \leq 74$ (samarium to tungsten) the 5s and 5p sub-shells are filled while the occupancy of the 4f sub-shell varies with atomic number and ion stage With increasing ionization the binding energy of 4f electrons increases more rapidly than that of 5s or 5p electrons so that 4f / 5p level crossing occurs at about six times ionized species and 4f / 5s at about twelve times ionized species Consequently all the elements of interest contain 4f electrons in the ground state for each ion stage generated in the laser plasmas under discussion here [

Carroll and O'Sullivan, 1982] It is the presence of f electrons in both the upper and lower states involved which give rise to very large number of lines which are generally not possible to resolve (hence the term 'Un-resolved Transition Array' or UTA)
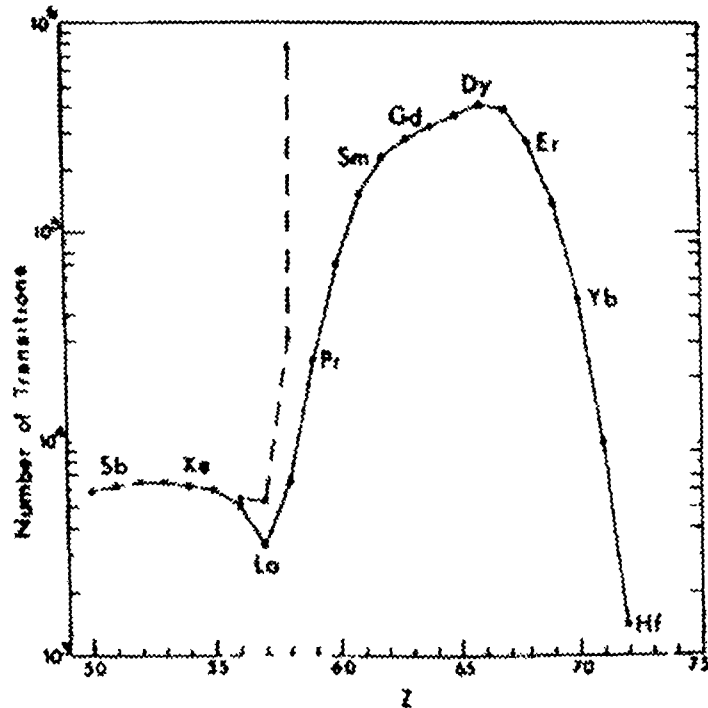
Figure 1-1   Total number of lines in LS coupling predicted for 4d-4f transitions in the rare-earth and immediately proceeding elements Broken curve, number of predicted lines when (4f, 5p) and (4f, 5s) degeneracy is included [Carroll and O'Sullivan, 1982]

The proximity of 4f, 5s and 5p binding energies gives rise to a band of overlapping complex configurations with variable numbers of 4f, 5s and 5p electrons Furthermore, if the plasma is optically thick (e g pure metal plasma) then the photoabsorption cross sections for these more intense lines will be greater and so the lines will be attenuated and merge into the underlying continuum [Carroll and O'Sullivan, 1981]

From this brief qualitative analysis, it can be seen that the continuum from rare-earth elements under the conditions normally present in a laser produced plasma is not the result of pure bremstrahlung and recombination processes but that it

contains a very large number of possible transitions which give the appearance of a pure continuum band even at high spectral resolution The presence of a few lines on the spectra (mostly at wavelengths greater than ~ 100 nm) of the rare-earth's is due to simpler electronic configurations m low ion stages and / or a configuration from which only a very small number of permitted transitions are allowed (e g $4d^{10}$ (^{1}S)$\rightarrow$ $4d^9$nl (^{1}P) arrays, see figure 1-2 and 1-3)

The extent of the continuum and position of the characteristic lines have been illustrated in figure 1-2 by O'Sullivan [1983] and summarises work done by Carroll *et al* [1980] on continuum emission of elements $62 \leq Z \leq 74$ in the wavelength range of 200 to 4 nm

It can be seen that a number of trends are evident Considering the long wavelength portion of the figure 1-2, two principal sets of characteristic lines appear superimposed on the continuum The first of these sets located at ~ 100 nm gradually increases in both intensity and extent as the atomic number of the target material increases The other set of lines located at wavelengths greater than ~ 180 nm for samarium rapidly moves to shorter wavelengths as the atomic number of the target material increases and overtakes the 100 nm group at the element ytterbium In tungsten this latter group is evident at wavelengths greater than ~ 12 5 nm
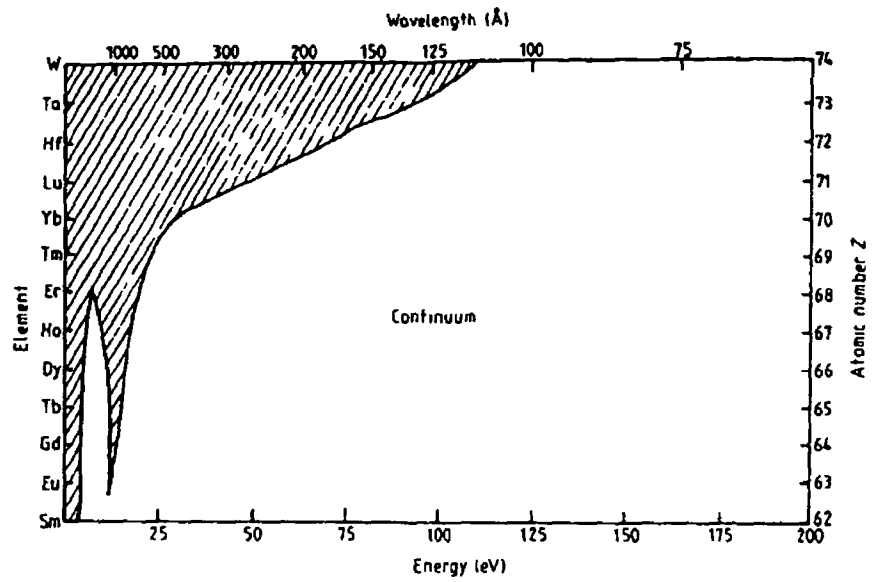
Figure 1-2   Extent of the continuum emission as a function of Z, the atomic number It should be noted that most of the line emission from ion stages with $\xi \leq 6$ and can be eliminated by increasing the plasma temperature The shaded region denotes line emission present The resulting power density at focus was estimated by consideration of the abundance of ion stages to be $\sim 2 * 10^{11}$ W cm^2 [O'Sullivan, 1983]
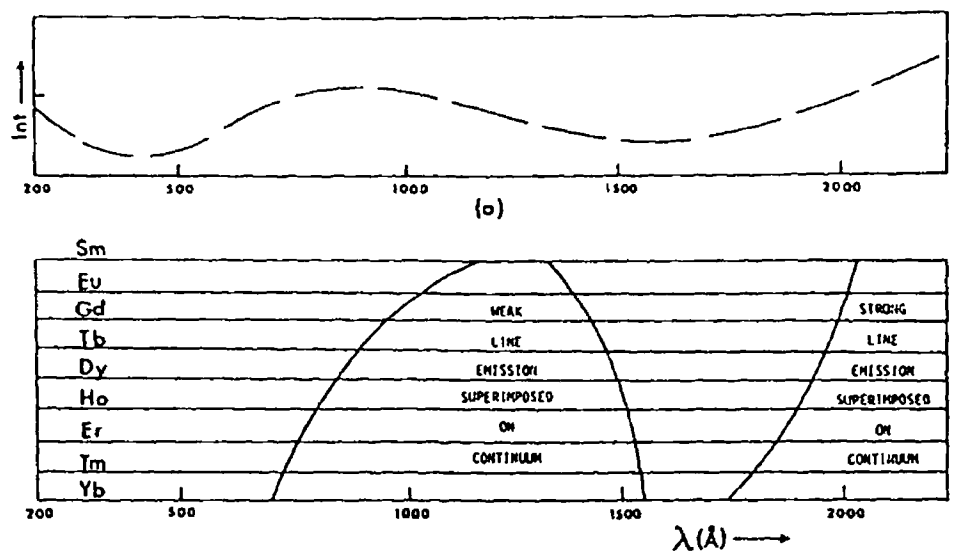
Figure 1-3   (a) Approximate intensity distribution in rare earth continuum (samarium Z = 62 to ytterbium Z = 70) in the 20 to 200 nm region (b) Region where line emission is superimposed on rare earth continuum. Lines in central region are relatively weak and scarcely effect the continuum character of the emission even at moderate dispersion i e 0 12 nm mm^{1} [Carroll et al, 1980]

13

1.5   Other applications of laser-produced continua.

The laser plasma light source has proven itself efficient in the production of continuum radiation A distinction between applications requiring broadband contmua and those requiring narrow band XUV or VUV continua can be made Laser produced plasma light sources for proximity lithography require narrow band continua above the silicon K-edge (~ 0 674 nm) but of short enough wavelength for efficient absorption by the photo-resist (i e generally between ~ 1 0 and ~ 1 4 nm) [Celliers *et al*, 1995] Therefore choice of targets here generally include L-shell emitters such as Ne-like ions (Fe, $Z = 26$, Co, $Z = 27$, Cu, $Z = 28$, Zn, $Z = 29$) or M-shell emitters such as Ni-like ions (Xe, $Z = 54$) On the other hand XUV sources needed for microscopy require narrow band emission confined to the water window (4 376 nm to 2 332 nm)[†] In this case, sources using target materials such as silicon ($Z = 14$) or carbon ($Z = 6$) are generally used Some applications requiring broadband continua and using rare-earth elements are briefly discussed below

1 5 1   VUV reflectivity measurements

The study of the interaction of light with a material has long been recognised as a fundamental method of determining the electronic structure of mater The number of applications requiring efficient optics for the low wavelength regime is increasing and therefore accurate determinations of the optical constants across the entire range from x-rays to VUV is important The optical constants are macroscopic quantities, which describe the electrical permittivity of the medium One of the techniques of determining the optical constants from raw reflection data is by use of the Kramers Kronig integrals A prerequisite of an accurate Kramers Kronig analysis is the possession of reflectivity data over a wide spectral range

In work performed by French *et al* [1989], a cylindrical samarium target

---

[†] The water window Wavelength region between the K absorption edges of carbon (4 376 nm) and oxygen (2 332 nm) In this range the contrast between a biological sample and the surrounding water is high

($Z = 62$) was illuminated by a focussed 500 mJ, 8 ns (FWHM) Nd YAG laser operating at a repetition frequency of a 20 Hz The focused laser had an estimated spot size of ~ 100 μm m diameter corresponding to an irradiance of approximately 10^{12} W cm^2 The VUV light from the laser-produced plasma was focused by a spherical mirror onto either a sample surface or an iridium reference mirror The spot size of this focused broad band VUV light was estimated to be 3 mm in diameter A normal incidence spectrometer utilising an 1800 lines mm^{-1} grating was used to observe the reflected light in the region of 5 to 40 eV The use of the iridium reference mirror allowed for the absolute reflectivity of the samples to be measured with a quoted accuracy of ~ 5 % A Kramers Kronig analysis of this reflection data yielded values for the optical constants for the samples under consideration

1 5 2 VUV radiative transfer standards.

Radiometric standards can be classified as those sources of calculable spectral radiant power – primary standards, and those sources with stable spectral radiant power, which can be controlled by a few source parameters These latter sources are calibrated against primary standards and serve as transfer source standards – secondary source standards [Kuhne and Wende, 1985]

Radiometric techniques for wavelengths are well established with calibrated transfer sources for $\lambda \geq 100$ nm and transfer detectors for $\lambda \leq 5$ nm Below ~ 100 nm, however, in general the problem of accurately determining spectral radiant quantities of sources, e g radiance (W m^2 sr^1) and spectral radiance (W m^2 sr^1 nm^1) is not yet well solved Detectors with known sensitivity can only be used for measuring the spectral radiance of sources if the spectral transmittance of the instrument has accurately been measured Ideally, the instrument should be calibrated by use of a primary source standard such as light from a synchrotron insertion device, which has been passed through an accurately calibrated monochromator Unfortunately, this is not always possible for such reasons such as cost and convenience Also, optical instruments degrade with time due to contamination of reflecting surfaces and detectors and therefore the ability to calibrate the instrument in-situ would be a great advantage [Bibinov et al, 1997]

Laser produced plasmas serve as effective sources for XUV and VUV radiative transfer standards The emission is both intense (typically 10^{23} photons $cm^{-2} sr^{-1} s^{-1} nm^{-1}$ @ 120 nm) and reproducible (better than 5 % typically) [Carroll *et al*, 1983] The fact that this radiometric standard uses a source, which is both small and simple to implement means that it can offer a non-obtrusive *in-situ* means of calibration in various plasma experiments

1.5 3   VUV photoelectron spectroscopy

Laser-produced plasmas have recently been used as an alternative to synchrotron based sources for x-ray photoelectron spectroscopy (XPS)[†] Research in Japan by Ohchi et al [1996] has shown promising results using a grazing incidence based monochromator with toroidal optics combined with a Wolter mirror[‡] in the study of laser ablated silicon surface using photoelectron spectroscopy To detect the energy of the photo-generated electrons a hemispherical electron energy analyzer was used A pinhole between the monochromator and the Wolter mirror was used in order to select the x-rays with wavelength of 5 24 nm The Wolter mirror was designed and positioned to demagnify the monochromatized x-ray source to 1/32 With a pinhole diameter of 500 μm, it resulted in a spot size of approximately 20 μm in diameter Photoelectrons from the sample were collected by a retarding lens, analyzed by a hemispherical electrostatic electron analyzer and detected by a position-sensitive MCP The energy resolution of the analyzer was estimated to be ~ 2 eV

1 6   Advantages of laser produced plasma continuum light sources

The inherent properties of rare-earth plasma continua are important considerations when choosing an ideal light source for an application There are certainly disadvantages as with any source but by careful attention to system design and geometry some of these can be reduced to an acceptable level, i e uniformity of

---

[†] XPS is a technique used to measure the energy distribution of surface electrons

[‡] Wolter mirrors, which were originally developed in 1952, use the principle of grazing incidence to achieve focusing of x-rays The internal surface of a partial parabola – with central axis symmetry - is used as the reflecting surface

emission, shot to shot reproducibility etc The basic property of being 'tabletop' means that some of these disadvantages are much reduced when considering cost, size and commercial availability of complete set-ups In applications requiring an unpolarized source of XUV and VUV radiation with high single shot brightness, a laser plasma continuum source is ideal [Costello *et al*, 1991] Where polarization is critical, a high degree of polarized XUV can be obtained by using a 45° multilayer reflectors

1 6 1 High spectral irradiance

An important parameter of light sources of all types is the spectral radiance per pulse and can be expressed in units of photons $cm^2 \, sr^1 \, nm^1 \, s^1$ This summarises a number of properties such as intensity, directionality and spectral content Whereas the peak x-ray irradiance from laser driven plasma source can be up to 4 orders of magnitude higher than that of synchrotron light sources and have a duration up to 200 times longer, the repetition frequency is much lower, typically 4 to 5 orders of magnitude [Costello *et al*, 1991] This reduces the average power of the LPP source which (even at a repetition rate of 100 Hz) can be lower than bending magnet beam lines and orders of magnitude below insertion devices Further, the LPP is a point source while light from say an insertion device is collimated The laser produced plasma continuum has a peak spectral irradiance per pulse which is a factor of 10^3 higher than that of the B-R-V (Ballofet-Romand-Vodar)[†] source [Ballofet *et al*, 1961] which was one of the few laboratory continuum sources available before the advent of the laser produced plasma light source [Carroll *et al*, 1980]

1 6 2 Low line structure content and good reproducibility

The ideal contmuum light source for spectroscopic studies would be a uniform point source and would have a broad band continuum spectral content and would be perfectly reproducible from shot to shot The laser plasma continuum meets somewhat with this ideal if the target is chosen and prepared carefully Work has

---

[†] The original B-R-V source consists of three electrodes – one of which is of material with high atomic number - separated by a small distance in a vacuum A high voltage stored in capacitor is discharged across the intervening gap between the electrodes thus producing a plasma which emits continuum radiation

been carried out in this respect by Kuhne [1982] and it has been shown that shot to shot reproducibility can be better than ~ 5 % for part of the normal incidence spectral region (40 to 80 nm) This compares to a value of better than ~ 1 % for synchrotron light sources and 25 – 40 % for B-R-V based sources [Kuhne, 1982]

1 6 3   Temporal and spatial plasma properties.

The small size and potentially short duration of laser plasma continuum emission make it an exceptionally good back-lighter in experiments such as the dual laser plasma experiments (DLP) At DCU, a predominantly tungsten target is illuminated with 1064 nm radiation from a Nd   YAG laser with a duration of ~ 17 ns The resulting plasma has a continuum emission duration in the XUV comparable to the laser pulse width [Collins et al, 1993] and thus allows time resolved experiments to be carried out without the need for detector gating Because of the small size, the continuum source acts as a point source, which is generally easier to model in ray tracing software such as Shadow[t] The LPP continuum source also has increased uniformity in the angular sense when compared to the synchrotron source [Carroll et al, 1980]

---

[t] Shadow   Ray tracing software using Monte Carlo techniques for the modelling of VUV, XUV and soft x-ray optical systems Available from www xraylith wisc edu/shadow/

1.7 Dual laser plasma (DLP) technique.

The structure of the atom is such that inner shell electron binding energies generally result in energy transitions in the VUV normal incidence region and XUV part of the spectrum Therefore, in order to investigate these transitions in detail, both a way of generating continuum at these wavelengths and a means of detecting the spectral signal are needed

The laser produced plasma is ideal for the production of charged species as the relative abundance of certain ion species can be controlled to some degree by changes in the power density i e by changing the on-target focusing conditions or altering the laser pulse energy If the system set-up allows for temporal – by control of the inter laser delay – as well as spatial resolution – i e by the use of apertures, slits and / or toroidal optics – then a high degree of ion stage differentiation can be obtained

Target chamber with detail removed

Backlight target for continuum emissi

Lens arrangement with x y z movement

Optic axis of spectrometer

Absorbing target
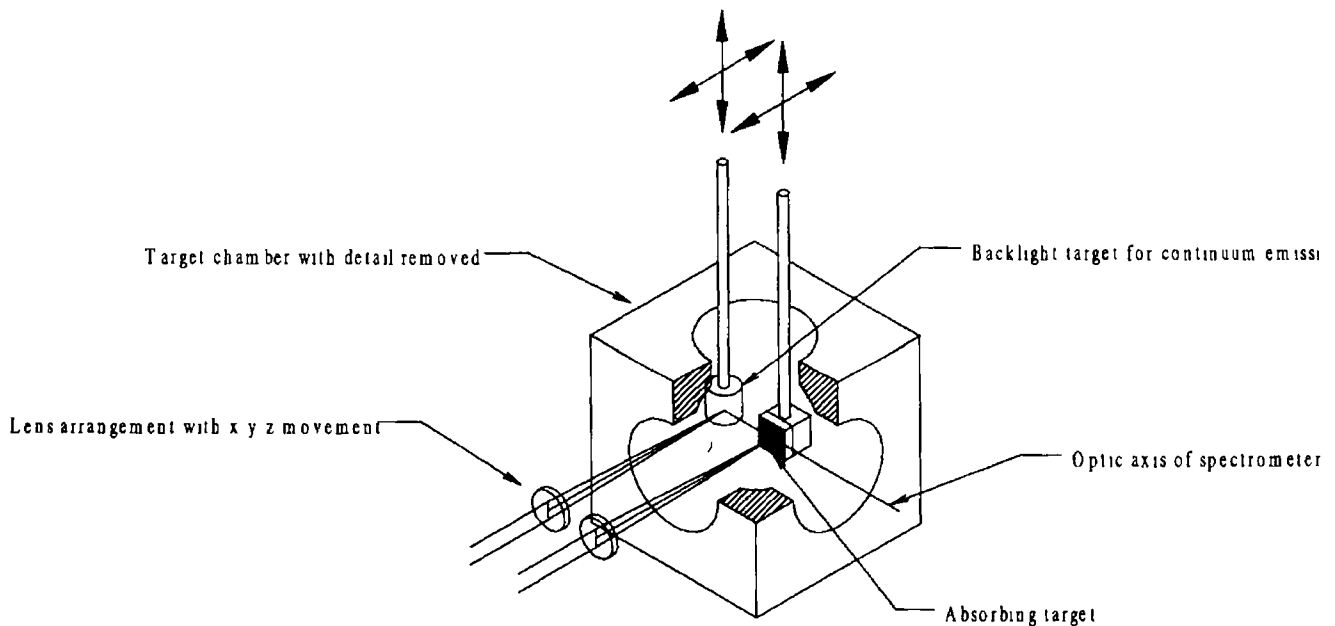
Figure 1-4   *Diagram showing general arrangement for dual laser plasma*
(DLP) experiment

19

1.7.1   History of the DLP technique.

The first attempt to develop a dual laser plasma technique for photoabsorption studies was made by Carillion *et al* [1970] who used aluminium for both the continuum emitting plasma as well as for the sample plasma Although the emission from aluminium is rich in line structure, the authors found that the underlying weak continuum emission present could be used for a continuum light source between the stronger line emissions This restricted them to time and space studies of the laser generated plasma plume within these 'line free' windows (~ 9 8 nm) The results showed that inverse bremsstrahlung was the dominant mechanism in the hot dense region of the aluminium plasma plume (i e at short inter laser time delays) and also that photoionization was evident at moderate distances (~ 0 3 mm) where the plasma was cooler and thus recombining

The application of rare-earth continua to photoabsorption studies was first performed by Carroll *et al* [1977] In these experiments, the authors studied the photoabsorption spectra of single ionized lithium Li^+ Using a beam splitter a Ruby laser was split into two beams, the first of which was focussed on a cylindrical tungsten target and the other onto a planar lithium target The experimental geometry was such that it resulted in spatially resolved spectra with a magnification of ~ 20 The $1s^2\ ^1S_0 \rightarrow 1snp\ ^1P_0$ principal series of Li^+ was recorded up to the n = 7 member The singly charged ion Li^+ is iso-electronic to helium and thus shows analogous doubly excited hollow atom states to helium but at a much higher energies due to the greater nuclear charge present In the work by Carroll *et al* [1977] the doubly excited $1s^2\ ^1S_0 \rightarrow 2snp\ ^1P_1$ series -- which was first observed 13 years previously in He by Madden and Codling [1965] with the use of a synchrotron radiation source -- was observed for the first time in a He like ion

One of the main advantages of using the DLP technique is that it allows for the study of photoabsorption in extended iso-nuclear and iso-electronic sequences

20

1.7.2 Recent XUV DLP experiments on lithium

The application of the dual laser produced plasma technique to the study of 'hollow lithium'[†] was recently performed by Kiernan *et al* [1994] On moving from helium to lithium the addition of a single electron makes possible the formation of triply excited states in which all three electrons reside in the L (or higher) shell leaving the K shell unoccupied Electron-electron effects are dominant in this Coulombic four-body system, thereby offering the possibility of studying both direct and resonant double photoionization The experimental arrangement consisted of a grazing incidence type spectrometer with a 1200 groove mm[1] grating and a CEMA / PDA detector combination resulting in a resolution of ~ 1500 before de-convolution The absorbing column was produced by focusing the output from a flashlamp pumped dye laser (2 5 J with pulse duration of 0 5 μs FWHM) onto the lithium target with a 22 mm line focus The photoabsorption spectrum in the vicinity of the $1s^2 2s$ (^2S) → $2s^2 2p$ (^2P) triply excited transition was studied, and the position, width and profile index of the main resonance were measured

---

[†] A hollow atom or ion is one in which at least one inner-shell is empty
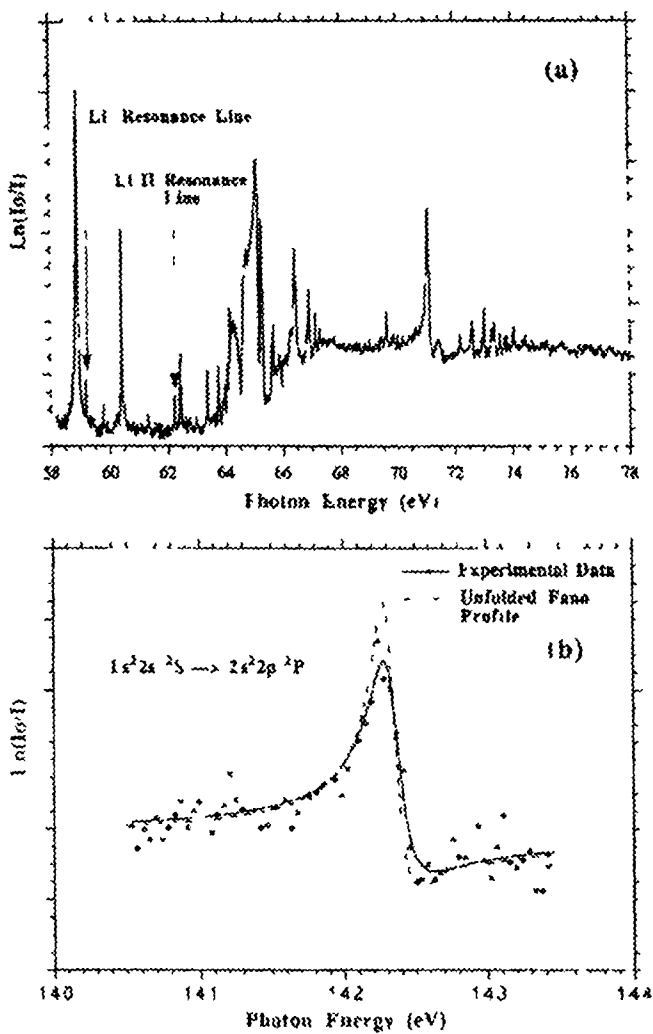
Figure 1-5 (a) K-shell absorption spectrum of the dye laser produced lithium plasma at a inter plasma delay of 750 ns corresponding to maximum ground state neutral lithium. Indicated on the plot are the strongest lines of valence excited Li and ground state Li^+ in this energy region The weakness of both lines is a good measure of the purity of the ground state neutral lithium in the absorbing sample (b) Photoabsorption spectrum of atomic lithium in the energy window of the main $1s^22s$ (^2S) $\rightarrow 2s^22p$ (^2P) transition The broken line represents a Fano profile fit to the restored data following removal of instrument broadening [Kennedy et al, 1996]

1.7 3 Normal incidence VUV DLP experiments

In work carried out by Jannitti et al [1985], the photoabsorption spectrum of beryllium was measured m both the normal incidence and grazing incidence regions by use of the dual laser plasma technique To produce the two plasmas a 10 J, 15 ns (FWHM) laser was split into two parts with a variable path difference between the two beams thus allowing a variable delay between the two plasmas The continuum

target used was copper A spherical cylindrical lens focuses the laser onto the beryllium target producing a line focus with dimensions of ~ 100 μm wide and up to 10 mm in length In this way, the spreading velocities of the streaming plasma along the line of sight were minimized, and the absorbing length is maximized

The experiments utilised a 2 meter normal incidence spectrometer system with a 1200 line mm^{-1} spherical grating The dispersed VUV radiation was incident on a scintillator coated face plate and imaged by two high speed objectives (N A = 0 75) external to the vacuum system on an intensified photo diode array (~ 0 0195 nm pixel^{-1}) The absorption spectrum close to the ionization limit of Be$^+$ was studied The photoionization cross sections of the outer electron for transitions of the type 2s → εp and 2p → εd were measured at threshold The values thus obtained were σ = (1 5 ± 0 1) * 10^{18} cm^2 and σ = (2 5 ± 0 5) * 10^{18} cm^2, respectively

Figure 1-6   Solid curve, experimental absorption coefficient of the resonance series $1s^2 2s\ ^2S \rightarrow 1s^2 np\ ^2P^0$ with n = 5 to 8 of Be^+ at a distance 0 6 mm. From the target surface and ~ 70 ns laser delay Dashed curve, convolution of the computed coefficient with the instrument function In the inset, the best fit of the instrumental function (solid curve) with a Voigt profile (dashed curve) is shown [Jannitti et al, 1985]
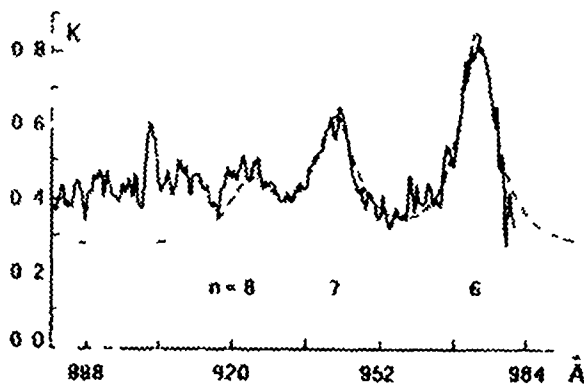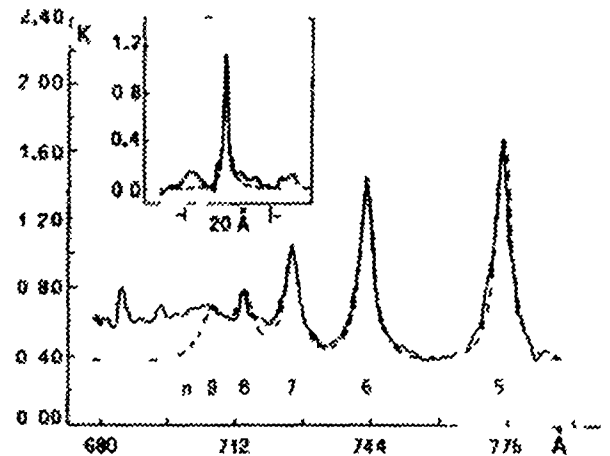
Figure 1-7 Solid curve experimental absorption coefficient of the series $1s^2 2p\ ^2P^0 \rightarrow 1s^2 nd\ ^2D$ with n = 6 to 8 of Be^+ versus wavelength at 0 6 mm distance from target Dashed curve, convolution of the computed coefficient with the instrument with the instrument function [Jannitti et al, 1985]

In some further experiments also done by Jannitti *et al* [1986], the photoabsorption spectrum of B^+ was studied in the range 40 to 170 nm. The experimental set-up used was similar to one used in the Be^+ experiments of Jannitti [1985]. The length of the absorbing plasma was increased using a cylindrical lens, up to about 18 mm. The contribution of the absorption from B III was minimized by controlling both the power density on the boron target and the delay between laser pulses. The photoabsorption spectrum of B^+ was found to be optimized at a position of 1 to 1.5 mm from the surface of the boron target with a 80 ns inter laser delay. The values for the photoionization cross-section at threshold thus obtained were (1.7 ± 0.6) $* 10^{-18}$ cm^2 for the series $2s^2 \, ^1S \rightarrow 2snp \, ^1P^0$, and (4.0 ± 0.5) $* 10^{-18}$ cm^2 for the series $2s2p \, ^3P^0 \rightarrow 2snd \, ^3D$.
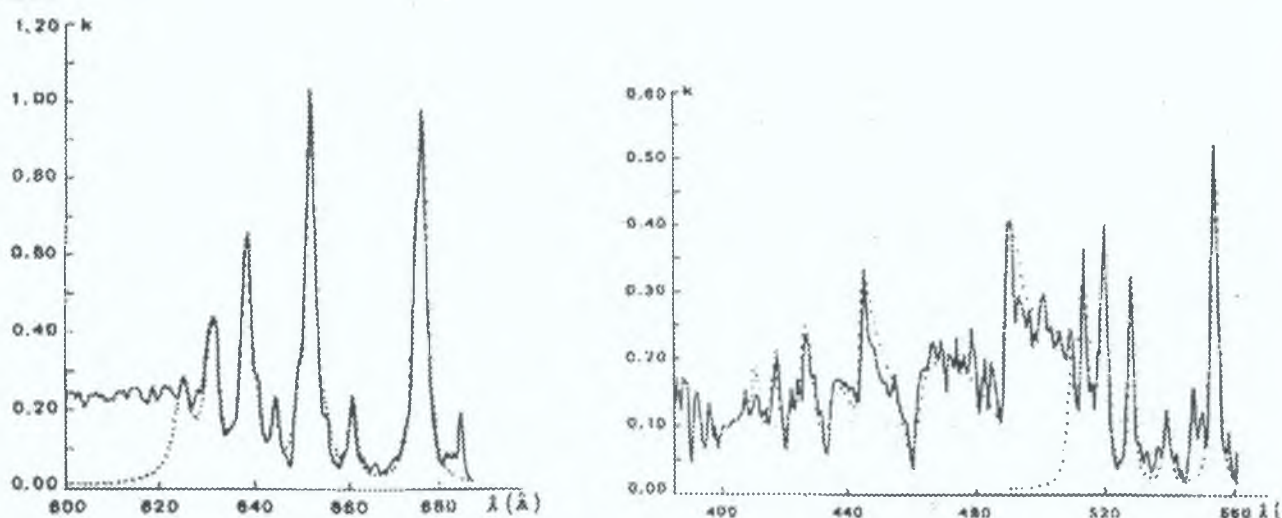
Figure 1-8.   The absorption coefficient k for (a) the series $2s2p \, ^3P^0 \rightarrow$ 2snd, ns ^3D, ^3S and (b) the series $2s^2 \, ^1S \rightarrow 2snp \, ^1P^0$ and for $2s^2 \, ^1S \rightarrow 2pnd$, ns $^1P^0$. Solid line: experiment. Dotted line: best fit [Jannitti et al, 1986].

1.8   Concluding remarks.

In this chapter the fundamental physics of laser produced plasmas has been discussed in terms of the interaction of the laser radiation with the target material and the resulting plasma formation and primary emission processes within such plasmas. A number of applications of laser plasma broadband VUV continuum sources have been discussed. The properties of such sources include; ease of production, good

reproducibility, 'line-free' structure, high peak brightness, large spectral range, short duration, ease of source alignment and small extent A sample of recent photoabsorption experiments in the XUV and normal incidence VUV region which utilize such sources for the backlight were briefly described

Chapter 2.   Experiment set-up.

This chapter outlines the experimental system configurations used in the spectroscopic investigations reported in chapter 3. A brief outline of the theory of the Rowland circle mount is considered and the important parameters describing the spectrometer performance such as linear dispersion and resolution are summarised. Associated instrumentation such as a Channel Electron Multiplier Array (CEMA), Photo Diode Array (PDA) and back thinned charge coupled devices (CCD) are described in terms of mode of operation and characteristics.

2.1   Overview of experimental arrangement.

The core experimental system is based on a near normal incidence spectrometer which has a focal length close to one metre. Throughout the studies two image detection systems were used. These consisted of a Galileo™ Channel Electron Multiplier Array with an EG&G™ Photo Diode Array readout and an Andor Technology™ back thinned CCD. The longest possible wavelength the instrument can reach mechanically when equipped with a grating with 1200 grooves mm^{-1} is 325 nm at the centre of the detector plane. However as the grating is blazed at 80 nm the efficiency is observed be poor above ~ 120 nm.

A laser plasma light source was coupled to the spectrometer system by a vacuum-optical beam-line. A glass capillary array (GCA) was positioned between the plasma target chamber and the spectrometer's slit. This reduces the amount of plasma debris that can enter the spectrometer and also allows for differential pumping across the GCA needed for experiments on gaseous absorption while still holding a vacuum of < 10^{-6} mBar in the spectrometer chamber.

Nearly all VUV and XUV spectrometers employ a configuration developed by H.A. Rowland at the end of the last century. Whereas the detection of short wavelengths has had major advancements in recent years by development of channel electron multiplier arrays[†] (CEMA) [Oschepkov *et al*, 1960, Goodrich and Wiley,

---

[†] Original conceived by Farnsworth in 1930, the continuous dynode electron multiplier was implemented concurrently by groups in the USSR, USA and UK in the 1960's.

1962, Adams and Manley, 1965, 1966] and back thinned CCD arrays [Janesick *et al*, 1985], the Rowland circle mount has not been changed in any significant fashion since it's early development The other significant developments in the field of XUV and VUV spectrometer design have been the use of toroidal optics [Tondello *et al*, 1975] which allow better spatial imaging of the source, holographic gratings which have resulted in more uniform groove spacing and the possibility of aberration corrected gratings and vari-spaced gratings which produce focal planes devoid of curvature and hence suitable for readout by flat detectors (e g CCDs)

2.2 Rowland circle normal incidence spectrometer mount

Diffraction gratings have their origins in the early 1800's where they were first used to disperse light by T Young and later by J von Fraunhofer Since then, several attempts were made to produce quality gratings for scientific studies It wasn't until the late 19th century, when H A Rowland began producing gratings with sophisticated ruling engines, that the ruled diffraction grating made an impact on the field of spectroscopy [Jobin Yvon™, 1988] It is now over 100 years since H A Rowland discovered the possibility of using a concave grating placed tangentially on a circle in order to diffract and focus light which had it's source on this circle The diffracted spectrum is focused onto this circle which is referred to as the Rowland circle

The associated theory may be developed using Fermat's Least Time Theorem There are many variations on the Rowland circle mount (i e Eagle, Grasshopper etc) and each of these have relative advantages and disadvantages depending on the application The parameters which govern the choice of mount are principally the spectral range to be covered, the resolution required, degree of astigmatism that can be tolerated as well as limitations placed on the movement of the entrance and exit arms of the spectrograph [Samson, 1967 and Namioka 1959, 1961]

2.2.1 Spherical grating equation.

Spherical grating spectrometers combine the dispersive characteristics of a grating with the focusing characteristics of a spherical surface. When limits on the movement of the entrance and / or exit arm of these spectrometers are placed, various geometries and mount are defined.

The basis of the following discussion lies in the analysis of the path length difference between two different beams reflected from two different points on a curved reflecting surface. These are assumed to originate from a point source, which is situated on the Rowland circle. If this path difference equals an integral number of wavelengths then constructive interference occurs at this point. No rigorous treatment of the optical path function is given. A more detailed discussion can be found in the work done by Namioki [1959].

If we simplify the calculations by assuming that the source and diffracted spectrum lie in the x-y plane – as in the case of the Acton™ VM 521 spectrometer (see figure 2-1), then the optical path function can be written as,

$$F = |AP| + |BP| + \frac{kw\lambda}{d} = |IA| + |IB| + \frac{kw\lambda}{d} + \Delta \qquad [\text{ E 2-1 }]$$

where k is an integer and by definition is the spectral order of the diffracted image at wavelength λ, w is the inter groove distance of the grating, d is the distance between I and P on the grating surface and Δ is the aberration optical path function and contains coefficients which describe the defocusing, astigmatism, first and second type of coma, and others which describe the spherical aberration. Δ can also be thought of as a perturbation on the simple optical path lying in the x-y plane and can be expressed in terms of Y and Z coefficients as follows,

$$\Delta = FY + D\frac{Y^2}{2R} + A\frac{Z^2}{2R} + C_1\frac{Y^3}{2R^2} + C_2\frac{YZ^2}{2R^2} + S_1Y^4 + S_2Y^2Z^2 + S_3Z^4 + ... \qquad [\text{ E 2-2 }]$$

where R is the radius of curvature of the grating, D is a coefficient which characterises defocusing, A characterises astigmatism, C_1 characterises the 1st type

coma or classical coma, C_2 characterises the 2nd type coma and S_1, S_2 and S_3 characterise spherical aberration.
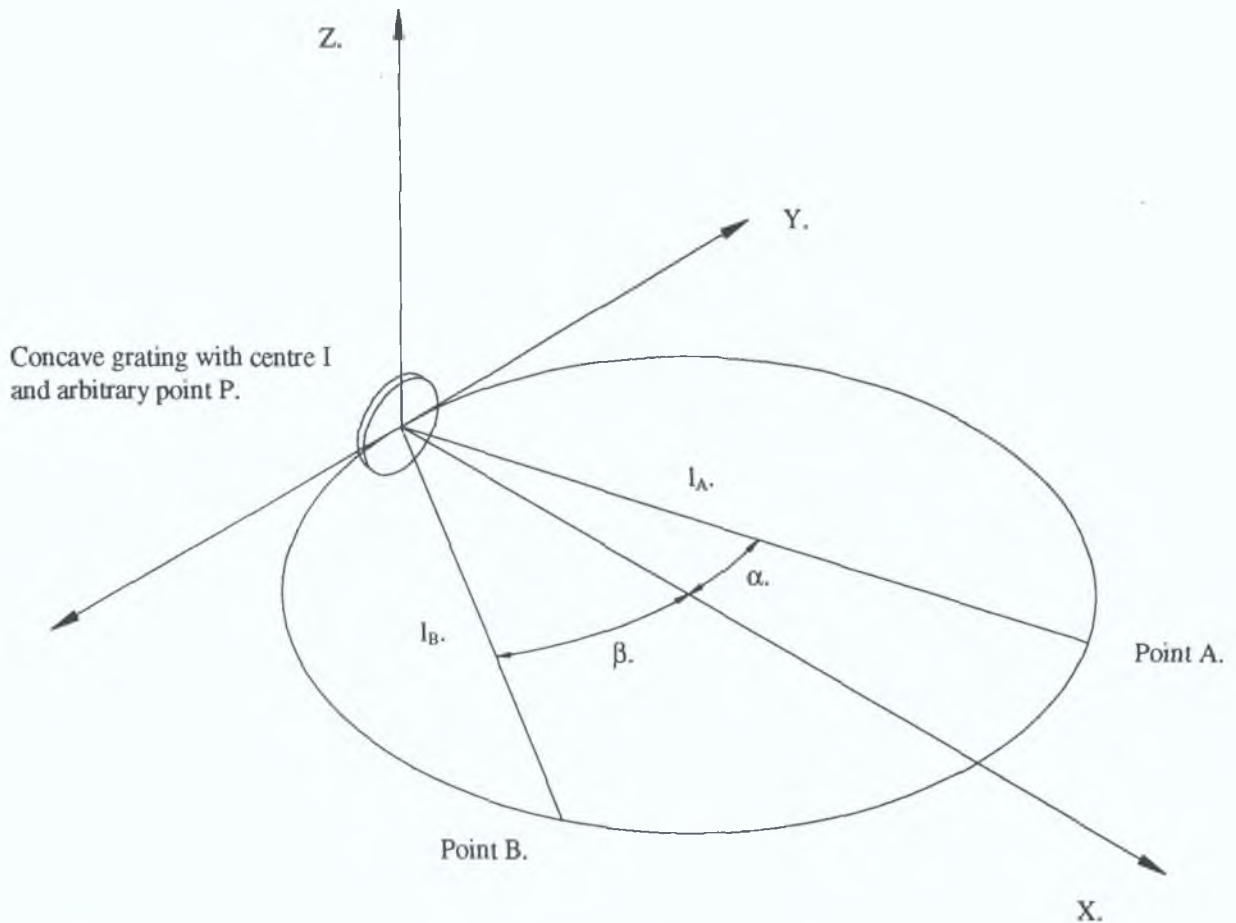
Figure 2-1.   Diagram showing parameters used in the description of the concave grating. Point A represents the position of the entrance slit while point B represents the position of the exit slit or detector plane.

In order to obtain the location of the spectrum, the terms F and D are equated to zero. This will give the locus of the spectrum. The residual values for A, C_1, C_2, S_1, will give the remaining aberrations present in the image spectrum. These aberrations degrade spectral resolution, spatial resolution and / or signal-to-noise ratio. The most significant are astigmatism, coma, spherical aberrations and defocusing. The optical path function F represents the permissible path lengths. Coma is the result of the off-axis geometry and is seen as a skewing of rays in the dispersion plane enlarging the base on one side of the spectral line. Spherical aberrations are the result of rays emanating away from the centre of an optical surface failing to find the focal point as

29

those from the centre. Astigmatism is characteristic of an off-axis geometry. It tends to have the effect of representing a point source as a line on the focal plane.

Expressing this aberration optical path function in terms of polar co-ordinates one can obtain [Jobin Yvon™, 1988],

$$\Delta = Y\left[\sin(\alpha) + \sin(\beta) - kn\lambda\right]$$
$$+ \frac{Y^2}{2}\left[\frac{\cos^2(\alpha)}{l_A} - \frac{\cos(\alpha)}{R} + \frac{\cos(\beta)}{l_B} - \frac{\cos(\beta)}{R}\right]$$
$$+ \frac{Z^2}{2}\left[\frac{1}{l_A} - \frac{\cos(\alpha)}{R} + \frac{1}{l_B} - \frac{\cos(\beta)}{R}\right]$$
$$+ \frac{Y^3}{2}\left[\frac{\sin(\alpha)}{l_A}\left(\frac{\cos^2(\alpha)}{l_A} - \frac{\cos(\alpha)}{R}\right) + \frac{\sin(\beta)}{l_B}\left(\frac{\cos^2(\beta)}{l_B} - \frac{\cos(\beta)}{R}\right)\right]$$
$$+ \frac{YZ^2}{2}\left[\frac{\sin(\alpha)}{l_A}\left(\frac{1}{l_A} - \frac{\cos(\alpha)}{R}\right) + \frac{\sin(\beta)}{l_B}\left(\frac{1}{l_B} - \frac{\cos(\beta)}{R}\right)\right]$$
$$+ Y^4[...] + ... \qquad\qquad [\text{E 2-3}]$$

where l_A, α and l_B, β are the polar co-ordinates of A and B, and Y^4 and higher order terms can be considered negligible. By equating the coefficient of Y (i.e F) term to zero in equation 2-3 one obtains the fundamental grating equation,

$$\sin(\alpha) + \sin(\beta) = \frac{m\lambda}{d} \qquad\qquad [\text{E 2-4}]$$

where m is the spectral order and d is the inter groove distance.

2.2.1.1 Dispersion.

The angular dispersion, $d\beta/d\lambda$, defines the angular separation between two wavelengths for a particular spectral order m, inter groove spacing d and diffracted angle β and can be expressed as.

$$\frac{d\beta}{d\lambda} = \frac{m}{d\cos(\beta)} \qquad\qquad [\text{E 2-5}]$$

Linear dispersion, $d\lambda/dx$, defines the extent to which a spectral interval is spread out across the focal plane of a spectrometer and therefore is associated with

30

an instrument's ability to resolve fine spectral detail. Linear dispersion perpendicular to the diffracted plane at a central wavelength λ can be expressed as,

$$\frac{d\lambda}{dx} = \frac{d\lambda}{d\beta} \cdot \frac{d\beta}{dx} \qquad \text{[E 2-6]}$$

$$\frac{d\lambda}{dx} = \frac{d\cos(\beta)}{mR} \qquad \text{[E 2-7]}$$

where d is the inter groove spacing, m is the spectral order and R is the effective focal length of the concave grating. In the case of a McPherson™ normal incidence type mount, the angle of incidence does not remain constant throughout the wavelength range. In this case it is the deviation angle (i.e. the angle subtended by the entrance slit and centre of the detector plane, $D_v = \alpha - \beta$) which remains constant at 15 ° and therefore equation 2-10 must be modified to account for this. If one substitutes $\alpha = 7.5 ° + \varphi$ and $\beta = 7.5 ° + \varphi$ into the general grating equation where φ is the grating's angle of rotation, the linear dispersion perpendicular to the diffracted plane can be expressed as,

$$\frac{d\lambda}{dx} = \frac{d\cos(7.5)\cos(\varphi)}{mR} \qquad \text{[E 2-8]}$$

By equating the D term in equation 2-2 to zero one obtains the condition for focusing on the tangential focal plane, with the possible values for α and β given by the following.

$$\frac{\cos^2(\alpha)}{l_A} - \frac{\cos(\alpha)}{R} + \frac{\cos^2(\beta)}{l_B} - \frac{\cos(\beta)}{R} = 0 \qquad \text{[E 2-9]}$$

Considering the last equation and it's solutions, it can be shown those if point A is on the Rowland circle then point B will also be on the Rowland circle. If the polar co-ordinates of point A and B are substituted in the terms for the aberrations then it is observed that only the C_1 term in equation 2-2 vanishes. Therefore, on a Rowland circle there is no 1st type coma; only astigmatism, 2nd type coma and spherical aberration.

2.2.1.2 Wavelength and order considerations.

Because of the inherent structure of a grating there will exist multiple orders with relative intensities determined by the coating used and the blaze angle as well as the groove shape. The presence of these multiple orders degrades the performance of the spectrometer and it is sometimes necessary to incorporate filters to limit the bandpass of the system. For the same angle α and at the same angle of observation β several wavelengths are superimposed. These are all wavelengths for which $m\lambda/d$ = constant or equally $m\lambda$ = constant.

2.2.1.3 Resolving power.

Resolving power $\Re$ is a theoretical concept and is given by,

$$\Re = \lambda/\delta\lambda \qquad [\text{ E 2-10 }]$$

where $\delta\lambda$ is the wavelength separation of two peaks which are just resolved and λ is the wavelength of the spectral region of interest. Applying this concept to the use of gratings, it can be shown that [Samson, 1967],

$$\Re = knW_g \qquad [\text{ E 2-11 }]$$

where in this case W_g is the width of the grating illuminated with the incident radiation, k is the spectral order that the instrument is being used in and n is the groove density of the grating being used. Using equation [E 2-11] to define the geometry of a system with the separation of α and β fixed it can be shown [Samson, 1967] that the theoretical resolution can be expressed as,

$$\Re = \frac{W_g (\sin\alpha + \sin\beta)}{\lambda} \qquad [\text{ E 2-12 }]$$

The theoretical resolving power of an instrument is defined principally by the width of the grating illuminated, the central wavelength to be resolved and geometry of the system used. According to the modified Rayleigh's criteria, two spectral peaks are considered resolved if the ratio of minimum intensity (at the position between the peaks) to that of the maximum intensity of either peaks is less than $8/\pi^2$

[Namioka, 1959] Although the theoretical resolving power of the spectrometer predicted by equation 2-12 is approximately 30000, the experimentally measured resolving power as measured by Acton™ is approximately 5700 @ 80 nm when using 10 μm entrance and exit slit widths and represents the maximum resolution achievable. The difference in theoretical and experimental values is primarily due to optical aberrations present and the use of entrance and exit slits of finite width

2.2.1 4 Grating efficiency

The concentration of a limited region of the spectrum into any order other than the zero order is performed by using grooves which have a defined angle to the incident light. Blazed gratings are manufactured to produce maximum efficiency at designated wavelengths by appropriate selection of groove geometry. Blazed grating groove profiles are calculated for the Littrow condition where the incident and diffracted rays are in auto-collimation (i e $\alpha = \beta$) At the blaze wavelength, λ_{blaze} α = $\beta = \omega$ = blaze angle and,

$$2\sin(\omega) = mn\lambda_{blaze} \qquad\qquad [\text{ E } 2\text{-}13]$$

where n is the groove density

In the case of the Bausch & Lomb 1200 groove mm ^{1} grating which is blazed at 80 nm in first order the required angle is 2 75 ° The principle is to rule the grating so that the reflecting elements are tilted with respect to the grating surface The grating efficiency curve shifts so that the maximum efficiency is not at the zero order Efficiency in higher spectral orders usually follows the first order efficiency curve For a grating blazed in first order the maximum efficiency for each of the subsequent higher orders decreases as the order k increases The efficiency also decreases the further off-Littrow the grating is used

2.2 2 Acton spectrometer mount

The spectrometer used throughout these investigation was an 1 m focal length Acton™ model VM 521 using a 1200 lines mm ^{1} spherical concave holographic

grating with an iridium coating The optical mount system used is based on a
Rowland Circle mount in the general McPherson™ normal incidence configuration
[Tang *et al*, 1991] This mount is ideal for normal incidence work as both the
entrance slit and exit slit or, in this case, the focal plane are fixed in space

The principle of the McPherson™ mount is that the grating is constrained to
move along the bisector of the angle subtended by the entrance slit and centre of exit
plane from the centre of the grating while simultaneously the grating is rotated about
a vertical axis tangent to it's centre This movement is achieved by using a cam
driven stage which is machined to give the correct combination of movements for
each wavelength Fine focus adjustments to the movement can be made through the
use of two micrometers external to the vacuum system

It can be shown that the diffracted spectrum will only be focused for one
value of φ, where φ is the grating rotation If the grating is rotated the diffracted
spectrum will no longer be focused on the Rowland circle and therefore a linear
motion is needed This linear motion can be approximated by considering figure 2-2

$$x + GM_0 = R \qquad\qquad \cos(\varphi) \cong \frac{GM_0}{R}$$

Therefore,

$$x \cong R\{1 - \cos(\varphi)\} \qquad [\text{ E 2-14 }]$$

Concave grating
original position G₀ → original position G_0

Translational
movement x

G

Rotational
movement φ

Incident angle

Diffracted
angle

Deviation
angle

Exit slit
Bo
B

Mo
O

A

Entrance slit
Ao
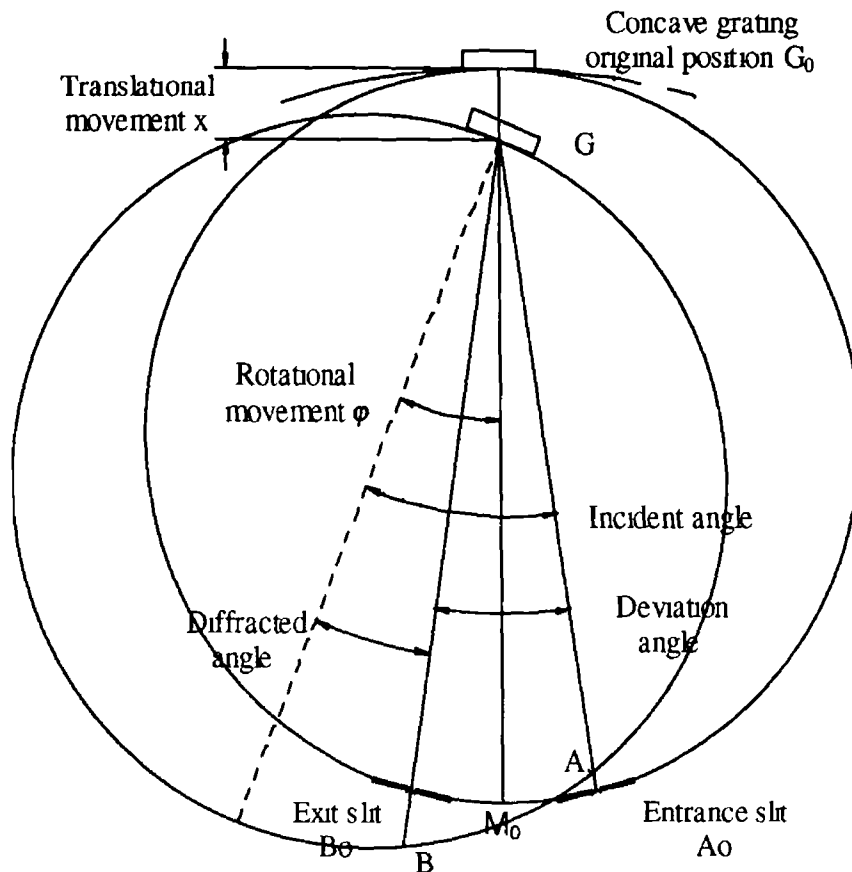
Figure 2-2   Schematic showing rotational (φ) and translational (x) movement of the grating in the McPherson mount when grating is scanned from λ to $\lambda+\Delta\lambda$

With this off-Rowland circle type mount, the translation of the grating causes the shift of the optical axis from the centre of the grating to the slits The displacement of the optical axis is sufficiently small to be considered negligible

Although the limits of the grating movement allow for a possible wavelength range between 30 and 325 nm, m practice it has been observed that measurements are confined to the region where the CEMA detector and grating are both efficient The grating efficiency profile falls off gradually in the long wavelength region while the CEMA detection efficiency falls off rapidly at wavelengths greater then ~ 180 nm The use of a back-thinned CCD detector does not extend this range as the efficiency of this detector also falls off similarly In absorption studies, the effect of order over lapping at wavelengths greater than ~ 75 nm means that studies are confined to the wavelength range where second order continuum emission does not saturate the measurement

The only modifications made to the commercial VM 521 spectrometer for this project were the replacement of the existing flanges to facilitate a penning gauge to be positioned closer to the main chamber of the spectrometer and also to house an inspection window which allows viewing of alignment HeNe laser on the grating.

2.2.2.1 Aperture ratio and acceptance angle.

The aperture ratio and acceptance angle, are principally defined by the external coupling system used. Without any spatial slits or apertures and with no GCA separating the source from the spectrometer, the instrument operates as a f/10 instrument. The acceptance angle in the horizontal plane (dispersed plane) is 5.7° while the acceptance angle in the vertical plane is 3.2 °. In the case of experiments carried out in this thesis, a glass capillary array (GCA) was used to prevent plasma debris contaminating the spectrometer chamber and also to allow for a pressure differential between the target and spectrometer chambers. The GCA used had specifications which are outlined in the appendix VIII, the most important of which is the thickness of the plate (3 mm) and the pore diameter (50 μm) as well as exposed diameter (6 mm). With the limited exposed diameter, it can be shown that only single reflections within the capillaries are possible. The distance between the entrance slit and the GCA plays an important part in determining the acceptance angle of the combined system. The GCA was located approximately 212 mm from the entrance slit in experiments with direct coupling of the target chamber to the spectrometer, the acceptance angle was 17 mrads (assuming an extended source geometry). This implies that the maximum illuminated width of the grating will be 34 mm, and the theoretical maximum resolution achievable will be down proportionally. However, in reality grating aberrations will diminish the actual resolution achievable well below the grating width limit.

2.2.2.2 Bausch & Lomb™ concave grating.

The holographic concave grating used in the Acton™ VM 521 is one provided by Bausch & Lomb™. It has 1200 lines mm^{-1} and a blaze angle of 2.75 °, which results in a first order blazed wavelength of 80 nm. The grating has

dimensions of 56 mm in height (in groove direction) and 96 mm in width and is located by a kinematic mount which facilitates inter change of gratings without re-alignment The coating used is iridium, which yields a good reflectivity throughout the wavelength range used Iridium is ideal for efficient reflection coatings at short wavelengths as it has one of the highest electron densities of all the metals [Samson, 1967]

2 2 2 3 Entrance and exit slit assemblies.

The exit slit assembly was removed and replaced by an adapter flange to hold the CEMA intensifier to allow for the multi-channel detection of the spectrum [Doyle, 1995] The entrance slit has a vertical baffle, set at 3 mm The entrance slit width used was generally 50 µm (dial setting), although investigations with other slit widths were performed in order to find the optimum slit width for each of the detectors used The slit is adjustable from 5 to 3000 µm with a quoted accuracy of 10 µm [Acton™] The slit assembly has stops which prevent the slit jaws from touching and therefore it is not possible to completely close the slit

2 2 2 4 Spectra drive controller

The wavelength range was scanned using a precision lead screw external to the vacuum system This was connected to a stepper motor and in turn connects to a drive controller provided by Acton™ This permits computer as well as manual wavelength selection In the initial commissioning of the instrument the bellows assembly was found to be leaking and was therefore changed This assembly was replaced with one which was slightly too long and therefore the dial reading on the spectral drive controller no longer represents the actual wavelength at the centre of the focal plane Because the equation governing the translational motion of the grating (equation 2-6) is not linear, the offset is not exactly constant throughout the wavelength range This was confirmed using carbon and aluminium spectra lines and identifying features so that a reference spectrum was obtained for the 30 nm to 220 nm spectral range

2.2 2.5 Aberrations.

Since the spectrometer is a near normal incidence type with a 15 ° deviation angle there is very little astigmatism present in the final image Most of the important work for this thesis was done using an Andor™ back-thinned CCD array detector used in full vertical binning mode over a 15 mm height This procedure yielded no appreciable degradation in resolution when compared to a spectra recorded by a single horizontal row of pixels thus indicating the very low astigmatism and good angular alignment of the detector with the spectral image

2 2 2 6 Stray and scattered light

Stray and scattered light are kept to a minimum by use of a number of baffles m the entrance and exit arms of the spectrometer Also the use of a GCA limits the extent of the grating illuminated thus reducing the possibility of light reflecting off the grating mount itself Stray light also results from non perfect planeity of the reflecting surfaces A holographic grating , which is produced by use of the interference of monochromatic radiation does not have significant periodic imperfections in the groove profile or spacing and so generally does not suffer from ghosts as much as ruled gratings [Lerner and Therenon, 1988]

2 2 2 7 Order overlapping and efficiency curves

The efficiency curve of a grating shows a characteristic sharp drop off in the low wavelength limit with a lesser fall off in the high wavelength limit centred approximately around the blaze wavelength in first order (80 nm in this case) The groove shape determines the amount of radiation concentrated into a given spectral order As a result of the optical interference inherent in the operation of a grating there exists order overlaping in which light at λ/m appears at the λ location, where m is the spectral order Depending on the experimental study, this may be an important consideration and may require the use of filters to reduce the radiation from this higher wavelength

2.2 2.8 Resolution.

The groove separation determines the angular separation of the diffracted beams from two different wavelengths The theoretical maximum achievable resolution is directly proportional to the width of the grating illuminated This maximum resolution is never physically attainable due to effects such as detector resolution and entrance slit widths used as well as aberrations present in the optics of the system The choice of entrance slit width should be chosen so that the bandpass of the instrument is minimized and the throughput is maximized

2.2.2 9 Wavelength and pixel position relationship

With the removal of the exit slit assembly and it's replacement with a multi-channel detector such as the back thinned CCD or CEMA / PDA variety, a range of wavelengths may be viewed simultaneously in a single image collected from the detection electronics Depending on the geometry involved in the spectrometer design the diffraction may or may not be linear across the field of view Under these circumstances it is common to take reference spectra of such an element that has well documented line structure (e g Kelly, 1987) in this region each time the spectral range is changed Although the rotational movement of the grating is a linear function with respect to required wavelength, this is not true for the translational movement and therefore the offset between dial reading and actual centre wavelength can be expected to be not entirely constant With the use of a planar detector the linear dispersion will not be constant across the observed range and for an accurate calibration the points should be fitted with a quadratic expression of $\lambda(p)$ where λ is the wavelength and p is pixel number for each change of spectral region

2.3   Galileo™ Glass Capillary Array (GCA).

Use of glass capillary arrays GCA in VUV and x-ray applications have increased greatly in the last twenty years They are efficient in transmitting VUV radiation and show focusing properties even at low wavelengths e g XUV and soft x-rays [Chapman *et al*, 1991] They are also used in applications of gas flow collimation, in-line filtration or as calibrated leak sources [Tebo, 1994], [Wilkins *et*

39

al, 1989] GCAs are sometimes referred to as passive MCPs This term comes from the fact that the bulk of the early development work was concentrated on MCP with production techniques spilling over to GCAs

The manufacturing process starts in much the same way as MCPs Single channels are drawn as solid-glass fibres having two components, a core glass, soluble in a chemical etchant, and a lead glass cladding which is not soluble in the core glass etchant The fibre is then drawn out by processes much like that used in the production of optical fibres and multiple fibres are stacked together in a hexagonal structure The array of fibres is again drawn out and stacked and the process repeated The blocks are sliced into wafers with the channels running normal to the surface The wafers are then ground and polished to the desired dimensions The solid core is now etched thus creating the pore like structure with differences in pore diameters of less than 6 % [Wiza, 1979], [Lucatorto *et al, 1979*] The uniformity of pore dimensions and the fact that these structures can have open areas up to 60 % permits GCAs to be used as VUV and x-ray windows They can sustain a pressure differential across their faces (the controlled leak rate typically allows for 2 to 3 orders of magnitude in pressure differential for the GCA used here) and also are able prevent contamination of spectrometers from material used in studies

A Galileo™ GCA having a pore diameter of 50 μm and a length of 3 mm was used in the experiments It was housed in a custom made flange which allowed connection to 40 KF vacuum flanges at either end The length of the housing was kept small in order to ensure that the GCA could be located close to the target chamber thereby maximizing the instrument's acceptance angle It was held in place on a Viton® o-ring by an aluminium plate with three nylon screws which were positioned so that the GCA could be angularly aligned The GCA was set off centre so that it could be rotated to provide a fresh area following a build up of any plasma debris An aluminium disk with a 6 mm bore was used to mask the unused section of the GCA The full specifications of the GCA are contained in appendix VII A schematic of the GCA housing is shown in figure 2-13

In order to align the GCA, its mount was coupled to the target chamber and an alignment HeNe laser was centred on the aperture It was found that the HeNe laser could be aligned normally to target chamber side by minimising the location of the multiple reflections which occur in the rear glass plate This was important since the GCA had only limited anglular movement The GCA was then placed in the housing and the nylon screws were gently tightened A screen was placed a number of meters away and the spectral pattern intensity and symmetry was maximised by a process of tightening and loosening the three screws

In order to estimate the transmission of the GCA for VUV radiation at 50 nm it is assumed that no interference effects occur and the diffraction can be considered separately from geometrical aperture effect of the capillary array Considering a point like source at a distance, u, from the front face of the GCA (length l, pore diameter d and effective diameter D) with uniform angular radiance By using geometric optics, the rays that are emitted from the source can be divided into four groups

1   Rays that are blocked by the non open area of the GCA
2   Rays that pass directly through without any reflections
3   Rays that are reflected an odd number of times from the capillary walls
4   Rays that are reflected an even number of times from the capillary walls

The rays that pass directly through without reflections can be considered collimated as there will be a maximum divergence angle D_{max} which will depend on the d/l ratio The intensity on a screen placed a distance v from the output face of the GCA will display a Gaussian type distribution Rays which are reflected an odd number of times will tend to result in a focused intensity distribution The extent of the focus will depend on the u/v ratio The depth of focus will be approximately $2d$ Rays which are reflected an even number of times can be considered to result in a diffusive intensity distribution with no simple intensity distribution

If these arguments are applied to the optical system being used, it can be shown that $D_{max} \cong 17 * 10^{-3}$ radians The GCA holder was manufactured with a 6 mm

unmasked diameter centred on the optic axis This enabled the use of an o-ring for sealing and GCA angle alignment as well as the possibility of rotating the GCA to provide a fresh section Therefore, the maximum angle that a ray from the source can strike the capillary walls is $18 * 10^3$ radians This results in a maximum number of reflections of 0 17 and so only single reflections need to be considered The reflectivity of SiO_2 glass at these large incidence angles ($\sim 18 * 10^3$ radians) and relatively large VUV wavelengths (~ 50 nm) can be assumed to be close to unity In reality, the laser plasma has non-point like extent and so rays that originate off-axis can still possibly pass through the GCA although they do not fulfil the above criteria

2 4 Galileo™ Channel Electron Multiplier Array (CEMA)

A single stage 12 ° bias angle channel electron multiplier array (CEMA) consisting of a Micro Channel Plate (MCP) with an VUV detection enhancement coating of MgF_2 coupled to a fibre face plate with a P20 phosphor coating was used for preliminary work The CEMA assembly was constructed by Galileo™ and was attached to the exit arm of the spectrometer with the front face of the Micro Channel Plate (MCP) lying on the focal plane of the instrument Applications for CEMA based intensifiers and detectors include scanning electron microscopes, residual gas analysers, image tubes and time-of-flight mass spectrometers where they are used to detect VUV, XUV, soft x-rays, neutrons or charged particles

2 4 1 Basic construction

The construction of a single stage CEMA intensifier is shown in Figure 2-3 The MCP has an active diameter of ~ 25 mm and is 0 5 mm thick It consists of pores which are 10 μm in diameter and have a centre to centre spacing of 12 μm resulting in an open area of ~ 55 % The pores have an electrically semi-conductive and secondary electron emissive layer A single pore acts in the same way as a photo-multiplier tube but using a continuous dynode structure of the photo multiplier tube When a photon or charged particle is incident on the entrance face of a microchannel, secondary electrons are generated Due to the bias applied, these secondary electrons are accelerated down the channel towards the output end When these electrons strike

the wall, additional secondary electrons are released This process is repeated continuously along the micro-channel and therefore the process amplifies the initial event yielding up 10^4 electrons at the output Higher gains are possible if two or more of these micro-channel plates are stacked together usually in opposing angles resulting in a so-called chevvon pair MCP stack The limit is set by ion feedback problems, which result in saturation and noise Normally the electrons are detected by use of a phosphor-covered faceplate, which converts the kinetic energy of the electrons to visible light This visible light is usually coupled by the use of a fibre faceplate to a detector such as a photo diode array (PDA)

In applications requiring the detection of VUV radiation at the long wavelength extreme some form of electron emissive enhancement coating on the input face of the MCP is needed Un-coated MCPs generally have quantum efficiencies of ~ 10 % in the VUV with an upper wavelength limit of ~ 130 nm after which the quantum efficiency rapidly decreases The MCP described here has a MgF_2 coating which extends this upper limit to ~ 180 nm
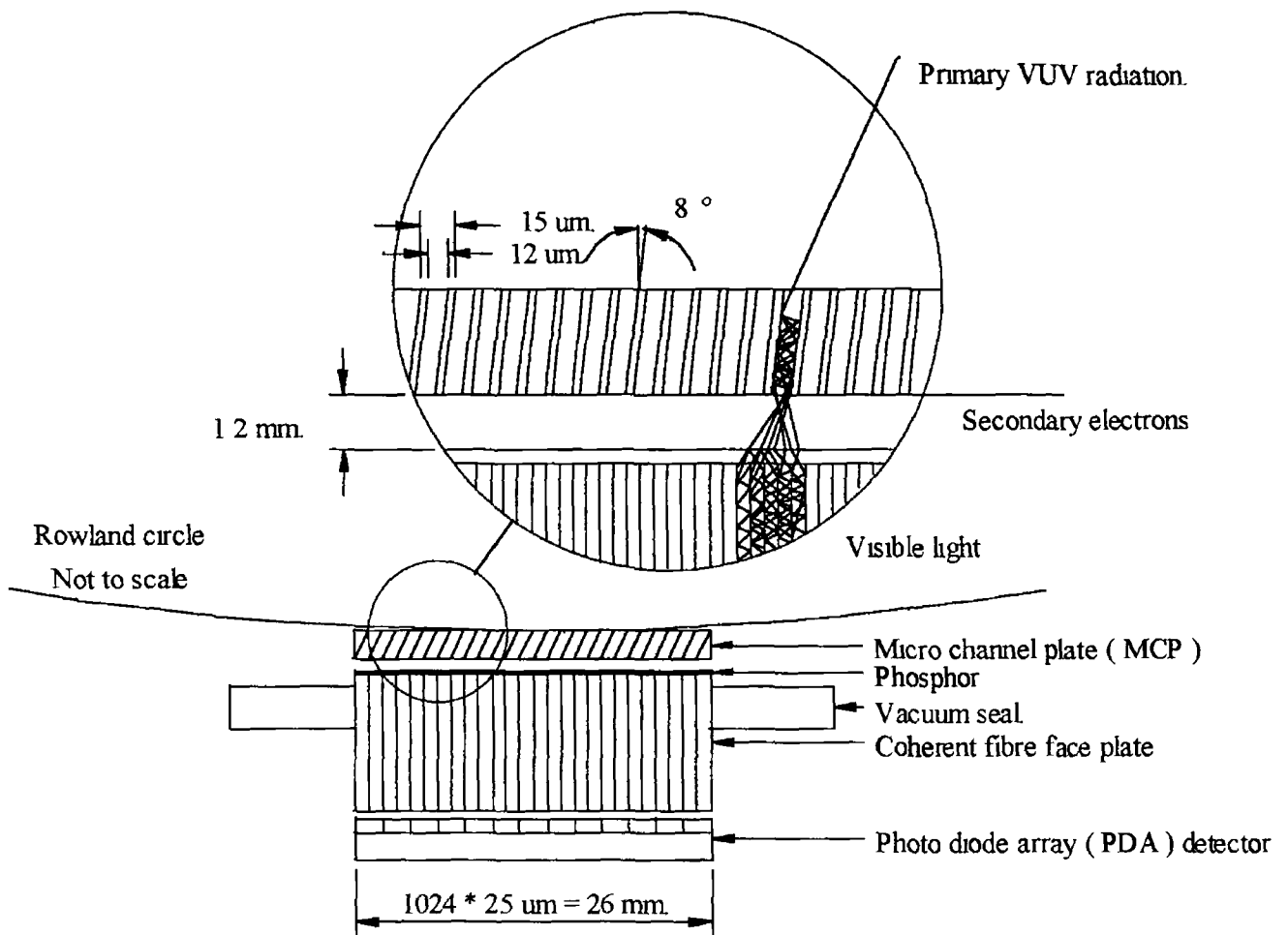
Figure 2-3   *Schematic of a channel electron multiplier array assembly*
(CEMA) showing actual micro channel plate (MCP) and fibre face plate with
phosphor coating Also shown is photodiode array PDA detector for readout

The early part of the construction of a MCP is very much like that of a glass capillary array (GCA) The main difference is the thickness of the plate is usually smaller having a thickness of < 1 mm Through further processing of the micro-channel walls, a silicon dioxide rich secondary electron emissive layer is formed on a electrically semi-conductive layer Finally, a thin metal electrode is vacuum deposited on both input and output faces to electrically connect all channels in parallel

2.4.1 Characteristics.

The gain of a single stage MCP can be expressed as,

$$G = \left\{ \frac{AV}{2\alpha V_0^{1/2}} \right\}^{\frac{4V_0\alpha^2}{V}} \qquad [\text{ E 2-15 }]$$

where V is the channel voltage, V_0 is the initial energy of an emitted secondary electron ~ 1 eV, α is the length to diameter ratio of a MCP pore and A is a proportionality constant ~ 0 4 For the Galileo™ 6025-FM MCP, $\alpha = 40$ and $V = 1000$ V which results in a gain of ~ 3 * 10^4 The gain was measured by Galileo™ to be 2 6 * 10^4 for the same conditions Efficiency for the MCP is generally about 10 to 15 % for radiation in the VUV region of the spectrum Due to the inherently high electron gam, this combination still produces a very sensitive detector The detection efficiency falls away rapidly above 200 nm
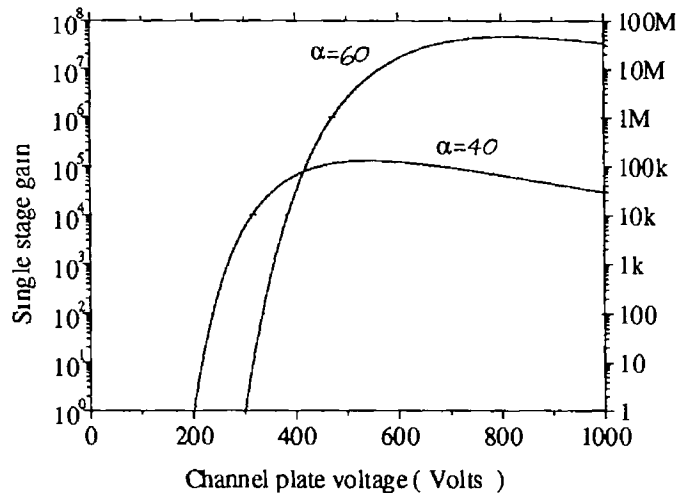
Figure 2-4   *Gain of a single stage MCP as a function of plate voltage V_0*

The limiting spatial resolution of a MCP is generally characterised by the modulation transfer function (MTF) This parameter brings together three important parameters of an imaging system. That is, resolution, contrast and sharpness of the resulting image Using the Nyquist criterion the limiting resolution of a MCP expressed in line pairs mm [1] is proportional to $\frac{1}{2}\Delta p$ where Δp is the centre to centre

spacing of the micro-channels in mm The emerging electrons are then accelerated across a gap by a positive potential and proximity focused onto a phosphor coated face plate with a visible array detector readout or direct electronic readout with the use of a single anode plate, thus providing photon / particle counting

Other factors which may limit the resolution of a CEMA are the size of electron bunch at the position of the phosphor and the size and the quality of the fibres in the faceplate used for image transfer Considering the first of these limiting factors it may be shown that the theoretical spot size d (μm) can be given by [Cromer *et al*, 1985],

$$d(\mu m) = \frac{s(\mu m)}{\sqrt{V_{Gap}}} \qquad [E 2\text{-}16]$$

where s (μm) is the inter gap spacing and V_{Gap} (V) is the inter gap potential The CEMA used in the experiments considered here had a inter gap spacing of 1 2 mm and a operational inter gap voltage of 4 kV which resulted in a theoretical spot size of ~ 19 μm There is no magnification by the fibre face plate (fibre centre-to-centre spacing ~ 10 μm) so the limit in resolution of the complete detector set-up was theoretically due to the PDA with a pixel size of 25 μm (ignoring other resolution degrading effects) which should have yielded an instrument function of 3 pixels FWHM
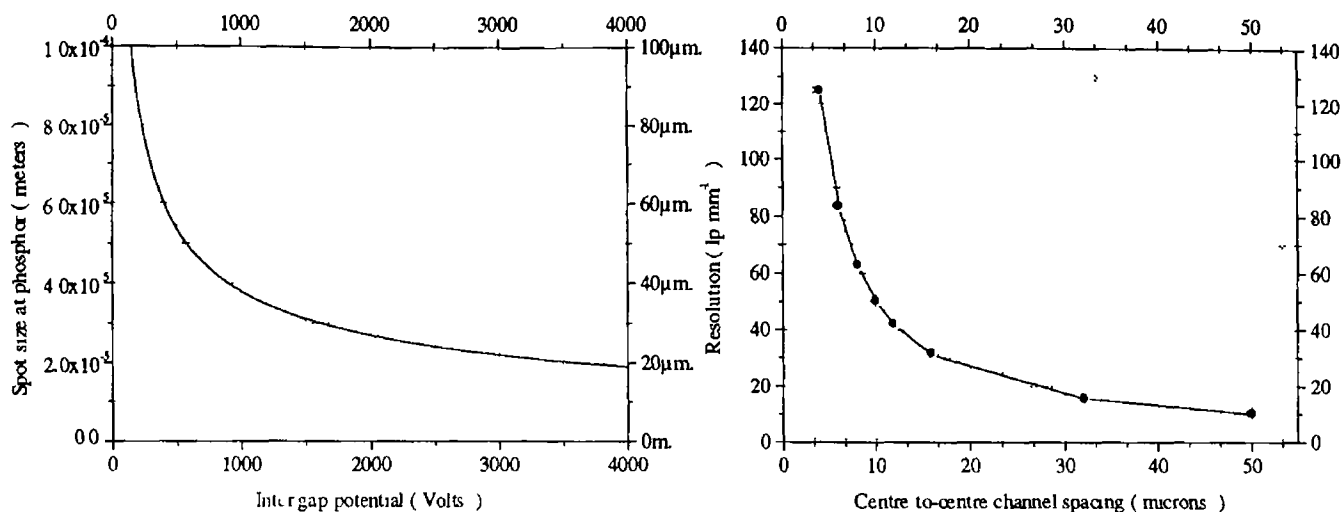
Figure 2-5   (a) Spot diameter of electron bunch at 1 2 mm inter gap distance as a function of inter gap potential and (b) resolution of MCP as a function of centre-to-centre channel spacing

In practice the instrument function was a factor of >2 worse @ 5 pixels FWHM and so the electron bunch spot was obviously significantly larger than 19 μm Problems in the detector towards the end of experiments limited the inter gap voltage to 2 5 kV which resulted in a theoretical spot size of ~ 60 μm In this case the CEMA was the limiting element in terms of resolution

If the capacitance of the MCP can be kept to a minimum, nanosecond gating is possible with such intensifiers using basic image PDA or CCD / ICCD detectors With electric fields of the order of 10 kV cm ^{1} and pore lengths of 0 5 mm the transit time for an electron pulse can be reduced to less than 500 ps without too much temporal spread of the electron bunch [Galileo™, 1995]

2.4 2   Noise contributions in CEMA intensifiers.

Although CEMA intensifiers have excellent spatial and temporal resolution properties and unrivalled efficiency in the XUV wavelength region, they are inherently noisy with significantly higher background noise than CCD based detectors [Fraser et al, 1987] Cosmic rays, thermal emission, field emission, ion feedback and internal radioactivity and material outgassing are all sources of noise in

47

CEMA based detectors In view of the very large internal surface areas of channel plates (~ 200 cm^2 for each cm^2 of intensifier area) it is reasonable to suppose that the time-dependent noise source is related to the out-gassing of the plates, whereby ions or neutrals released from the channel walls subsequently initiate avalanches Theretore exposure to atmosphere should be kept to a minimum and after each exposure, the MCP should be thoroughly out-gassed before operation in order to protect the intensifier Once the intensifier has been out-gassed, the principal source of noise is the random variations in avalanche gain due to the inherenly high gain and statisical process of electron gain Also the contribution to noise from radioactivity in the CEMA components has been shown to be significant Radioactive impurities such as potassium ^{40}K and rubidium ^{87}Rb present in the lead glass which makes up the MCP and it's casing and also in the ceramic supports are estimated to account for ~ 22 % of all background noise Cosmic ray flux is not a major background noise contribution and is estimated to account for ~ 8 % of all background noise [Fraser *et al*, 1988,1987]

2 5 Andor Technology™ back thinned CCD.

Experiments were also performed using a back thinned CCD borrowed from Queens University Belfast (QUB) The sensitivity of a CCD imager to light is determined by system noise levels and quantum efficiency Quantum efficiency measures the sensor's efficiency in the generation of electronic charge from incident photons Electron-hole pairs are produced by photons in the region from 400 to 1100 nm for front illuminated CCD This spectral window is set by the depth of penetration of the photons into the chip and the band gap energy respectively Light normally enters the CCD through the gates of the register These gates are made of very thin amorphous silicon, which is reasonably transparent at long wavelengths but becomes opaque at wavelengths shorter than 400 nm In order to extend this lower wavelength limit further so that VUV and XUV photons can be detected, the radiation must enter and pass through as little amorphous silicon gate structure as possible This is not possible with front illumination as the gate structure is necessary for electrical connections and also because ideally the image electrons should be stored away from the interface layer

It is possible to chemically etch the back face of a CCD after production so that the charge storage areas are effectively exposed to incoming radiation There is thus no extra structure that the photons need to pass through before being absorbed in the vincinity of the CCD charge storage potential wells and generating charge carriers For any given wavelength, the amount of charge stored is proportional to the intensity of the illuminating radiation This results in an ideal detector for imaging and spectroscopy studies

2 6 EG&G™ photo diode array (PDA).

The detector used to detect the visible output image from the CEMA intensifier was a linear photo diode array with 1024 pixels The detector, Model 1432, was supplied by EG&G Princeton Applied Research™ The detector interface Model 1471A optical multi-channel analyser (OMA) was also supplied by EG&G Princeton Applied Research™ The size of the PDAs pixels are 25 μm * 2 5 mm with 25 μm centre to centre spacing It has a quoted spectral sensitivity range of 200

to 1100 nm. The detector is thermally bonded to a Peltier cooler which can lower the detector temperature and therefore reduce thermally generated dark counts. With no water cooling the Peltier cooler can operate down to 5 °C. With water cooling it is possible to extend this to –19 °C. When the cooler is used for temperatures below room temperature, a dry nitrogen flow is needed in order to prevent condensation from forming inside the detector head. The analog signal is converted to a digital format using a 16 bit (with 1 bit allocated for an overflow flag) analog to digital converter (ADC) in the OMA and is available for interrogation by a computer using the GPIB interface provided [EG&G Princeton Applied Research™ literature]. See Doyle, 1995 for more details on software and interfacing.

The detector consists of an array of reverse biased photodiodes, each diode behaving like a charged capacitor. When incident light (200 to 1100 nm) enters the depletion region of the p-n junctions it has the effect of creating charge carriers – electron hole pairs – and thus decreases the effective dielectric property of the depletion layer. During each scan, the shift registers and FET switches cause the photodiodes to be successively connected to the input of the detector amplifier. Each successive junction voltage potential defines the integrated photon flux on the addressed pixel. The resulting signal, following buffering and amplification is sent to the controller interface for digitising and data processing. The output video signal is directly proportional to the incident light flux.

2.7   CCD and PDA characteristics.

2.7.1   Dynamic range of CCD and PDA detectors.

The dynamic range of a detector is the next most important parameter after the quantum efficiency. The dynamic range of a CCD imaging system is defined as the ratio of CCD saturation signal to the readout noise. A high dynamic range is more desirable especially in spectroscopic studies as it allows very weak emission lines to seen in the same frame as very strong lines and therefore the higher intensity lines do not saturate the detector.

2 7.2 Noise contributions in CCD and PDA detectors.

The sources of noise in a CCD or PDA imaging system are predominately from three areas These are photon noise, preamplifier noise, and dark current noise [Photometrics™] Photon noise, also known as shot noise, arises from the discrete nature of light production The total number of photons emitted by a steady source over any time interval varies according to a Poisson distribution The charge collected by a detector exhibits the same Poisson distribution, so that the noise is related to the square of the signal Photon noise is unavoidable and is always present in imaging systems Preamplifier noise, also called readout noise, is generated by the on-chip output amplifier This noise can be reduced to a few electrons by design Dark noise current also referred to, as thermal noise is the dominant mechanism for noise in CCD and PDA based imaging systems The electrons are generated by thermal processes and therefore cooling the detector reduces this dark current and hence the dark noise level The back thinned CCD imaging system used in the experiments carried out for this thesis had three stages of thermoelectric cooling by which it is possible to cool the detector to a temperature of -90 °C At these temperatures the detector performance rivals that of the more expensive liquid nitrogen cooled CCDs with a quoted dark current of 40 electrons pixel ^{1} sec ^{1} at a temperature of $- 20$ °C [Andor Technology™ InstaSpec IV technical manual] The PDA also had a thermoelectric cooler which allowed for the detector head to be cooled to $- 40$ °C (see page 57) resulting in a quoted dark current of 100 electrons pixel ^{1} sec ^{1} [EG&G™ 1453A operating manual]

With the exception of a few full frame images, the back thinned CCD measurements were taken using full vertical binning of the frame pixels This increases the SNR (signal to noise ratio) of the detection system but can reduce resolution of spectroscopic data if image aberrations are present or if the detector is tilted with respect to the lines

Several sources of noise are present when the signals stored by a PDA or CCD are read out They can be classified as either random noise or fixed pattern noise The fixed pattern noise in principle can be removed either by the electronics or

by later data processing Random noise arises from the electronics (primarily the input section of the pre-amp circuit) and from the statistical nature of the arrival of photons at each pixel In general, reset noise n_{reset} (also referred to as kTC noise) will dominate the signal and may be expressed as,

$$n_{reset} = \left(\frac{1}{q_e}\right)(k_B T C_{pixel})^{1/2} \qquad [\text{E 2-17}]$$

where q_e (C) is the charge on an electron, k_B (1 381*10^{23} J K^1) is Boltzmann's constant, T (K) is the absolute temperature and C_{pixel} (F) is the capacitance of a single pixel element [Howes and Morgan, 1985] The total reset noise is larger due to the multiple readout switching and therefore the C_{pixel} should be replaced by $2*(C_{pixel} + C_{video\,line})$ where $C_{video\,line}$ is the video line to clock capacitance Considering the PDA used here with $C_{pixel} = 2$ pF, $C_{video\,line} = 1\,2$ pF and $T = 288$ K, the reset noise is approximately 997 electrons and is by far the dominant noise component within the detector The noise due to the preamplifier n_{preamp} can be expressed as,

$$n_{preamp} = \left(\frac{C}{q_e}\right)(4k_B T \Delta B(k_0 / gm))^{1/2} \qquad [\text{E 2-18}]$$

where ΔB (Hz) is the bandwidth of operation, k_0/gm is the channel resistance of the input FET and C_{input} (F) is the capacitance at the preamplifier input which is composed of the series combination of $C_{video\,line}$ (F), C_{preamp} (F) and C_{stray} (F) In the case of EG&G™ PDA where $\Delta B = 10$ MHz, $T = 288$ K, $C = 10$ pF and $k_0/gm = 100$ the noise contribution from the preamplifier will be approximately 250 electrons over the entire detector array

The dark current shot noise can be expressed as,

$$n_{dark} = \sqrt{\left(\frac{I_{dark} t_f}{q_c}\right)} \qquad [\text{E 2-19}]$$

where I_{dark} (A) is the equivalent dark current and t_f (s) is the readout time Typically, the equivalent dark current will be 1 pA and so a 30 ms readout time will

result in a dark noise of approximately 433 electrons averaged over the entire array All of the above noise sources combine to give an effective total noise n_{total} which is superimposed onto the actual detected image

With the Galileo™ CEMA / EG&G™ PDA detector system the dominant type of noise present in spectral signals is fixed pattern noise (FPN) which can be reduced considerably by subtraction a background noise signal from the spectral signal Also it is worth pointing out that the PDA described in this work had a dc offset count (~ 45 average counts) which is necessary for correct operation of the ADC and is present on all signals recorded Random fluctuations in all components of the detection system (e g CEMA gain, laser energy etc) can be reduced by averaging a number of shots (typically 10)

2 8   JK Lasers™ ruby laser

A JK Lasers™ ruby laser operating in Q-switched mode was used to generate the plasma in most experiments reported in this thesis The laser was of the single oscillator type and provided ~ 1 J (@ 1 85 kV capacitor charging voltage) with a pulse length of 35 to 45 ns at a wavelength of 694 3 nm The ruby rod consists of a crystal of aluminium oxide Al_2O_3 in which some of the Al^{3+} ions were replaced by Cr^{3+} ions The lasing medium was pumped by a Xenon flash-lamp A Pockels cell combined with a polarizer was used to provide Q-switching The Pockels cell is normally biased to prevent lasing and the high voltage is removed to allow for an intense pulse to be generated

Ruby crystal

Output mirror

Pockel cell

He Ne alignment laser

Rear mirror

Stack of plates polarizer
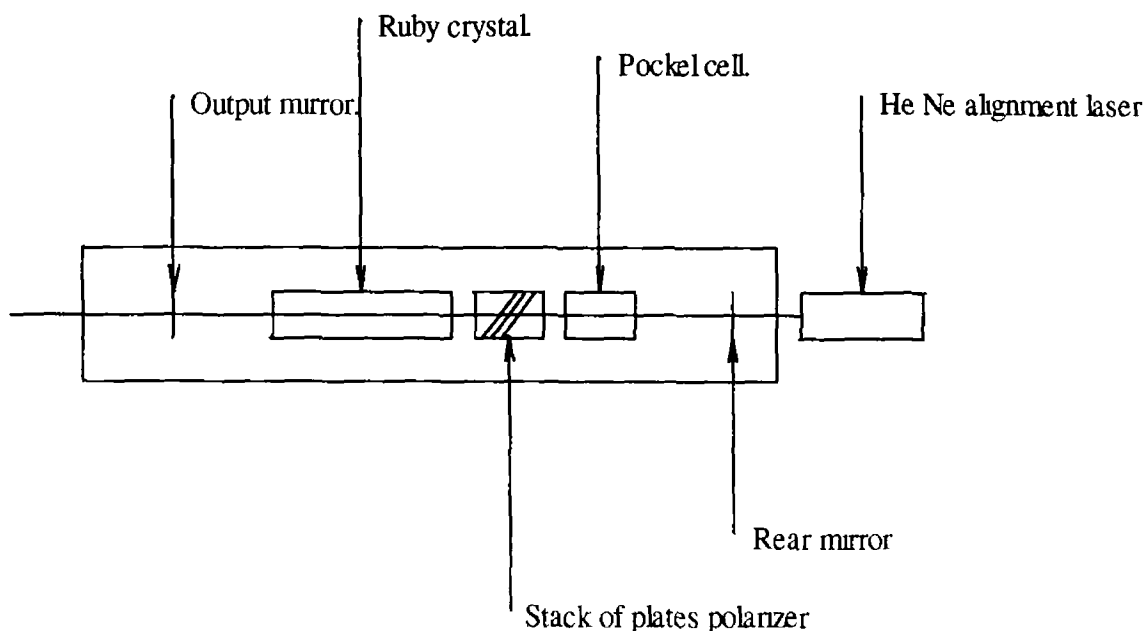
Figure 2-6   *Schematic of the JK Lasers™ ruby laser*

2 9   Spectron Laser Systems™ Nd   YAG lasers

The laser used in the initial experiments was a Spectron Laser Systems™, Q-switched Nd   YAG SL803 laser featuring a two stage oscillator / amplifier configuration This system yielded an output pulse energy of ~ 690 mJ in ~ 15 ns @ 1064 0 nm and was used for producing the continuum plasma Also used was a Q-switched Nd   YAG SL404 laser which did not have an amplifier stage This laser was predominantly used for the production of the absorbing target plasma and had an output pulse energy which was measured to be ~ 170 mJ with a pulse duration of 15 ns @ 1064 nm

Rear mirror assembly Nd Yag rod

Intra cavity telescope Output coupling mirror and safety shutter

Pockells cell 45 degree corner beam steering mirrors

He Ne alignment laser

Beam expanding telescope

Amplifier chain
SL803 only

Front dichroic mirror
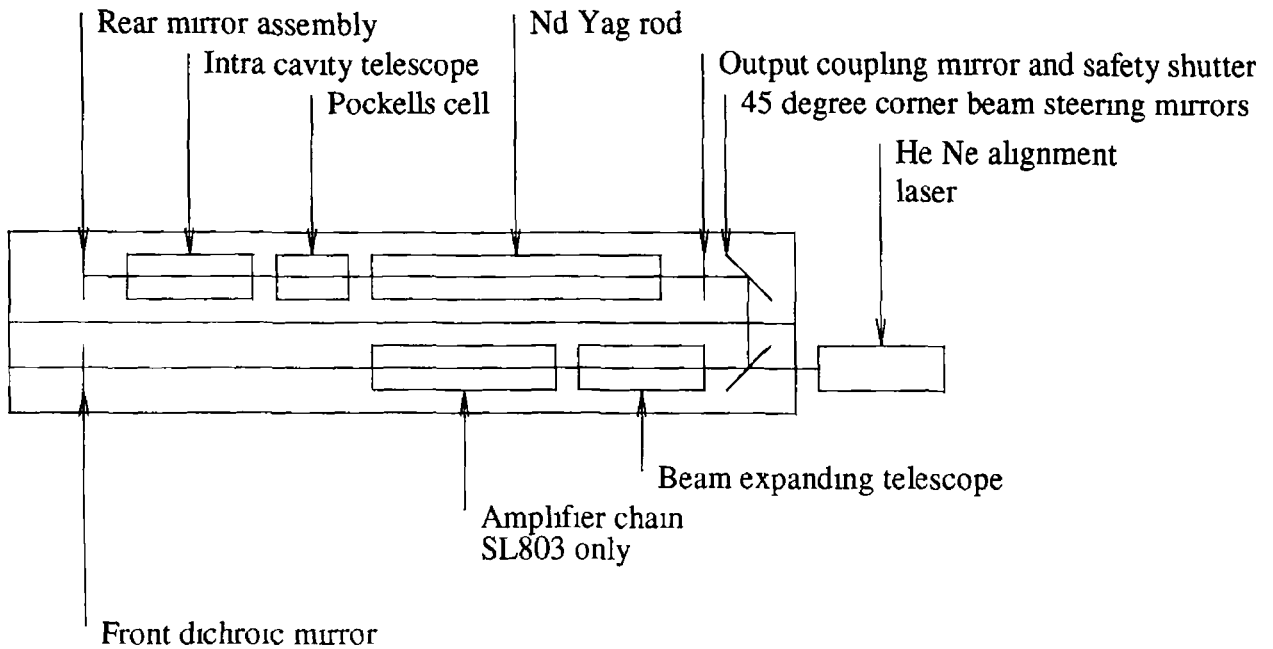
Figure 2-7 *Schematic of the Spectron Laser Systems™ Nd YAG lasers (SL803 and SL404)*

The lasing medium consists of a rod of crystalline yttrium-aluminium-garnate (YAG, Y_2 AL_5 O_{12}) doped with neodymium (Nd^{3+}) ions The crystal is pumped to a state of population inversion by a flash-lamp close coupled in a diffusion cavity A Pockels cell / polarizer combination is used to inhibit normal lasing action until a Q-switch trigger pulse is received This can be either internally or externally triggered A Stanford pulse delay generator with 5 → 15 V step-up switches is used to fire all flashlamps and Pockels cells in synchronisation for laser pulse timing on a nanosecond timescale

2 10 Target chamber and vacuum system

For the study of electromagnetic radiation at wavelengths, less than 200 nm it becomes necessary to work under vacuum conditions due to the significant attenuation of radiation by atmospheric gases The spectral region λ < 200 nm is generally referred to as the vacuum ultra violet (VUV) Below $\lambda \cong 0\ 2$ nm the atmosphere becomes transparent again and therefore wavelengths of about 0 2 nm can therefore be regarded as the lower wavelength limit of the VUV One can further divide this spectral range into sub regions depending on the type of spectrometer required For example, the region between about 30 nm and 200 nm has been termed the normal incidence region, and the region between about 3 nm and 30 nm is quite

often referred to as the grazing incidence region It must be stressed that no formal definitions of spectral ranges in the VUV exist and the regions do overlap somewhat
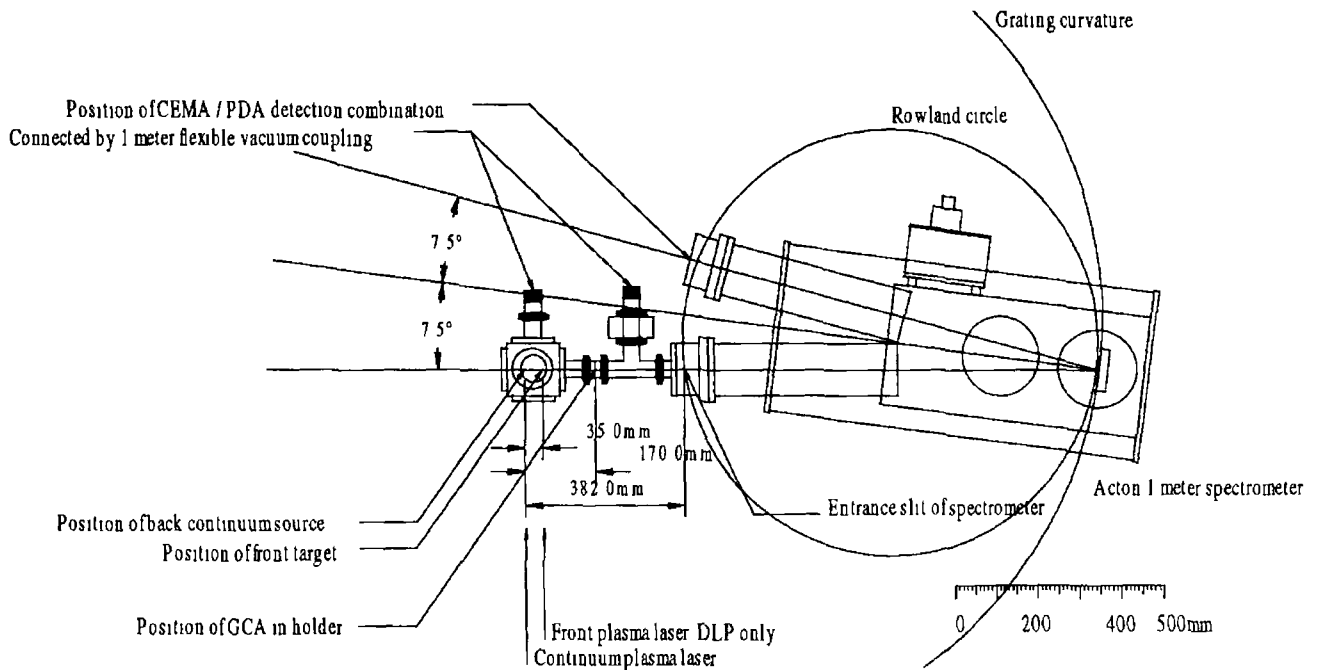
Figure 2-8 Schematic of direct coupled spectrometer arrangement showing main dimensions between optical components

2.10 1 Vacuum pumps

A number of vacuum pumps were used throughout the experiments to pump the spectrometer and target chambers The target chamber was pumped using a turbo mechanical and rotary pump combination The spectrometer was pumped using a turbo mechanical pump, with the ion pump taking over once a pressure of 10^5 mBar was reached A full schematic of the vacuum arrangement used is shown in Figure 2-9
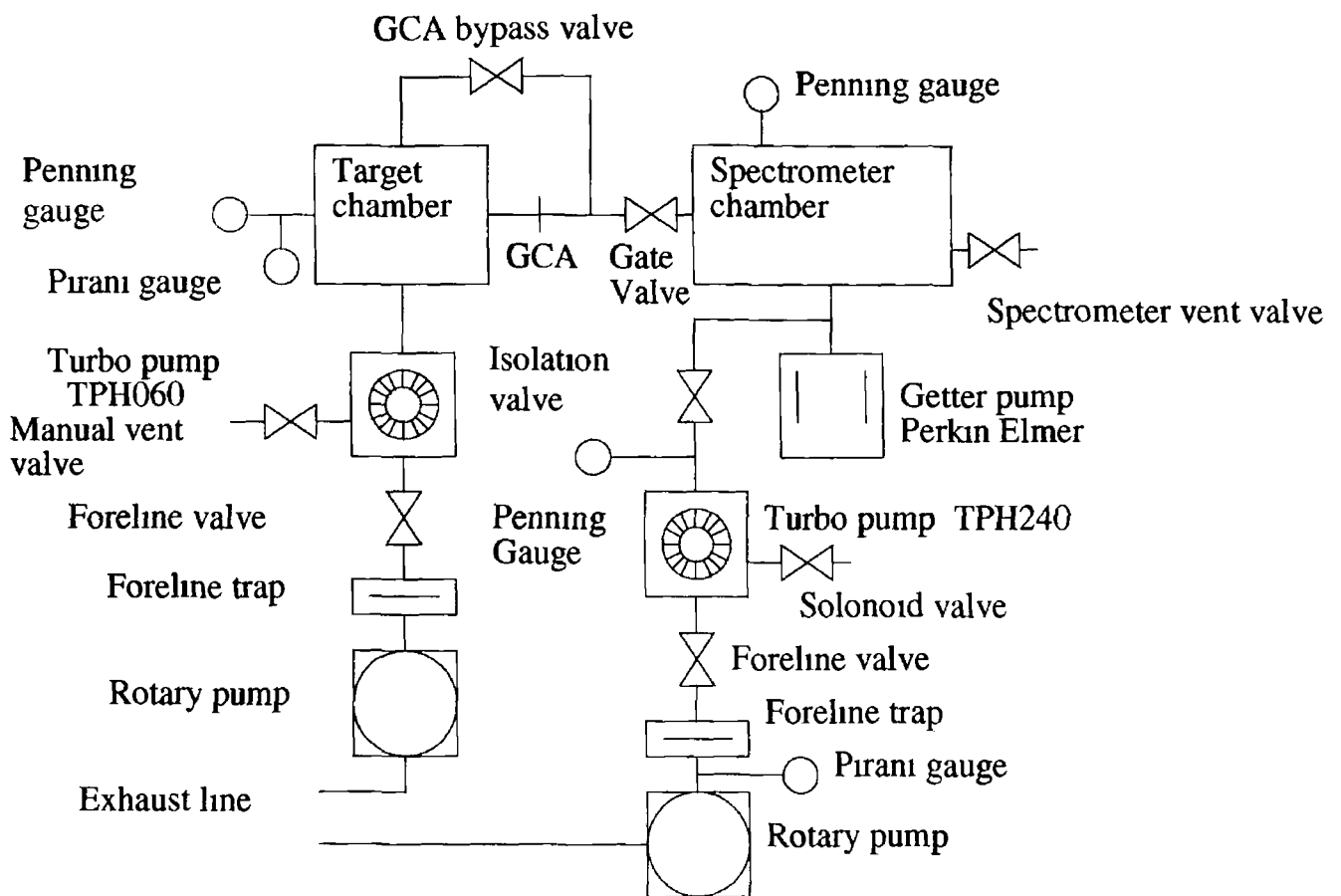
Figure 2-9   *Schematic of vacuum system showing set-up used with direct connection of target chamber to spectrometer chamber*

Typical operating pressures were 9 7 * 10^7 mBar in the spectrometer chamber and 7 * 10^6 mBar in the target chamber The pressure differential between the spectrometer and target chamber was primarily across the GCA It is possible to increase this differential pressure e g for gaseous absorption studies, of up to ~ 10^2 for steady state and higher for small periods of time (i e less than ~ 3 mins) If a CEMA based intensifier is being used it is important that the pressure in the spectrometer is never allowed to increase beyond 2 * 10^{-6} mBar With the use of the back thinned CCD no limitation is imposed but the pumps require a minimum of 10^5 mBar at the inlet ports for correct operation and to prevent back streaming of oil from the rotary pumps

2.10.2 Vacuum component design

The target chamber consisted of an aluminium cube of edge 126 mm with each face drilled to provide holes of 68 mm in diameter This resulted in a chamber

with vacuum connections on all six sides The target chamber was supported by an *in-house* constructed base facilitating attachment of the TPH060 turbo pump and pressure gauges The entrance window consisted of a 6 mm thick BK7 glass plate held in place by a collar with a o-ring seal between the plate and the target chamber A dual target holder flange suitable for connection to the target chamber was designed and constructed (see figure 2-12) The flange allows translational (both across the optic axis and vertically) as well as rotational movements of the target holder The vacuum seal on each of the target holder bars was made through the use of a Wilson seal This resulted in a target chamber which was vacuum compatible with the spectrometer with or without the GCA in place A GCA holder was designed and built (see figure 2-11) which allowed the GCA to be both rotated and positioned close to the target chamber The holder incorporated a mask which allowed an unused section of the GCA to be rotated into place when plasma debris built up The holder was 50 mm in length and facilitated connection to 40 KF flanges at either end

In order to couple the back thinned CCD camera to the spectrometer an intermediate flange was constructed This was constructed from aluminium and had an o-ring seal on one face The thickness of this flange was machined to 57 mm so that the focal plane of the spectrometer would be coincident with the front face of the detector Replacement flanges for the spectrometer were constructed which allowed the attachment of a pressure gauge close to the spectrometer's chamber and incorporation of a window which made it possible to view the grating The ability to view the alignment HeNe laser footprint on the grating with the system under vacuum proved crucial in the alignment of the system

4*M4 for attaching detector

30 0°

112 5mm
105 0mm

139 5mm

6*M6 for connection to spectrometer

Spectrometer focal plane

40 0mm

52 0mm

90 0mm

152 0mm

40 0mm

2 5mm

152 0mm

57 0mm

64 0mm

Figure 2-10   Schematic of adapter flange for use with Andor Technology™

InstaSpec IV back thinned CCD Dotted line indicates spectrometer's focal plane

2mm thick o ring
Diameter 18mm

18 0mm

2 0mm

15 8mm

39 0mm

12 8mm
3 0mm

Part 2 shown separately
Thickness 3mm

5 0mm

2 5mm

3 0mm

12 5mm

3 0mm

15 8mm

26 0mm

45 0mm

40 0mm

69 9mm

18 5mm
21 5mm

3 0mm

40 0mm

6mm diameter bore
Plate fixing screw holes
3mm diameter Plastic screw
to be used for fixing

Figure 2-11   Schematic of GCA holder
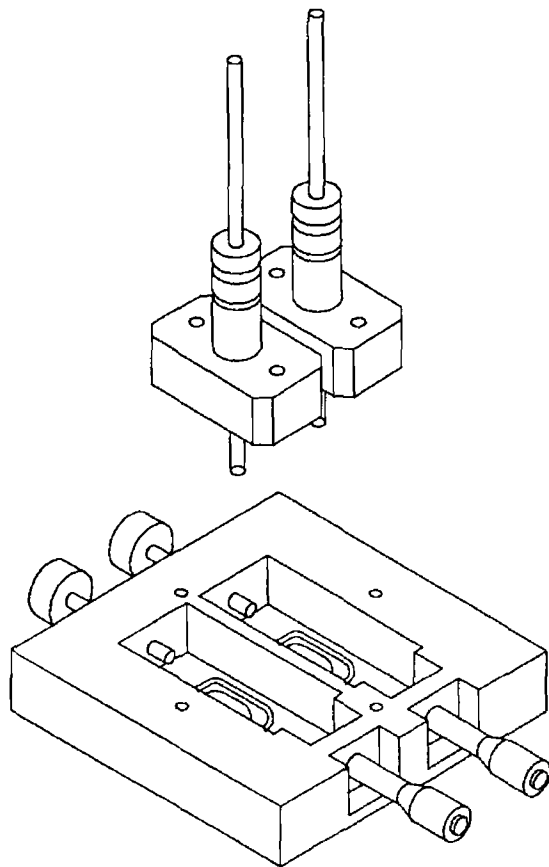
Figure 2-12   Schematic of target holder flange showing the two target holders Centre to centre spacing between target holders   47 mm. Maximum movement possible in x-axis direction   15 mm. Hole size for continuum target   30 * 22 mm Hole size for absorber target or spatial slit / aperture   30 * 20 mm.
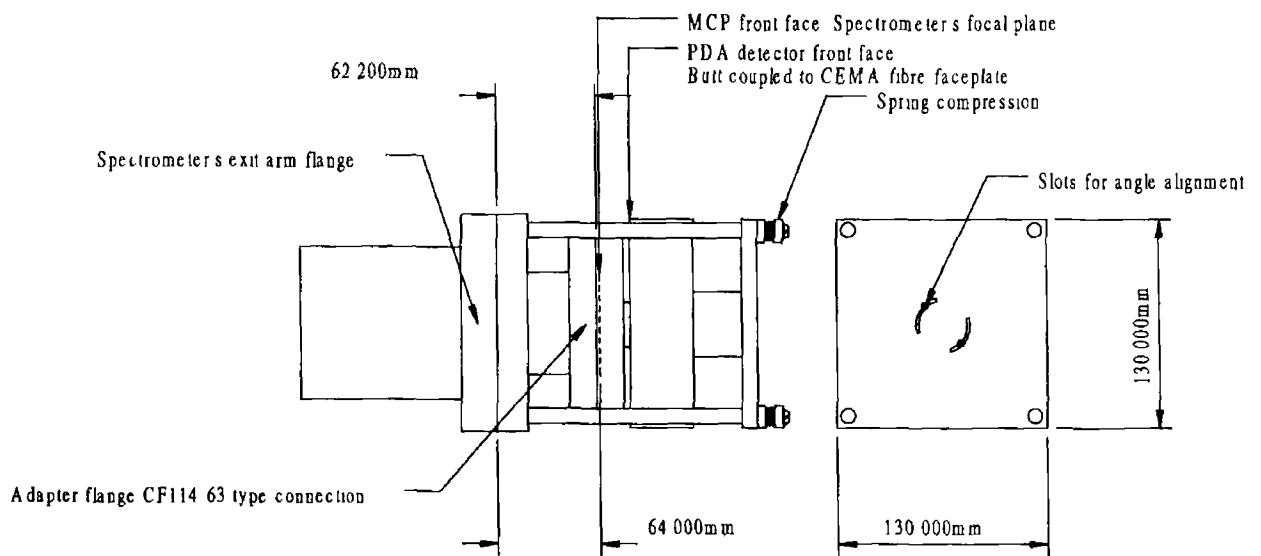

Figure 2-13   Schematic of CEMA / PDA detector arrangement [Doyle, 1995]

60

Chapter 3   Results and discussion.

Experiments carried out with the use the Acton™ normal incidence VUV

spectrometer are described here Various system configurations and detectors were

used during these experiments and are highlighted at the beginning of each relevant

section The results include emission studies of plasmas with line or continuum

dominated spectra, VUV photoabsorption by helium gas, and also photoabsorption

studies with the dual laser plasma (DLP) technique The chapter concludes with

results on spatially resolved YBCO ($YBa_3Cu_5O_{7\,\delta}$) plasma VUV emission

3 1   Line dominated laser plasma spectra carbon and beryllium oxide

Line dominated spectra are useful for characterising a spectrometer

instrument in terms of wavelength calibration, resolution, sensitivity and dynamic

range In addition they are useful in plasma diagnostics, e g to estimate peak plasma

temperature by observing the peak ion stage present in the spectrum If the

wavelength resolution is such that spectral lines display their true line width (i e

instrument function width is much less than typical plasma line width) then

estimates of the electron densities can also be made Line dominated plasmas also

serve to optimize detector alignment and focusing

3.1 1   Carbon emission spectra

Carbon is an ideal reference spectrum for use in the VUV region It has

strong discrete features, which can have narrow line widths under appropriate plasma

conditions and which can make it possible to estimate the system wavelength

resolution Most lines of the CI to CVI spectra have been classified [Kelly, 1987 and

NSRDS-NBS 60] and hence accurate estimates of the plasma ion stages present and

also some plasma parameters (e g electron temperature) can be made Because the

known lines extend well into the UV and VUV spectral regions this allows estimates

of the degree of order overlapping present and combined grating and detector

efficiency over the wavelength range to be made Figures 3-1 and 3-2 show the

observed multiple laser shot (corresponding to the accumulation of ten spectra from

ten successive laser shots) emission spectrum of a polyethylene laser produced

plasma with both the Andor™ back thinned directly illuminated CCD and the Galileo™ CEMA / EG&G™ PDA detectors[†]. Both spectra show strong line dominated emission with very little underlying continuum. In the case of the CEMA / PDA detector the width of the narrowest spectral lines observed as measured at full width half maximum (FWHM) is 6 to 7 pixels (linear dispersion : 0.021 nm pixel^{-1}), while with the improved spatial resolution with the back thinned CCD means that the same spectral lines are much narrower at about 2 to 3 pixels (linear dispersion : 0.022 nm pixel^{-1}).

From a comparison of figure 3-1 and 3-2, it can be seen that the relative intensities of the emission lines are different for the two detector arrangements. This can be attributed to different plasma conditions such as on target irradiance and position of the plasma relative to the spectrometer's optical axis as well as differences in detector efficiency. The CEMA / PDA polyethylene emission spectrum of figure 3-1 shows improved signal at wavelengths greater than about 120 nm than that obtained with the use of the back thinned CCD detector.

[†] All wavelengths mentioned are actual calibrated values unless otherwise indicated. The spectrometer's dial was found to be ~ 5.9 nm (approximately constant over the 30 to 325 nm range) lower than actual centre wavelength.

Figure 3-1   *Single shot polyethylene (C_4H_8) plasma emission spectrum observed with the Acton™ 1 metre normal incidence spectrometer in the spectral range 20 to 220 nm A Galileo™ CEMA based intensifier with an EG&G™ PDA detector was used to record the spectral signal The spectrometer slit width was set at 50 µm Laser Ruby ~ 1 J, 25 – 35 ns (FWHM) @ 694 3 nm*
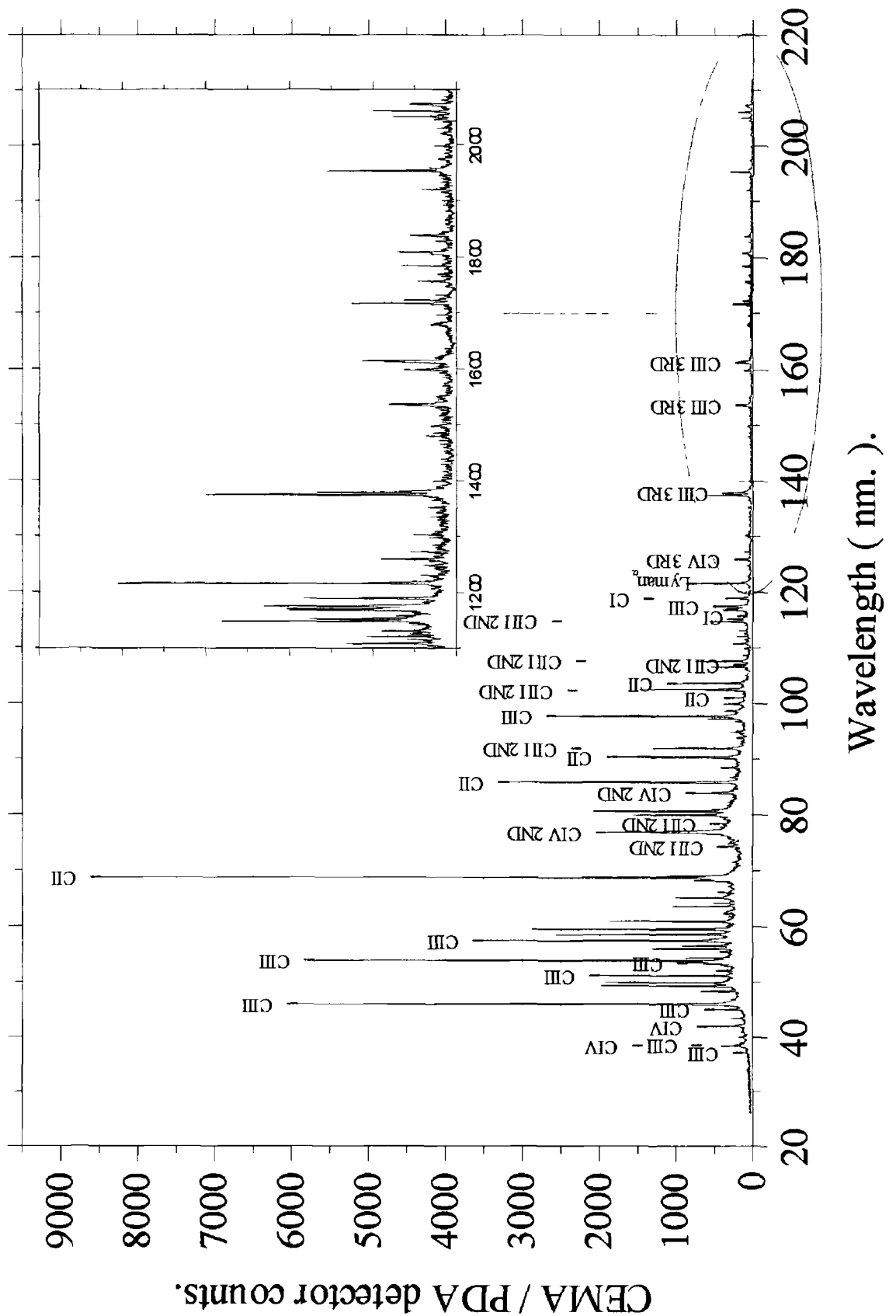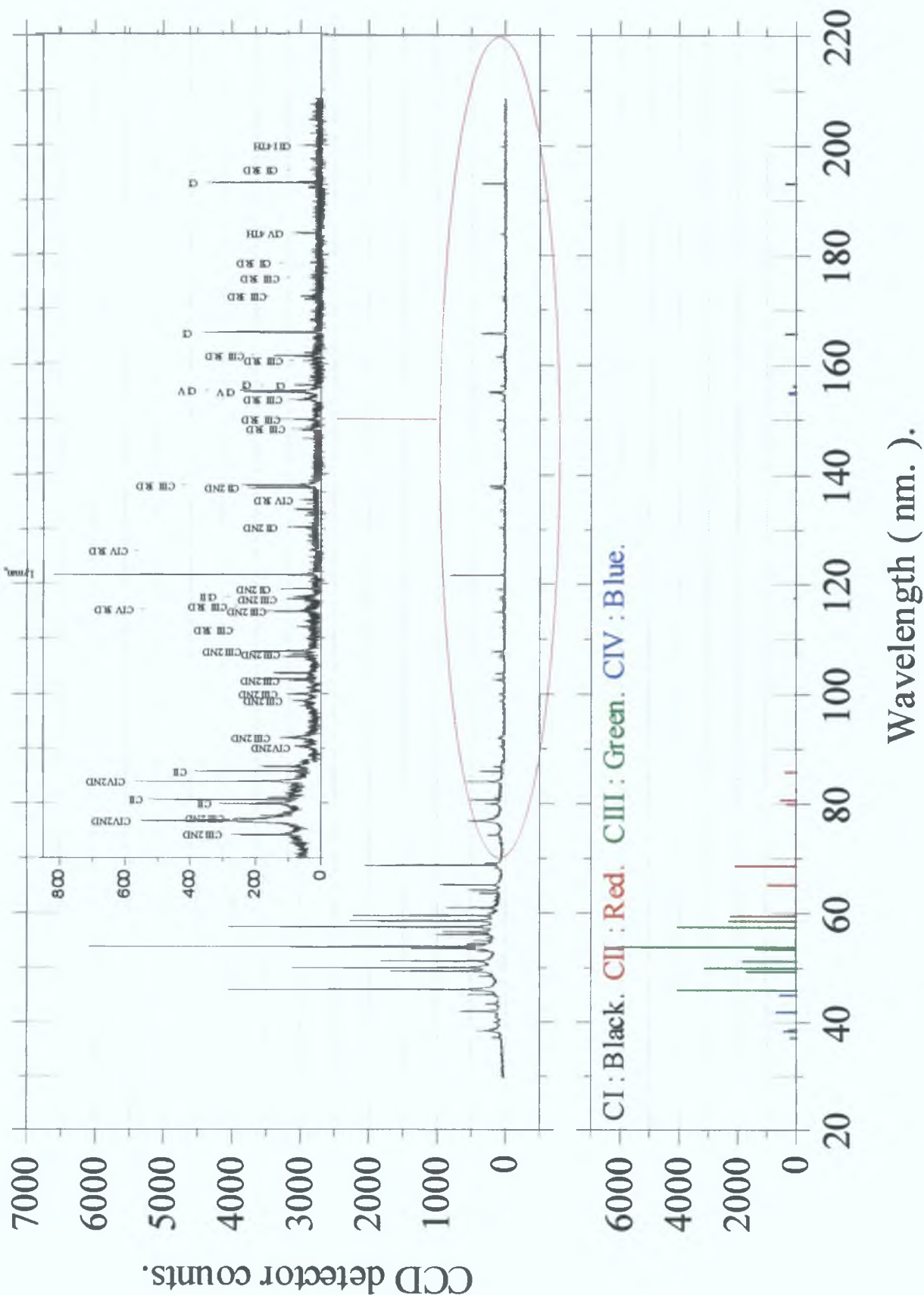
Figure 3-2. *Single shot polyethylene (C_4H_8) plasma emission spectrum observed with the Acton™ 1 metre normal incidence spectrometer in the spectral range 20 to 220 nm. An Andor Technology™ back thinned CCD was use to record the spectral signal. The spectrometer slit width set at 50 μm. Laser : Ruby ~ 1 J, 25 – 35 ns (FWHM) @ 694.3 nm.*

3.1.2 Beryllium oxide emission spectra

The laser produced plasma emission from beryllium oxide is dominated by intense oxygen lines in the normal incidence VUV region The near complete absence of beryllium spectral lines in this region makes this material ideal for observing the pure oxygen spectrum As a surface contaminant, oxygen lines are usually present in spectra of most metal plasmas, especially for the first few laser shots and the ability to identify these impurity lines in subsequent recorded spectra is important The single shot sensitivity of the PDA / CEMA detector arrangement for the study of emission spectra in the wavelength range 30 to 220 nm is clearly seen in figure 3-3 where the spectral signal is well above the underlying noise Most of the lines were identified using reference tables [Kelly, 1987 and NSRDS-NBS 60] and correspond to transitions in ion stages from O^+ to O^{4+} Second order lines begin to dominate the spectrum at wavelengths greater than ~ 100 nm while third order lines begin to dominate at wavelengths greater than ~ 150 nm There are a significant number of lines which could not be identified despite attempts at matching with transitions in lower ion stages of beryllium or the impurity element of carbon Their origin remains an open question

The oxygen emission spectrum is such that most of the observed spectral lines are the result of a number of close lying transitions which are not resolved in first order with the instrument used However some of the more intense lines are seen up to fourth order and the increased resolution results in some of the components of such lines being resolved

The order overlapping present in spectra recorded on the Acton™ instrument is also illustrated in figure 3-3 The poor efficiency of the grating at wavelengths below about 48 nm means that second order light is only significant at wavelengths greater than approximately 95 nm and third order light greater than approximately 170 nm The decrease in efficiency of the grating at wavelengths greater than 100 nm and the decrease in intensity of the plasma emission results in very few first order lines observable at wavelengths greater than 95 nm
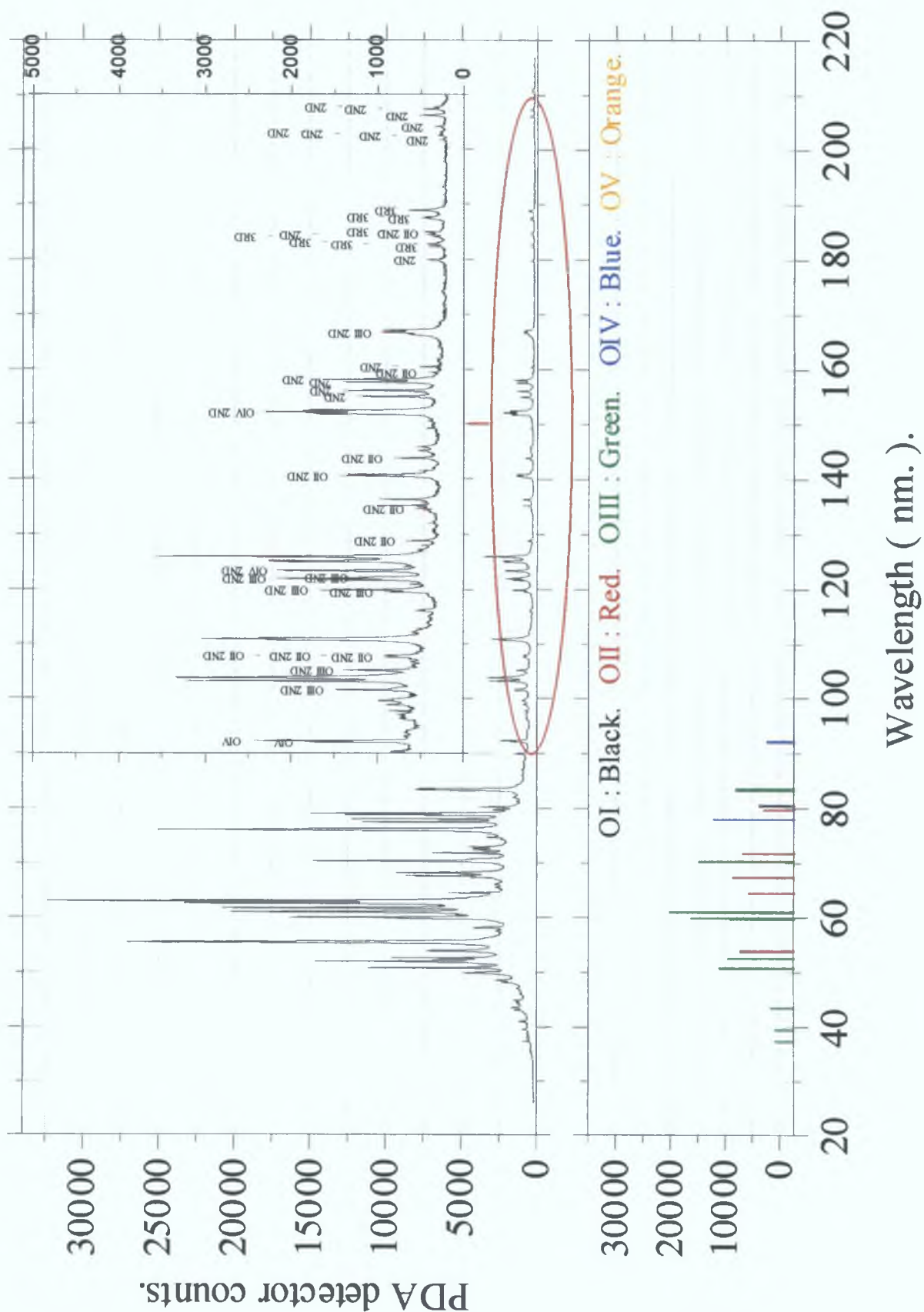
Figure 3-3.   *Single shot beryllium oxide emission spectrum observed with the Acton™ 1.0 metre normal incidence spectrometer in the spectral range 20 to 220 nm. A Galileo™ CEMA intensifier with an EG&G™ PDA readout was used to record the spectral signal. The spectrometer slit width was set at 50 μm. Laser : Nd : YAG, ~ 690 mJ, 15 – 25 ns (FWHM) @ 1064 nm.*

3.2 Continuum dominated laser plasma spectra samarium and tungsten

The continuum-dominated emission from high atomic number targets has already been discussed in terms of importance in photoabsorption studies and other applications such as photoelectron spectroscopy and VUV reflectivity measurements The common requirement of these applications is not so much a 'line free' but more a reproducible continuum Studies on the extent of the continuum observable with the Acton™ VM-521 spectrometer as well as structure, flux and reproducibility are discussed in the following sections

3 2 1 Samarium continua dominated emission spectra

A samarium (Sm, Z = 62) plasma, formed using a cylindrical shaped target with diameter 6 mm was used for continuum generation in most of the experiments described here Samarium is a lanthanide group metal which has a silvery-white appearance It is relatively stable in air but oxidises on contact with moisture It is quoted as been harmful and noxious and hence may involve limited heath risk if ingested or if it penetrates the skin

Laser produced samarium plasmas generally exhibit line free continuum emission over the range 4 to 200 nm with weak line emission superimposed on the continuum mainly around 125 nm This means it is an ideal backlight for use in normal incidence VUV absorption experiments It was also chosen for these experiments because in the spectral region of interest for resonant absorption by helium gas (~ 50 4 nm) the intensity of the samarium plasma emission has a maximum within the normal incidence wavelength range [Carroll et al, 1983]

A full scan of the samarium spectrum throughout the range of the Acton™ VM 521 spectrometer was performed using the Andor™ back-thinned CCD detector The output from the back-thinned CCD reached 2 5 * 10^4 counts @ 45 nm for the accumulation of 10 shots with the spectrometer slit width set at 50 μm, corresponding to 2 5 * 10^3 counts pixel[1] per laser shot or ~ 13 % of pixel saturation
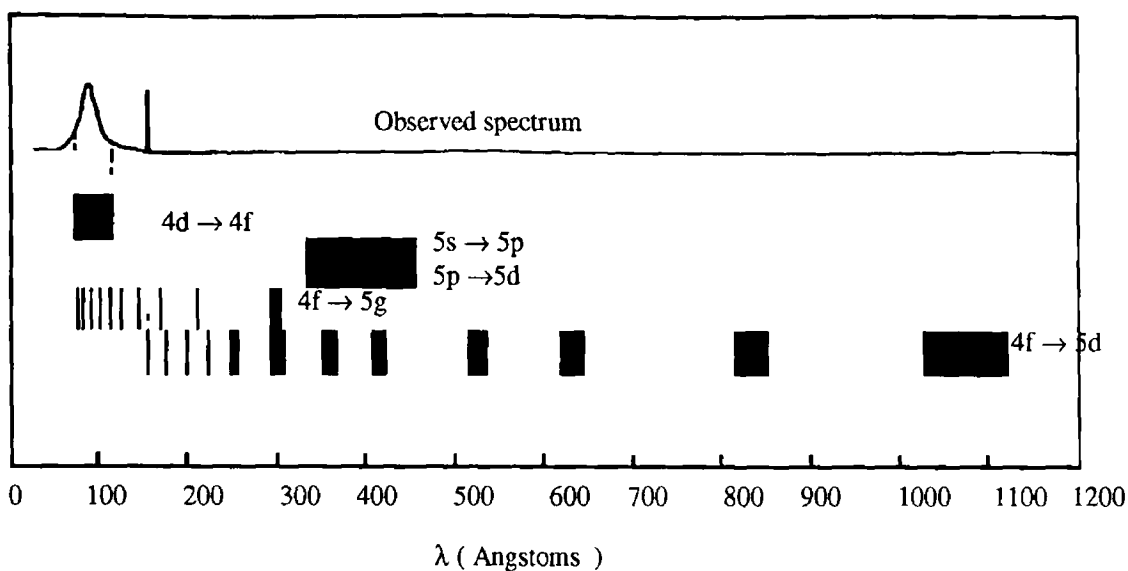
Figure 3-4   Schematic spectrum of samarium showing the calculated approximate position of the strongest transition arrays [O'Sullivan, 1983]

Figure 3-5   Samarium continuum emission observed by the Acton™ VM 521 normal incidence spectrometer in the range 20 to 220 nm. An Andor Technology™ back thinned CCD was use to record the spectral signal   The spectrometer slit width was set at 50 μm. Laser   Ruby ~ 1 J, 25 – 35 ns (FWHM) @ 694 3 nm.

3.2 2   Tungsten continuum dominated emission spectra.

The XUV continuum from a laser produced tungsten plasma is ideal for use in photoabsorption experiments as it has a reproducible and reasonable 'line free' structure In the longer wavelength normal incidence VUV region the number of discrete lines present increases and arise from transitions within lower ion stages of the tungsten plasma as well as impurities present such as oxygen Although the presence of these lines can degrade the quality of photoabsorption measurements taken with such continua in practice the overall structure is reproducible Hence it tends not to affect transmission (I/I_0) measurements Although samarium has less visible line structure superimposed on the underlying continuum and the overall intensity is greater in the normal incidence VUV region, samarium is a softer material and therefore the position of the target must be changed more frequently than that of tungsten Also the fact that the samarium target used in the experiments described here was of a cast form and hence was not perfectly cylindrical, when both targets are rotated to provide a fresh surface the tungsten target will deviate less from it's previous position

Figure 3-6   *Tungsten continuum emission as observed by the Acton™ VM 521*
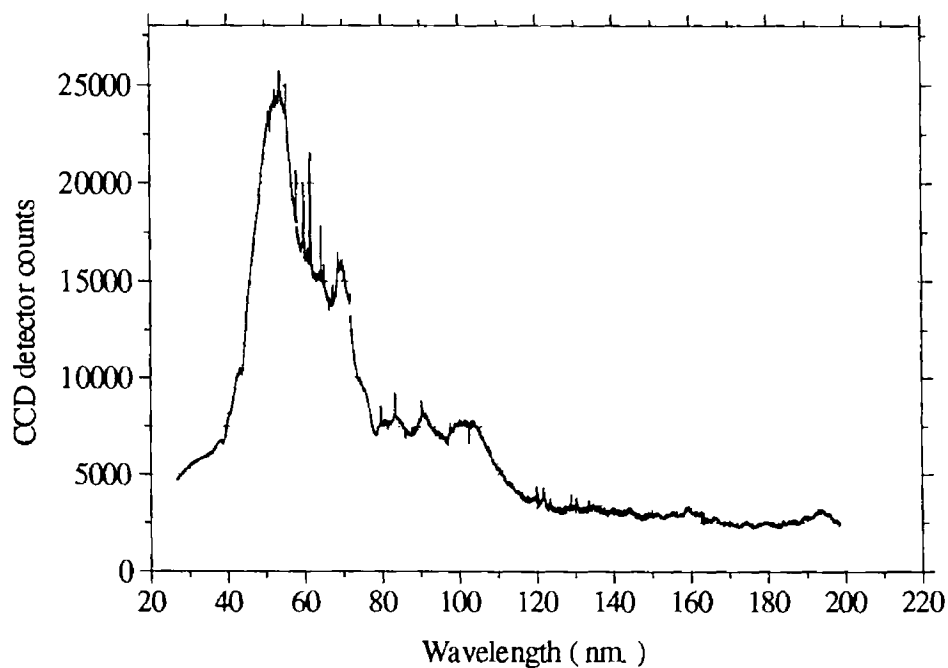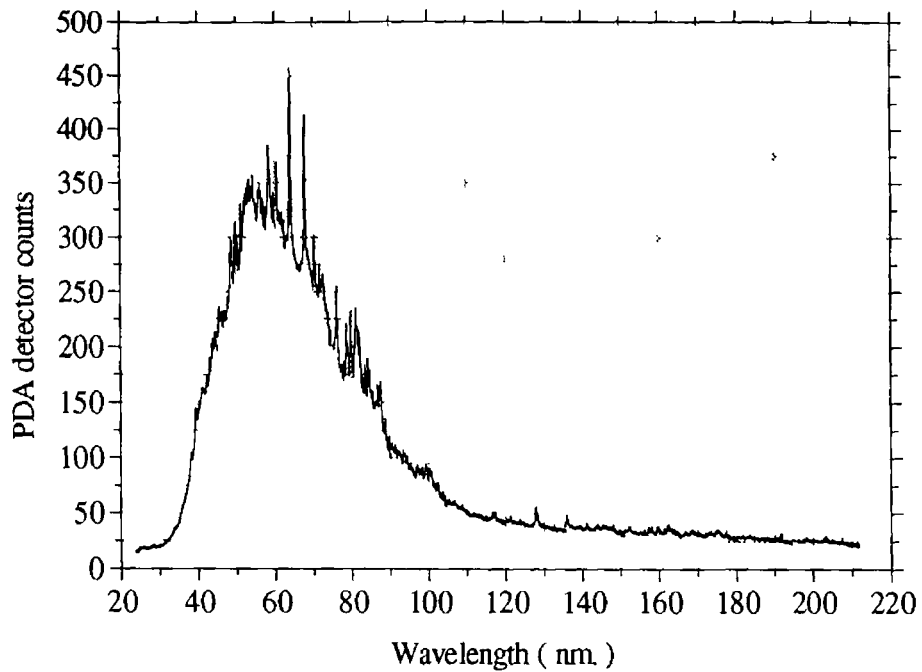
normal incidence spectrometer in the range 20 to 220 nm. A Galileo™ CEMA based

intensifier with an EG&G™ PDA detector was used to record the spectral signal

Spectrometer slit width set at 50 μm Continuum plasma excitation laser Nd YAG

~ 690 mJ, 15 – 25 ns (FWHM) @ 1064 nm

3.2 1   Accuracy and precision of mechanical movement of grating

In order to quantify the reproducibility of the wavelength scanning mechanism for the Acton™ VM 521 spectrometer a series of spectra were recorded over the range 30 to 200 nm in steps of 15 nm with the grating moved over the full range in between scans Inspection of the pixel position of spectral lines showed that theie weie no relative peak shifts thus indicating that the scanning mechanism was indeed reproducible to within the pixel dimension of 25 μm Also initialising the stepper motor drive (1 e turning the drive off and on) had no effect on the pixel positions over the entire range Although manual movement of the scanning mechanism to zero order (dial position ~ 9933) resulted in a shift in the pixel position of a number of lines by one pixel, this shift was not observed with all lines

and therefore is more likely to do with changes in line structure and profile due to source fluctuations

This shift of less than a single pixel (~ 0 02 nm) confirms the reproducibility quoted by Acton™ of 0 005 nm The dial reading no longer determines the centre wavelength position accurately and there is an offset which varies slightly over the complete range of the instrument Although the equations governing the motion of the grating (equation 2-10 and 2-11) result in a non linear rotation, the mechanical movement consisted of a sine drive which translates the cam driven stage linearly In the range 20 to 220 nm the offset was measured to be 5 899 ± 0 022 nm It is therefore noted that so long as the detector arrangement is not interfered with, calibration spectra need only be taken once The removal and replacement of the PDA detector can result in an offset of the centre pixel up to ~ 40 pixels

The Galileo™ CEMA / EG&G PDA detector arrangement displayed over a small region at the lower wavelength end of the spectra with depressed pixel counts, indicating that a portion of the detector was shadowed This region extended for approximately 40 pixels from the edge of the detector and was more evident when photoabsorption measurements were taken where the calculation of the relative photoabsorption cross section yielded a high value within this region As the recorded spectra are usually taken with an overlapped wavelength coverage of ~ 50 % or so, these shadowed pixels may be simply ignored
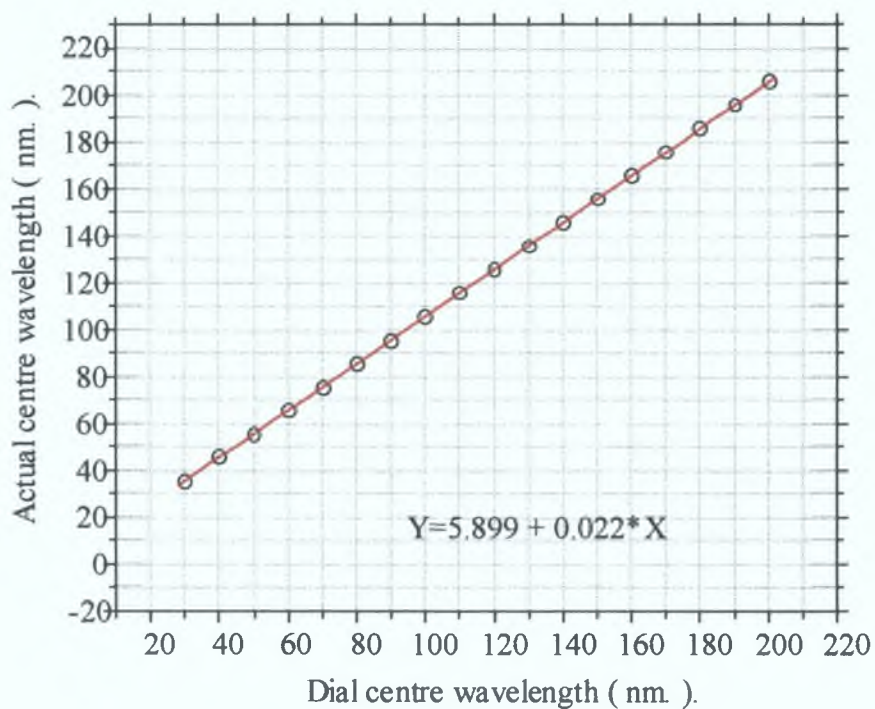
Figure 3-7.   Graph of centre wavelength as read from stepper motor dial versus actual wavelength calibrated with the use of beryllium emission spectra in the wavelength range 25 to 200 nm.

As can be seen from the graph the actual wavelength is 5.9 nm longer than that of the dial reading.

3.2.2   Wavelength resolution comparisons between the two detectors.

In figure 3-8 the emission spectrum of a polyethylene plasma is shown in the limited wavelength range for both detectors where the improvement in wavelength resolution achievable by the Andor™ back thinned CCD is clearly seen. The vast majority of spectral lines recorded by the Andor™ back thinned CCD are at most 3 to 4 pixels in width (FWHM) whereas with the Galileo™ CEMA / EG&G PDA the spectral lines are at most 6 to 7 pixels in width. The wavelength resolution of either detector is not sufficient to resolve the spectral lines to their natural widths. This is confirmed by comparing second and third order lines to their first order counter parts where no increase measured line width is visible.
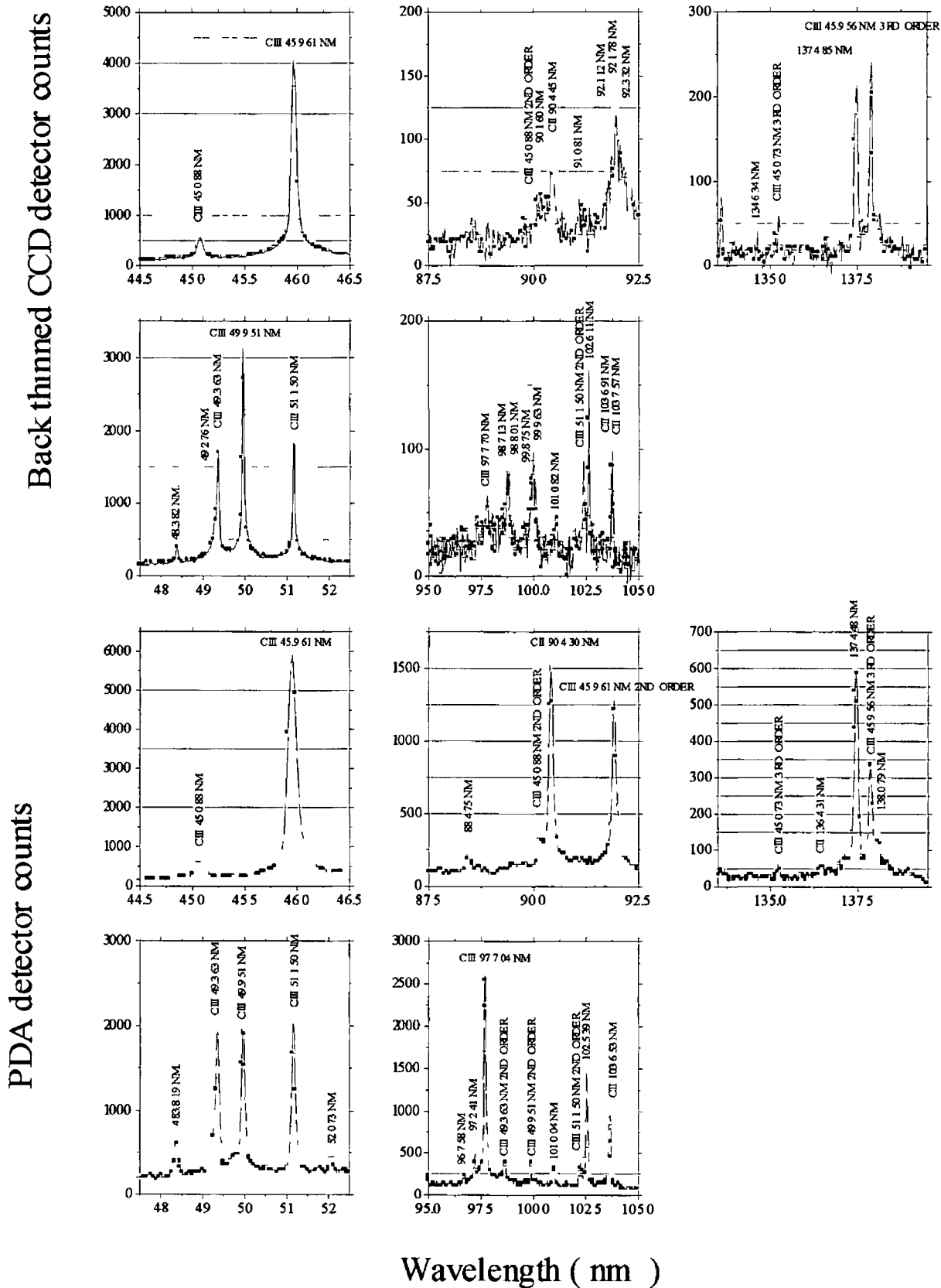
Figure 3-8   Single shot polyethylene (C₄H₈) plasma emission spectra observed with the Acton™ 1 metre normal incidence spectrometer using both (upper two rows) an Andor™ back thinned CCD and (lower two rows) a Galileo™ CEMA / EG&G™ PDA detector Proceeding from left to right the same region is displayed in first, second and third order

3.2.3 Quantum efficiency and dynamic range comparisons between the two detectors.

The efficiency of the grating with respect to wavelength has not been investigated as this would require a calibrated source at least of known relative intensity. Therefore any discussion of the quantum efficiency of the detectors must include a discussion on both the efficiency of the grating as well as radiance of the source. The detected spectra from a specific detector arrangement, $I_{Detected}(\lambda)$ will be a function of the spectral radiance of the laser plasma source, $I_{LPP\ source}(\lambda)$, the efficiency of the grating, $G_{Grating\ efficiency}(\lambda)$, depending on both the reflectance of the coating as well as blazed wavelength and that of the detector, $D_{Detector\ quantum\ efficiency}(\lambda)$. In addition a geometric factor, $F_{Geometric\ factor}(\lambda)$, accounting for the entrance optics of the spectrometer, position and shape of the plasma source is also present.

$$
I_{Detected}(\lambda) = I_{LPP\_source}(\lambda) * G_{Grating\_efficiency}(\lambda)
$$
$$
* D_{Detetor\_quantum\_efficiency}(\lambda) * F_{Geometric\_factor}(\lambda) \qquad [\ E\ 3\text{-}9\ ]
$$

It is evident from emission spectra that the efficiency of the grating determines to a significant degree the overall shape of the continua and relative heights of lines. The short wavelength falloff in efficiency is rapid while the longer wavelength is more gradual. The plasma intensity, $I_{LPP\ source}$, tends to peak at shorter wavelengths and compounds this difficulty in determining the efficiency curve of the grating. With most of the line and continuum dominated emission spectra the peak counts are observed to be at ~ 60 nm. The relative strength of the spectral lines of polyethylene, aluminium and beryllium oxide in second order tend to be as intense as their first order counterparts principally around ~ 80 nm. This suggests that the blaze wavelength of the grating within the Acton™ spectrometer is indeed 80 nm in agreement with the Acton™ specifications.

The quantum efficiency of the two detectors also has an effect on the observed counts for both the continuum and line dominated emission spectra. The Galileo™ CEMA intensifier with the MgF_2 coating has a quoted quantum efficiency of 10 % when detecting normal incidence VUV photons ($\lambda < 1800\ nm$). It is also

evident that the quantum efficiency of the back thinned CCD falls off at lower wavelengths than the CEMA / PDA detector combination The back thinned CCD displays higher dynamic range and lower noise

Generally speaking, the description of the system sensitivity is rather crude because many of the factors involved, such as gain and efficiency of the detection device, are strong functions of other parameters Since the gains of both the MCP and of the phosphor screen are steep functions of applied voltage, and the CCD dark noise also depends on operating temperature, the estimate of the sensitivity is more qualitative than quantitative

3.2 4 Reproducibility of continuum emission from rare earth plasmas

In figure 3-10 the effect of a large number of shots has on the average intensity of the tungsten plasma continuum at a centre dial wavelength of 30, 40, 50, 60 and 70 nm with and without a 525 μm spatial resolving slit introduced 35 mm from the source is shown Once the position of the tungsten plasma has been optimized the average counts are seen to gradually increase over several hundred shots and then gradually decrease The centre of the plateau for each wavelength is observed to tend towards more shots with increasing wavelength Although the number of data points is limited, the inclusion of the spatially resolving slit has the effect of reducing the slope at which the average counts increase at, while not severely effecting the overall intensity
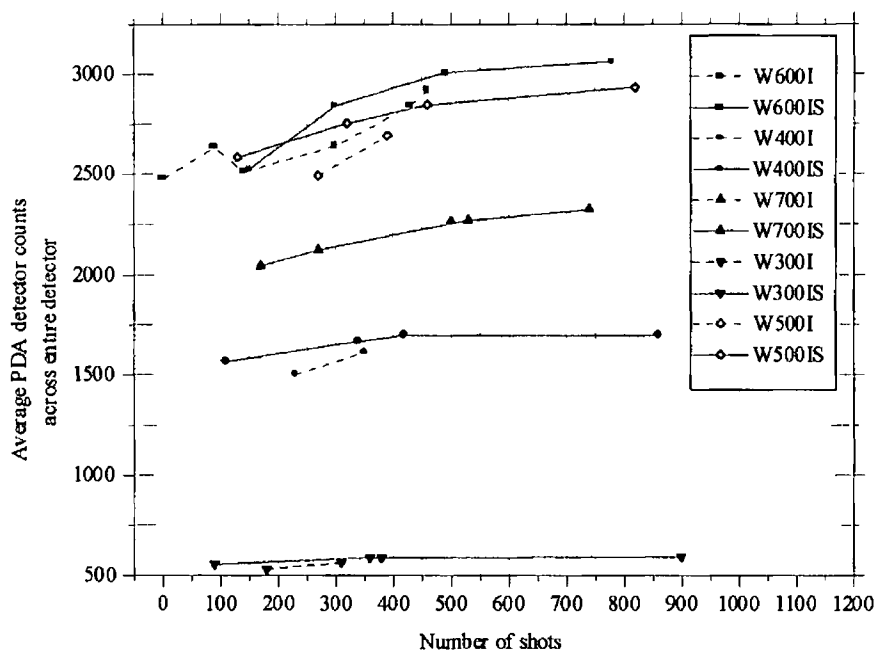
*Figure 3-8   Reproducibility of continuum dominated emission spectra of a
tungsten plasma generated with a Nd   YAG laser, ~ 690 mJ, 15 to 25 ns (FWHM)
@ 1064 nm   Number of laser shots averaged for each recorded spectrum   10   Black
lines represent data collected without a secondary slit present   Red lines represent
data collected with a secondary slit present*

These observations can be justified by considering the extent of the
emitting plasma and the fact that as the focused laser forms a crater increasing in
depth with each subsequent laser shot   Initially the crater is likely to confine the
plasma keeping it hot and hence bright   However as the crater deepens the hot
plasma core becomes increasingly occluded and the detector signal starts to drop
The secondary slit reduces the amount of scattered light entering the spectrometer
system and also reduces the sensitivity of the system to fluctuations in source size

3.3   Helium photoabsorption measurements.

These experiments were carried out with the use of the Andor™ back-thinned CCD and with the target chamber directly attached to the spectrometer entrance slit assembly The GCA was positioned a distance of 170 mm from the target source and 360 mm from the entrance slit The total absorption path length defined by the GCA to plasma source had dimensions of 170 mm A full schematic of the experimental arrangement is shown in figure 3-12 The spectrometer entrance slit width was set at 50 μm throughout the experiments

The target chamber was connected to the region between the GCA and entrance slit via a 40 KF flexible coupling A 40 KF gate valve was inserted in this line to enable isolation of the chamber from this region when leaking helium gas into the target chamber This allowed the small amount of helium gas that leaked through the GCA during an absorption experiment to be pumped out between experiments Also, it was important not to disturb the alignment of the GCA when the target chamber was vented This was only possible if there was no pressure difference on either side of the GCA and was achieved by opening the 40 KF value The spectrometer was pumped using a Balzers™ TPH240 turbo mechanical pump and the pressure was relatively stable at 3 5 * 10^5 mBar throughout the experiments

The laser used to generate the back light continuum source was a JK Lasers™ Ruby laser operating in Q-switched mode It generated a pulse with a duration of ~ 30 ns (FWHM) at a wavelength of 694 3 nm with an energy of ~ 1 J per pulse The laser was tightly focused via a plano-convex lens (focal length   105 0 mm, diameter   22 mm) to an estimated spot size of ~ 150 μm in diameter, thus achieving a power density of ~ 3 * 10^{11} W cm^2

Helium is a much-used gas for absorption measurements It has well known cross sections in the VUV region of the spectrum This makes it ideal for characterising a VUV spectrometer instrument Helium exhibits strong absorption (with a relatively small absorbing column length) by the $1s^2$ (^1S) → $1snp$ (^1P) Rydberg series before the absorption K edge at 50 43 nm

Samarium was chosen for its relatively 'line free' contmuum emission in this region as well as the fact that it is substantially brighter than tungsten in this limited region In addition, samarium displays an average counts profile which has its broad peak in the 40 to 60 nm region Although samarium is not completely 'line free' in the VUV, the spectrum below ~ 100 nm is composed of broad structures which are very reproducible with suitable experimental conditions A measure of the reproducibility of the intensity of the contmuum emitting plasma was made by both monitoring the resulting spectrum as well as observation of the average counts of the detector in successive recorded spectra without the absorbing gas present

The position of the continuum emitting samarium plasma was optimized by maximising the average counts of the entire PDA detector array while adjusting the target position holder (translation across the optic axis, x) and focusing lens assembly (three degrees of freedom, x, y and z) The output energy of the laser used to generate the continuum emitting plasma depended both on repetition rate as well as delay between experimental runs and so the continuum emission also displayed poor reproducibility Figure 3-9 displays a number of the recorded continua Although the shape of the continuum was similar with each shot the intensity varied over a range approximately ~ 20 % Despite attempts at making the contmuum emission more reproducible by incorporating a slit between source and spectrometer and also maintaining the delay between experimental runs constant the reproducibility was not improved significantly Wavelength calibration was performed using the emission spectrum from a polyethylene plasma m a cylindrical rod form This resulted in an emission spectrum with well identifiable carbon emission lines across the entire detector plane

78
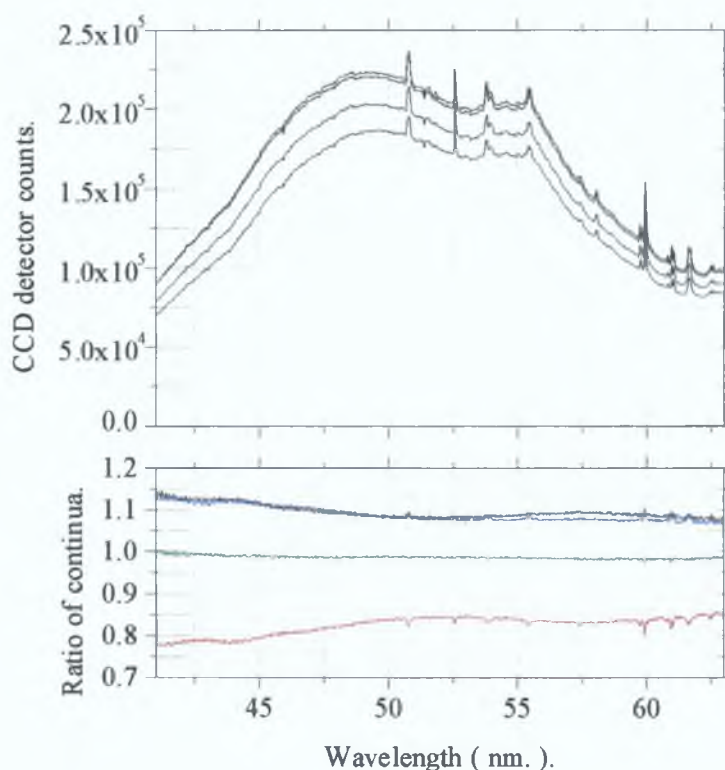
Figure 3-9. *(upper plot) Reproducibility of continuum dominated emission spectra of a rare earth, samarium (Z = 62), plasma for sum of ten laser shots at the center wavelength of 52 nm used in the helium photoabsorption experiments. All of the spectra are within ~ 20 % of the average counts (lower plot) ratio of recorded spectra indicating good reproducibility of features. Laser used : Ruby, ~ 1 J, 25 to 35 ns (FWHM) @ 694.3 nm.*

Helium gas was taken directly from the laboratory piped supply with a quoted purity of 99.993 %. A precision leak valve was used to vary the flow of helium into the target chamber. The target chamber was pumped continuously throughout the experiments using the Balzers™ TPH040 turbo mechanical pump. A relatively stable helium pressure throughout each experiment was achieved by adjusting the leak valve. The range of pressure for each experiment was recorded. Although a small volume of gas leaked through the GCA to the spectrometer side of the GCA, it was found that the amount of helium was so small that it resulted in negligible additional absorption. Therefore the length of the helium absorbing path was well defined as the distance from the continuum plasma source and the face of the GCA.
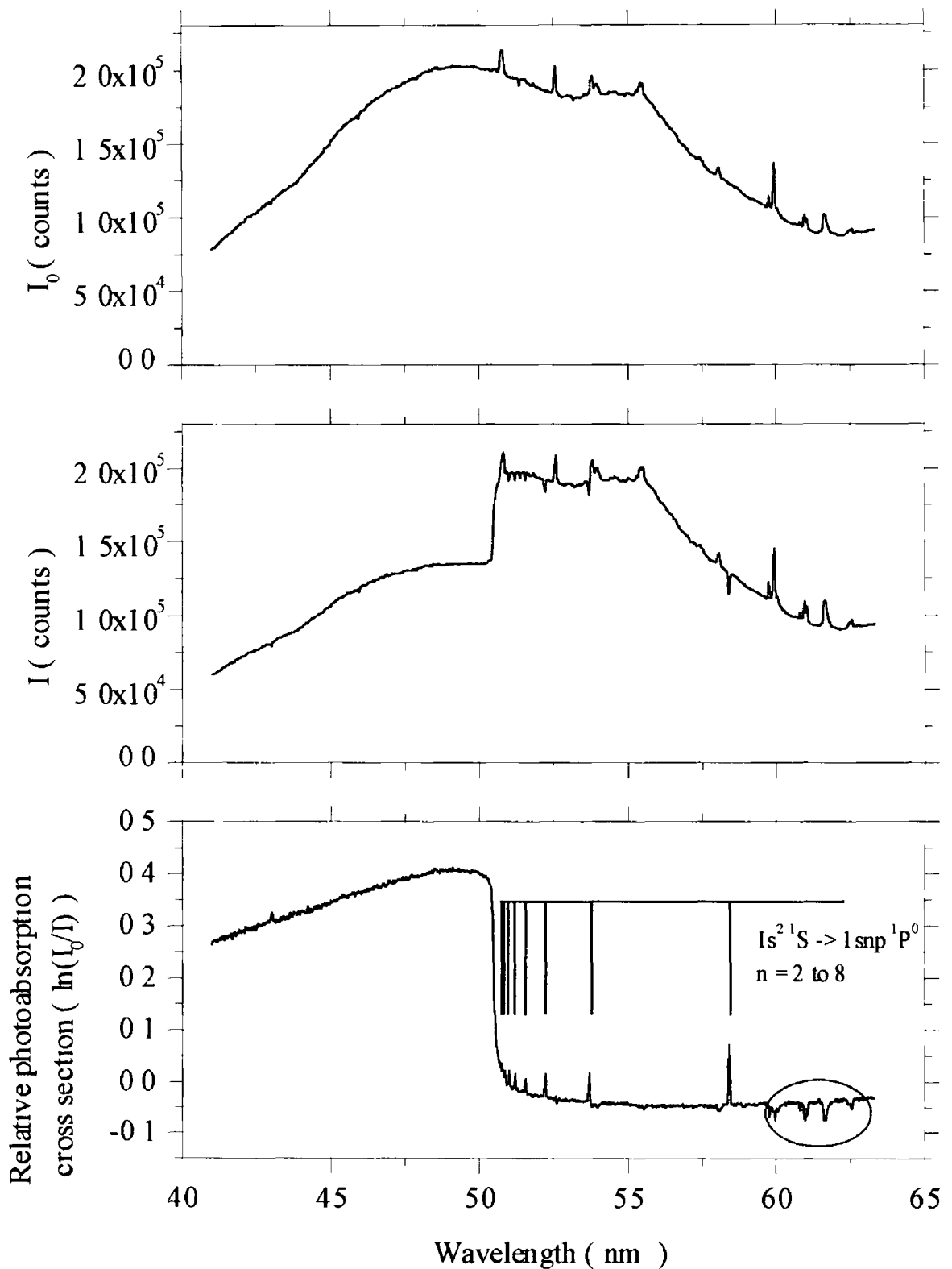
*Figure 3-10   (a) Continuum emission from a samarium plasma, (b) absorption of the continuum emission by helium gas and (c) relative photoabsorption cross section in the wavelength range around the K absorption edge at 50 43 nm corresponding to direct photoionization at the $1s^2$ S limit (Residual helium gas pressure   1 4 * 10^1 mBar, column length   170 mm)   The features circled are the result of changes in backlight emission*

The dramatic K absorption edge at 50 43 nm is clearly seen in both first and second order in figure 3-11 (a) and (b) In first order (λ_{centre} = 52 nm), the reciprocal linear dispersion is ~ 0 022 nm pixel[1] at the detector plane and therefore the observed range is from ~ 41 0 nm to ~ 63 3 nm The helium photoabsorption lines observed are $1s^2\, {}^1S \rightarrow 1snp\; {}^1P^0$ where n = 2 to 8 In second order the reciprocal linear dispersion is ~ 0 011 nm pixel[1] and therefore the observed range is from ~ 46 9 nm to ~ 57 1 nm The helium photoabsorption lines observed are $1s^2\, {}^1S \rightarrow 1snp$ ${}^1P^0$ where n = 3 to 9
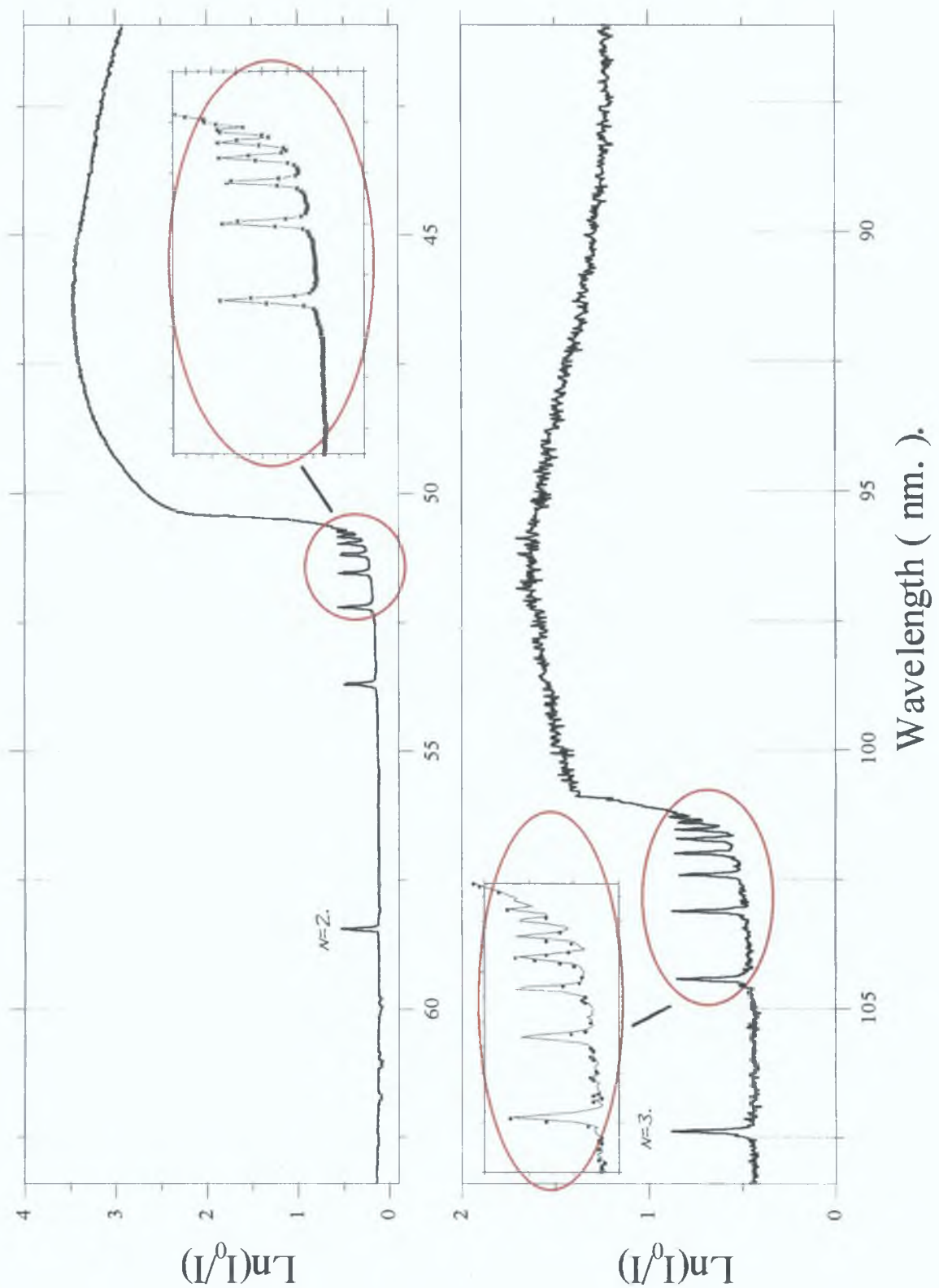
Figure 3-11. (*Left image*) *Image showing full vertical binned image of helium photoabsorption, I, with the use of a samarium laser produced plasma backlight in first order 41.8 to 62.2 nm and (right image) in second order 93.8 to 114.2 nm. Parameters : Absorbing length : 170 mm., Residual helium gas pressure : 2.0 - 2.7 mBar in first order, 2.7 - 3.0 mBar in second order. Absorption lines observed n = 2 to 8 in first order and n = 3 to 9 in second order.*

By calculating the number density of the residual gas species, cross section measurements can be performed on photoabsorption data This allows valuable information of system performance to be collected specifically on effects such as multi-order and scattered light contributions as well as wavelength resolution of the entire spectrometer and detection system

The absolute cross section σ of a particular species is defined by the following expression,

$$Ln\left(\frac{I_0}{I}\right) = \sigma n l \qquad [\text{ E 3-3 }]$$

where σ (m^2) is the absolute photoabsorption cross section, n is the number density of the absorbing species and l (m) is the column length of the absorbing species The number density can be calculated from the following expression,

$$PV = nRT \qquad [\text{ E 3-5 }]$$

where P (Pa) is the absolute pressure, V (m^3) is volume of the vacuum chamber containing the gas (estimated to be ~ 3 5 * 10^3 m^3), n is the number of moles, R is molar gas constant (8 314 J K^1) and T (K) is the absolute temperature of the gas The cross section should not vary as residual gas pressure changes, indicating a linear relationship between $ln(I_0/I)$ and the column length Figure 3-12 shows the calculated cross section versus the residual helium pressure at a number of different wavelengths after the K absorption edge
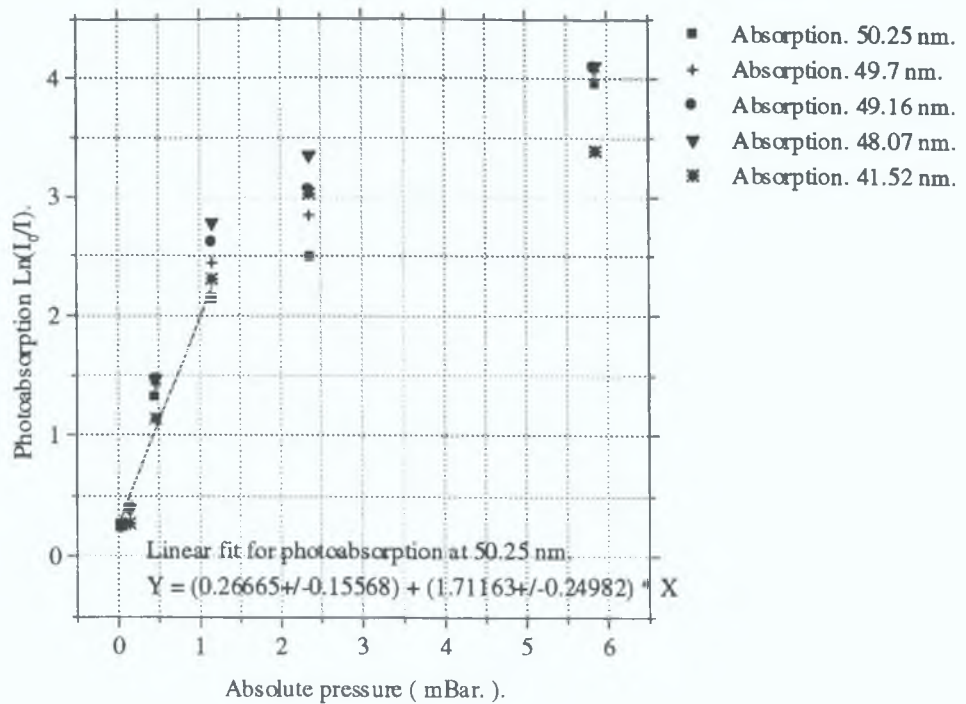
Figure 3-12. Experimentally calculated relative photoabsorption cross section of helium after K absorption edge versus residual helium gas pressure.

From figure 3-12 it is evident that the slope of the relative photoabsorption cross section, $ln(I_0/I)$, versus pressure is only linear for a limited portion of the graph. The non-linearity of the graph at relatively high helium gas pressures indicates that the absorption saturates before complete absorbed signal decreases to zero. The saturation should be insensitive to poor detector resolution and is more dependent on both stray light and detector noise. The poor reproducibility of the backlight emission results in discrete features being present in the relative photoabsorption, $ln(I_0/I)$ plots and a significant offset in baseline signal level.

The principal series running up to the K edge is seen to be largely independent of pressure indicating that the vast majority of data obtained was indeed saturated. The lines do not increase in absorption or increase in width for increasing pressure. Any measurement on the relative photoabsorption cross section for the series is therefore not possible. Stray light, detector resolution and detector noise are all thought to play a part in the saturated signal. Stray light in the form of multiple order light present and also scattered light within the spectrometer system will reduce the saturation limit in photoabsorption experiments. The resolution of the detector

used to record the dispersed spectrum also effects the saturation limit As the gas pressure increases, the relative photoabsorption cross section of the principal series does not increase substantially indicating that these features saturate at lower residual gas pressures

The blaze of the grating used in the Acton™ spectrometer is such that it exhibits a significant drop in efficiency at wavelengths greater than ~ 120 nm Considering that it is blazed at 80 nm and that second order helium photoabsorption results display strong absorption, it is clear that the underlying continuum is truly weak at ~ 100 nm and the observed spectrum is principally second order This is illustrated well in figure 3-12 (b) where the K edge and Rydberg series are clearly seen in second order

In addition, it is noted that the non-zero step in the second order spectra is due to residual first order light at ~ 100 nm passing through the gas with only a small amount of residual absorption The contribution of second order continuum light at ~ 100 nm is estimated to be ~ 62 % and therefore the weak first order contmuum signal prevents photoabsorption studies at wavelengths much greater than ~ 100 nm

Also it is observed that the width of the photoabsorption lines do not change with increasing residual gas pressure or become any more resolved in second order where the linear dispersion is effectively doubled This observation suggests that the photoabsorption features are truly narrow in width and it is not possible to resolve them

Also the importance of the effect of saturation of photoabsorption measurements is clearly illustrated in figure 3-11 where the data points on the experimentally extracted photoabsorption cross section deviate from a linear relationship with increasing residual gas pressure This is due to a number of effects such as stray light, presence of multi-order light, detector spatial resolution and detector dynamic range

3 4   Dual laser plasma barium 5p photoabsorption measurements

In order to characterise the suitability of the system for photoabsorption studies using the dual laser plasma technique, measurements on the 5p photoabsorption spectra of a barium plasma were made. This was the first time that the dual laser plasma technique for photoabsorption was performed on the Acton™ 1 meter normal incidence spectrometer at the DCU laboratory. The experimental arrangement is illustrated in figure 3-13. All measurements were made using the Galileo™ CEMA / EG&G™ PDA detector

The lasers used to generate the continuum emitting plasma and absorbing plasma were both Q - switched Nd YAG laser's (15 – 25 ns FWHM @ 1064 nm). The laser used to generate the continuum plasma had an energy of ~ 690 mJ (Spectron™ SL803) while that used to generate the absorbing plasma had an energy of ~ 160 mJ (Spectron™ SL404). The output of the SL404 Nd YAG laser was focused to a spot size of ~ 500 μm with a plano convex lens of focal length 105 mm and diameter 22 mm in order to generate an absorbing plume of principally neutral barium. The output of the SL803 Nd YAG laser was tightly focused with a plano convex spherical lens of focal length 100 mm and 22 mm in diameter to a spot size of ~ 150 μm. The burn pattern for the SL803 laser at the lens position was observed to be symmetrical (10 mm diameter) while the burn pattern for the SL404 laser at the target lens position was very elongated ($3 * 10 \text{ mm}^2$) due to poor internal alignment of the laser. Subsequent investigation showed damage to an output coupler in the SL404 to be responsible for poor beam quality

Figure 3-13   Schematic of experimental arrangement used in DLP experiments
Dimensions between optical components are shown in mm. Lens assembly not shown
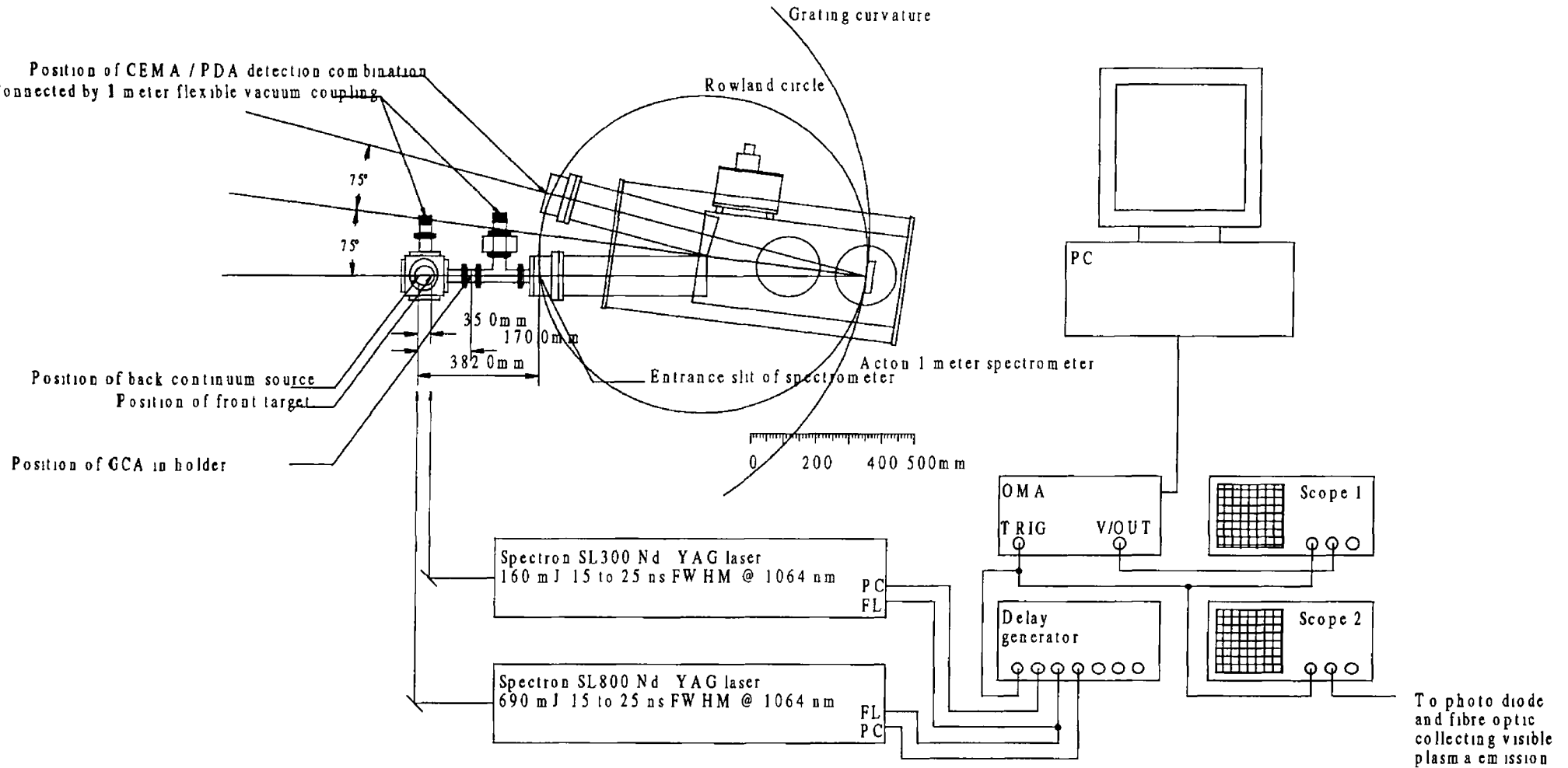
Barium is an alkaline earth metal having an atomic weight of 56 It has a silvery-white appearance and oxidises readily in air The VUV photoabsorption spectra of atomic and ionic barium have been investigated in work done by Kent *et al* [1987] and also by Lucatorto and McIlrath [1980] amongst others It has been found that the 5p photoabsorption spectra of barium and its ions display a rich variety of lines Some important physical processes have been first seen in barium e g double ionisation anomaly [Brehm and Hofler, 1975] It also is important for the reason that the compound YBCO ($YBa_2Cu_3O_{7\,\delta}$) is actively being investigated as a high temperature super conducting material It is also worth noting that the laser plasma ablation technique has proved itself ideal in producing thin films of such compounds

Barium possesses a closed outermost sub shell and therefore its photoabsorption spectrum should be relatively simple Instead of what should be a simple Rydberg series converging on just two series limits according to the one electron excitation scheme, $5p^6 6s^2\ ^1S_0 \rightarrow 5p^5 6s^2\ ^2P_{1/2\,3/2}$ ns, nd the 5p spectrum of Ba I is found to consist of 14 series converging on 12 limits [Lucatorto and McIlrath, 1980], [Kent *et al*, 1987] The 5p photoabsorption spectrum of atomic barium is therefore one of the richest inner shell excitation systems The large number of extra series encountered in the barium spectrum can be pictured as a 'shattering' of the $6s^2$ sub shell by 5p excitation [Connerade, 1978] In effect $6s^2$, 5d6s and $5d^2$ configurations lie close in energy and exhibit significant configuration mixing allowing photoexcitation to $5p^5 6s^2 nl$, $5p^5 6s5dnl$ and $5p^5 5d^2 nl$ series from the $5p^6 6s^2$ (^1S) ground state The corresponding Ba^+ ion-core yields the 12 observed limits [Rose *et al*, 1978]
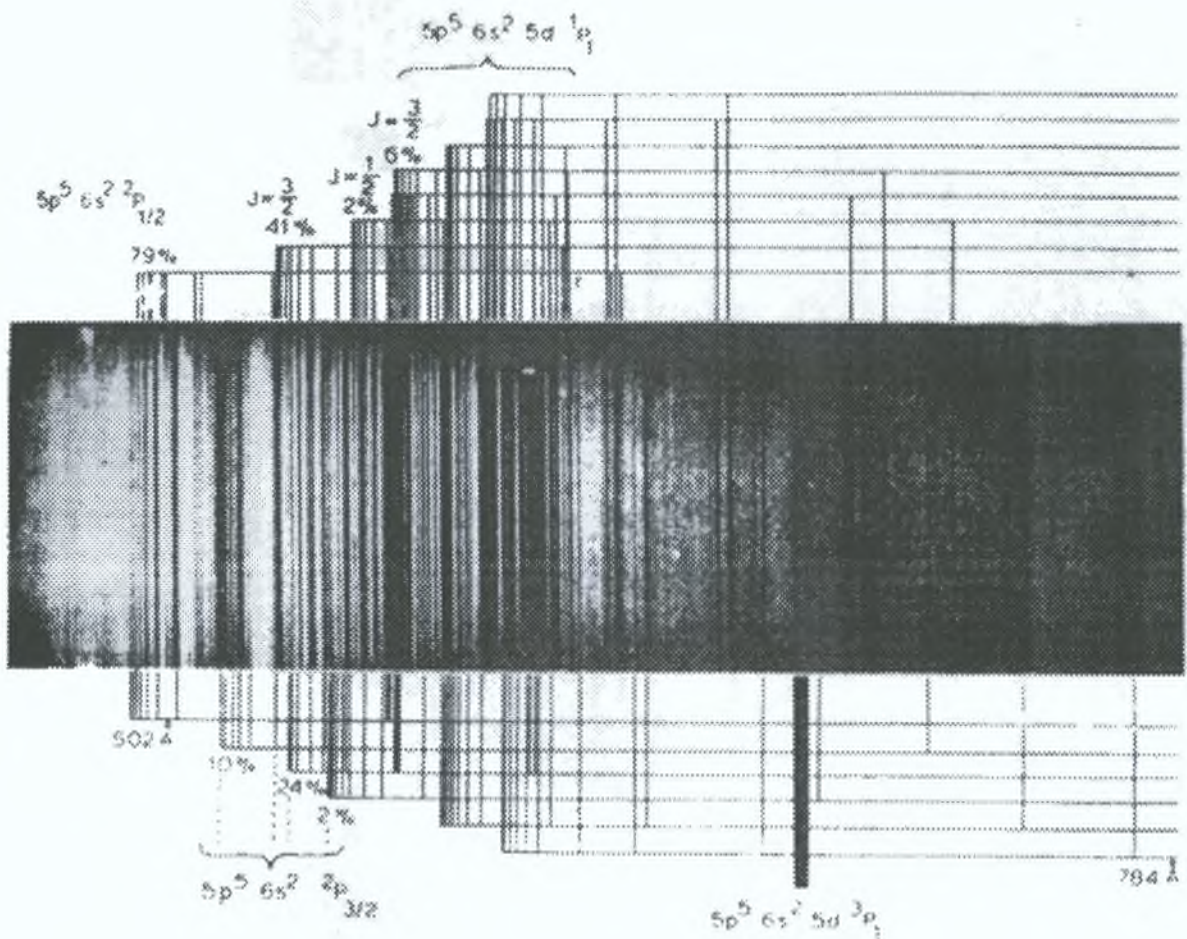
Figure 3-14.   The 5p sub shell photoabsorption spectrum of Ba I showing how the ordering into Rydberg series is accomplished [Rose et al,1978]. The range extends from approximately 48 to 79 nm.

In the experiments discussed here, the barium plasma producing laser was defocused and the barium plasma itself was positioned a distance from the optical axis in order to optimize the barium atomic population in the absorbing plasma plume. The wavelength range studied was between 48 and 68 nm and allowed for all of the series limits of the 5p photoabsorption spectrum to be observed within one wavelength setting of the grating.

It was found that the front plasma emission, $I_{front\,plasma}$, was of sufficient intensity that it needed to be subtracted from the absorption spectrum signal before the relative photoabsorption cross-sections could be derived. In order to reduce the collection of front plasma emission the barium planar target was rotated to make an angle of ~ 5 ° with the optic axis of the spectrometer. In this way it was possible to

partially occlude the hot (VUV emitting) core of the barium plasma. The absorption coefficient is given in general by the expression,

$$k(\lambda) = \exp\left(\frac{I_0(\lambda) - I_{s0}(\lambda)}{I(\lambda) - I_{front-plasma}(\lambda) - I_s(\lambda)}\right) \qquad [\text{ E.3.4.A. }]$$

where the spectrum of the background continuum source, $I_0(\lambda)$, and the absorption spectrum, $I(\lambda)$, are corrected by the contributions from stray light, $I_{s0}(\lambda)$, during the measurement of I_0, $I_s(\lambda)$ from both plasmas during the measurement of $I(\lambda)$ and for the emission, $I_{front-plasma}(\lambda)$, from the absorbing plasma. The contribution of stray light, presence of higher order light and light entering the spectrometer without passing through the absorbing plasma all result in an additional 'baseline' signal on the detector video out signal. Hence, features in photoabsorption measurements will saturate before complete absorption. Stray light was not calculated but assumed to be negligible as the spectrometer had a number of baffles and the illuminated width of the grating was significantly smaller than the actual width due to the aperture defined by the GCA. Due to the poor grating efficiency below ~ 30 nm, no significant second order light is expected in the 30 to 60 nm spectral range of interest here.

A small rectangular section of barium (approximately 4(w) * 6(h) * 10(l) mm) was cut from the cast ingot which was of spectroscopic purity. The barium sample was clamped in place by a small c-shaped machined holder. Barium oxidises readily when exposed to air thus forming a relatively loose barium oxide layer. This oxide layer was cleaned while under vacuum by firing a few loosely focussed laser pulses onto the barium target. The distance from the continuum plasma and the absorbing plasma was approximately 32 mm along the optic axis.

The CEMA intensifier was operated with a gap voltage significantly less than the recommended 4 kV so that the wavelength resolution achievable was degraded somewhat. This was unavoidable as higher voltages (greater than 2.5 kV) led to arcing across the gap. Although the resulting theoretical electron spot size on the phosphor within the CEMA intensifier (given by equation 2-10) is a factor of 12 higher than with normal operating gap potentials, it is found in practice that this is

not the limiting factor in spatial resolution of such a detector arrangement Emission spectra of polyethylene and other line-dominated plasmas displayed no significant linewidth increases when using the lower gap potential (perhaps one pixel or so)

The synchronization of the Q-switched lasers was achieved by the use of a multi-channel Standford Research™ time delay generator This triggered both the flash lamps and Pockels cells in the two Nd YAG lasers with a variable time delay between the Pockels cell triggers for the leading absorbing plasma generating laser and that of the following continuum emitting plasma generating laser The TTL level signals from the delay generator were converted to 15 V level signals suitable for the triggering of the lasers using step-up transistor circuits The master trigger was provided by the OMA controller and also was used for triggering storage oscilloscopes used to monitor the laser pulse profiles, inter laser pulse delays (with the aid of a optical fiber and fast photodiode, e g BPX-65) and also the OMA video signal (see figure 3-13)

A pair of 45 ° Nd YAG mirrors located on optical rails were used to direct the two Nd YAG laser beams onto focussing lenses located outside the target chamber The collected samarium plasma emission was optimized by maximizing the observed average counts of the entire PDA detector array while adjusting the target position holder (translation across the optic axis, x) and focusing lens assembly (three degrees of freedom, x, y and z) It can be seen from figure 3-10 that the samarium continuum has a reproducibility of ~ 2 % using a Nd YAG SL803 laser over the restricted wavelength range 48 to 68 nm used in most of the barium photoabsorption experiments
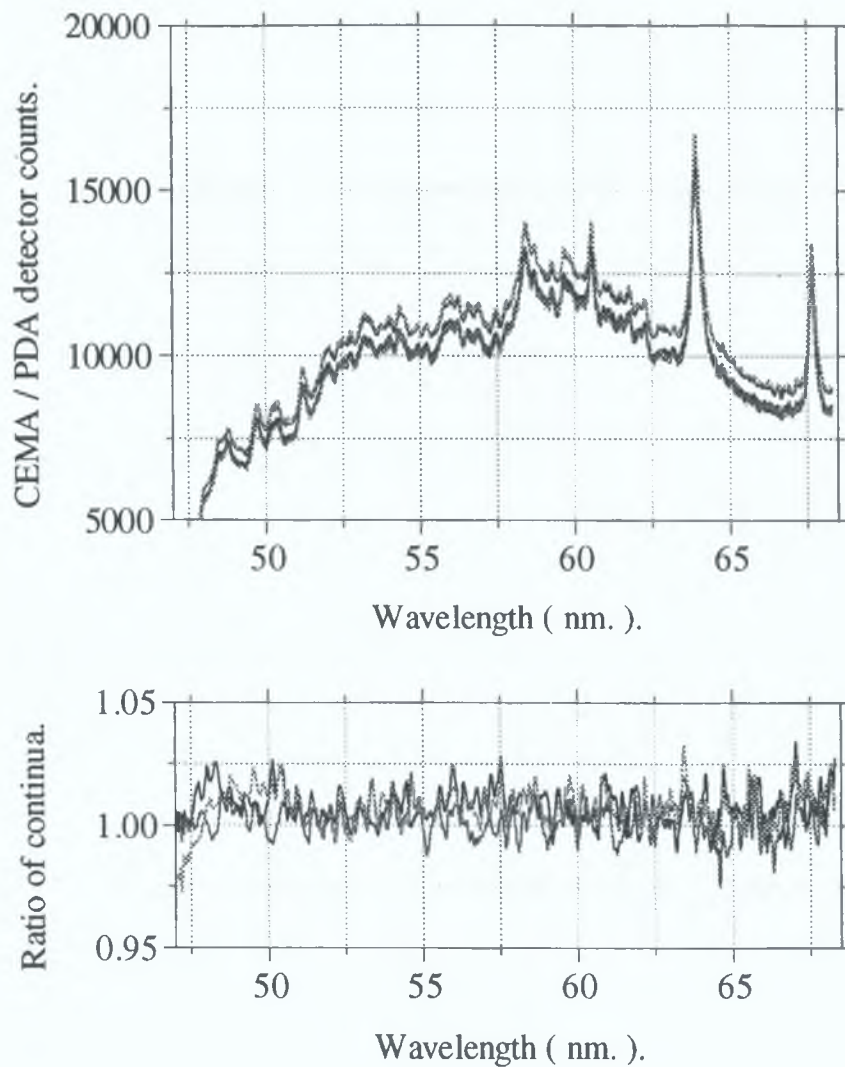
Figure 3-15.   (upper plot) Continuum dominated emission from a samarium plasma produced by a Spectron™ SL803 Nd : YAG laser (~ 690 mJ in 15 – 25 ns FWHM @ 1064 nm) showing good reproducibility and lack of discrete features and also (lower plot) ratio of pairs of I_0 spectra indicating good reproducibility of features.

The barium target was moved inwards towards the optic axis of the spectrometer until it began to occlude the continuum emission which was accepted by the spectrometer. This point was taken to correspond to zero deviation of the target surface from the optic axis of the system. It was then pulled back by ~ 0.5 mm (referred to as Δx) and a series of photoabsorption spectra were taken for various time delays.

In figure 3-16 (a) the continuum emission from a samarium plasma is displayed in the region of interest for the barium 5p photoabsorption spectrum The continuum is essentially 'line free' with the two strongest line features most likely to arise from the lower ion stages of the samarium plasma The absorption is displayed in figure 3-16 (b) for an inter laser time of 104 ns and $\Delta x = 0\ 5$ mm with the absorption plasma producing laser de-focussed by 5 mm In figure 3-16 (c) the front plasma emission is displayed with no target rotation A dark spectrum was not subtracted from this particular data set and so the relatively large offset from zero counts is not all continuum emission from the barium front plasma alone Some of the strong emission lines display self absorption and there is also signs of absorption of the continuum emission generated by the barium plasma
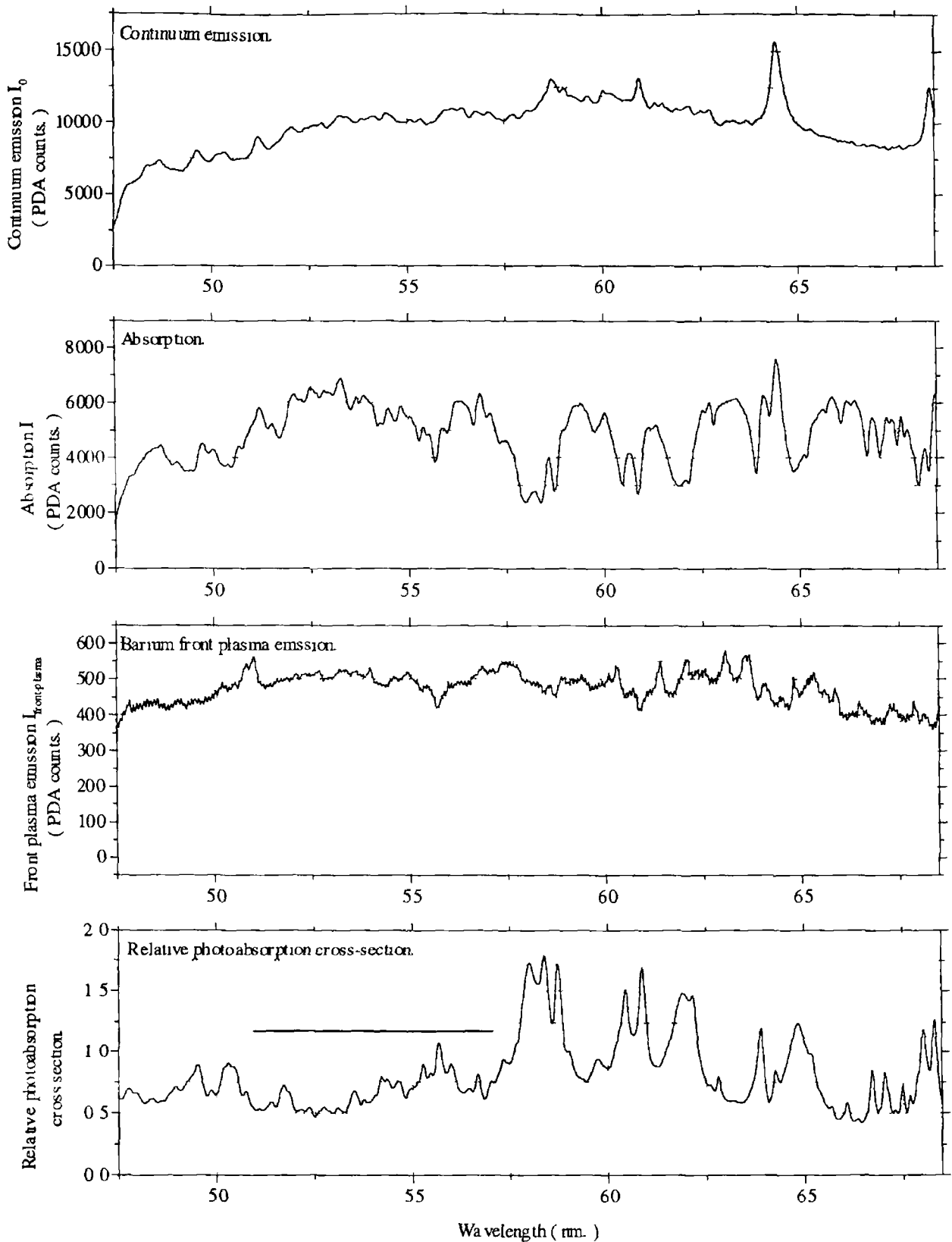
Figure 3-16 (a) *Continuum dominated emission from a samarium plasma in the region of interest 48 to 68 nm, (b) barium absorption spectrum (Δt = 104 ns and Δx = 0 5 mm), (c) barium front plasma emission only and (d) relative photoabsorption cross section*

The relative photoabsorption of barium is displayed in figure 3-16 (d) for the experimental conditions already given above. The spectrum is characteristic of that produced by the absorption of predominantly neutral barium. However comparing the spectrum with that taken by Lucatorto et al, 1980 it is evident that some Ba^+ and Ba^{++} is also present. The relatively strong photoabsorption feature (within the region between 51 nm to 57 in figure 3-10 (c)) at 55 548 nm corresponds to the Ba^{2+} resonance transition of $5p^6$ $^1S \rightarrow 5p^5 5d^1$ $^2P_{1/2}$
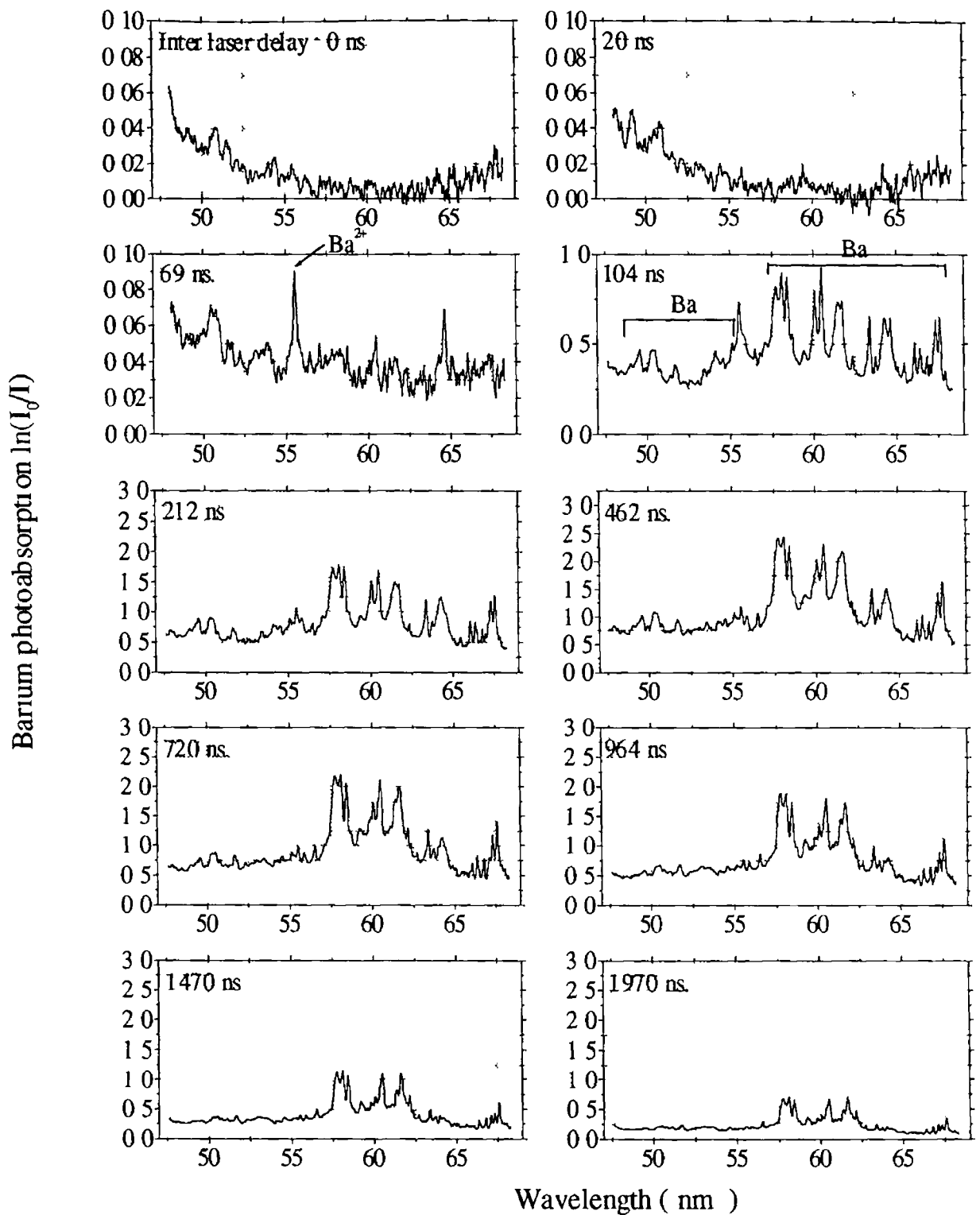
Figure 3-17   Photoabsorption of predominantly neutral barium in the wavelength range 48 to 68 nm for various different inter laser time delays The barium sample was positioned 0 5 mm back from the start of cut-off (see text) The continuum plasma was produced by a Q-switched Nd YAG (~ 690 mJ, 15 – 25 ns FWHM @ 1064 nm) focused onto a samarium target The barium absorbing plasma was produced by a Q-switched Nd YAG (~ 160 mJ, ~ 15 ns FWHM @ 1064 nm)

510Å   525Å   550Å   565Å

Ba

Ba⁻

Ba'⁺

He   515 62   522.21   537.03   555 48
      He   He   He   Ba'' ²P₁₂ 5d|3/2 ,
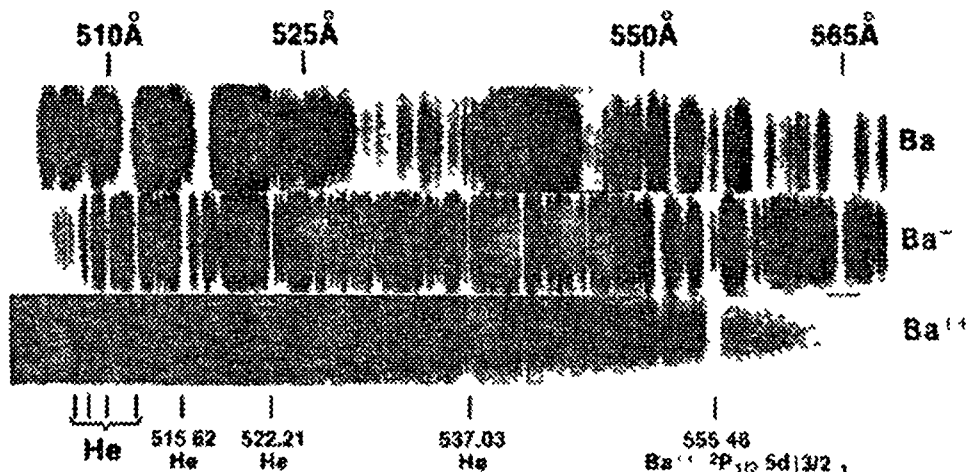
Figure 3-18   *Barium photoabsorption spectra in the range 50 to 57 nm as recorded by Lucatorto and McIlrath [1980] Upper spectrum Ba, middle spectrum, Ba⁺, lower spectrum Ba²⁺ Densities and temperatures are the same for all spectra Indicated wavelengths are in Angstroms*

In figure 3-17 the time resolved spectra show the absorption of predominantly neutral barium around the limits of the 5p photoabsorption The region around 56 5 nm displays the most intense relative photoabsorption cross-sections which compares to that result of Lucatorto and McIlrath [1980] The general features of the absorption spectrum agree with the full absorption spectrum as taken by Connerade *et al* [1978] The reduced resolution of the Acton™ VM-521 spectrometer instrument makes it difficult to compare the results directly to those of Kent *et al* [1987] At inter laser delays of ~ 70 ns the dominant ion stage is observed to be Ba^{2+}, $5p^6 \, {}^1S \rightarrow 5p^5 \, {}^2P_{1/2}5d[3/2]_1$, at 55 548 nm with few other absorption features present At this early stage in the plasma formation the high temperature and density facilitates the production of Ba^{2+}
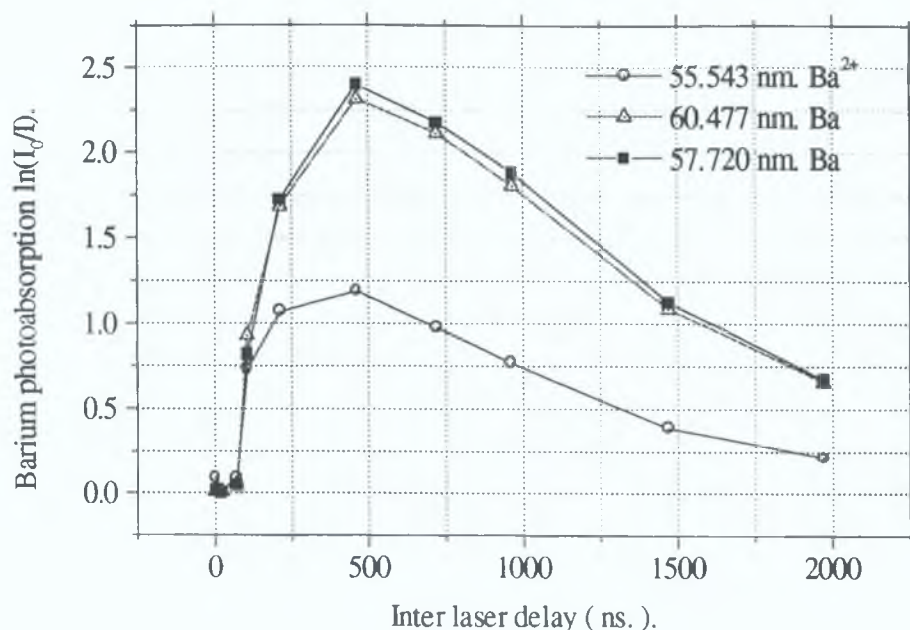
*Figure 3-19.   Graph of relative absorption for the resonance transitions of Ba^{2+} :
5p^6 ^{1}S → 5p^{5}5d^1 ^{2}P$_{1/2}$ at 55.55 nm and neutral Ba at 57.72 and 60.48 nm versus inter
laser delay.*

In figure 3-19 the relative photoabsorption cross-section is plotted against
inter laser delay for identified transitions. The relative photoabsorption cross-section
is seen to peak at ~ 500 ns for nearly all the spectral lines. The temporal resolution is
determined by the duration of the continuum emitting plasma which is approximately
~ 200 ns in the normal incidence VUV region with the Spectron™ Nd : YAG laser
used in the experiment [Rydén, 1993].

The results presented in this section serve to demonstrate the system's ability
to perform relative photoabsorption cross section measurements on a plasma plume
using the DLP technique. Use of a secondary slit between the absorbing plasma and
continuum emitting plasma would limit the extent of the source emission at the
absorbing plasma position as collected by the spectrometer thereby improving spatial
resolution. The increased spatial resolution would further improve the selection of an
individual ion stage and also help to discriminate against front plasma emission
which is predominantly from the hotter core. The experimental arrangement
facilitates temporal photoabsorption measurements to be performed on the secondary

plasma plume It must be pointed out that the duration of continuum emission from rare earth plasmas increases with wavelength and therefore the temporal resolution possible in normal incidence VUV experiments using the above arrangement are limited to approximately 200 ns [Rydén, 1993] Use of a gated MCP would of course reduce this to the chosen gate width (typically $\leq$ 10 ns) and would also serve to reject a substantial amount of front plasma emission

3.5 $YBa_2Cu_3O_{7-\delta}$ emission.

For a number of years, $YBa_2Cu_3O_{7-\delta}$ (YBCO) as a high T_C superconductor
has led interest in laser deposition techniques for the generation thin films of such
materials. The ion distribution, density and temperature as well as expansion velocity
of the plume and presence of ambient oxygen atmosphere are all thought to
determine the resulting thin film properties [Mehlman *et al*, 1993]. Several
techniques including optical emission spectroscopy [Fried et al, 1991 and Dyer,
1990], absorption spectroscopy [Geohegan and Mashburn, 1989], laser induced
fluorescence [Fried et al, 1994], direct imaging [Wazzan et al, 1996 and Geohegan,
1992] and mass spectroscopy [Wiedeman and Helvajian, 1991] have been used to
study the plasma parameters following laser ablation.

The current section is concerned with presenting spatially resolved VUV
emission spectra from a laser produced YBCO plasma plume. Spatial resolution was
achieved by placing a slit of width 525 μm, aligned with the spectrometer slit some
47 mm from the plasma source and 335 mm from the entrance slit (see figure 3-15).
As an aid to identifying spectral features in the recorded YBCO spectra, the emission
spectra of some of the constituent elements in the compound, namely barium (Ba, Z
= 56), copper (Cu, Z = 29) and oxygen (in the form of beryllium oxide, BeO)
were also recorded. Yttrium was unavailable at the time of the experiment. Emission
spectra were recorded using a Spectron™ SL404 Nd : YAG laser (~ 163 mJ 1064
nm, 15 – 25 ns FWHM) focused to an estimated spot size of 3 mm diameter
resulting in an on target irradiance of ~ $1.2 * 10^8$ W cm^{-2} or a fluence of ~ 2.3 J cm^{-2}.
The number of laser shots integrated to produce each spectrum record was ten.

The experimental arrangement was similar to that illustrated in figure 3-1
with the continuum emitting target being replaced by a sample holder which allowed
for the attachment of the YBCO [supplied by TCD], barium, and copper planar
targets as well as carbon and aluminium. For recording oxygen plasma spectra a
cylindrical beryllium oxide target was used which also had the secondary purpose of
calibrating the spectrometer. Although the laser ablation and deposition of YBCO
compounds is usually done in an oxygen rich atmosphere (100 to 200 mTorr), the

following results are concerned with the emission of a plasma expanding into vacuum

The YBCO spectrum displays a continuum dominated structure with a shape partly determined by the grating efficiency profile The observed emission lines are mostly oxygen up to the fourth ion stage with a small number of the discrete features from barium and copper present also The intense emission from barium is thought to make up most of the underlying continuum signal Although not studied here, the high atomic number target yttrium (Y, Z = 39) is expected to produce predominantly continuum emission The copper emission displays a low underlying continuum with low average counts with three visible broad features centred at approximately 68, 75 and 85 nm A small number of oxygen emission lines are also evident in the copper emission spectrum
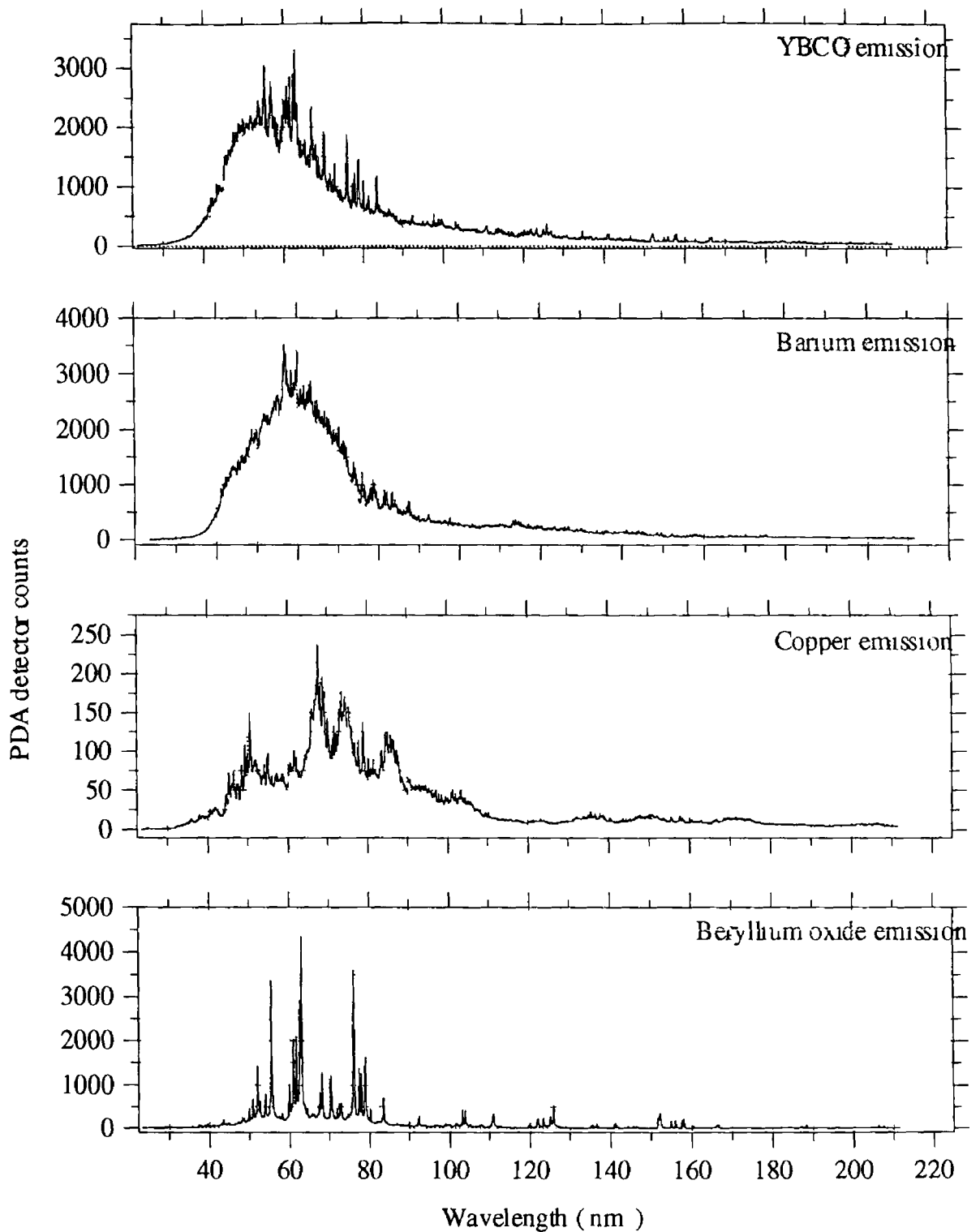
Figure 3-20   *Emission spectra of YBCO sample taken with Acton™ 1 meter*
normal incidence spectrometer in the range 20 to 220 nm without the use of a spatial
resolving pre slit A Nd   YAG laser ~ 169 mJ, 15 to 25 ns @ 1064 nm was used with
an on target irradiance of ~ 1 2 * 10⁸ W cm² In addition, shown underneath are
individual element spectra of barium, copper and beryllium oxide taken at a tight
focus condition.

With no spatially resolving slit the acceptance angle of the spectrometer is such that almost all the emission from the plasma is collected With the introduction of the slit it was possible to isolate a region of the plasma plume with dimensions of ~ 580 μm in the horizontal plane No additional spatial resolution in the vertical plane is obtained Figure 3-15 shows the arrangement specific to this experiment
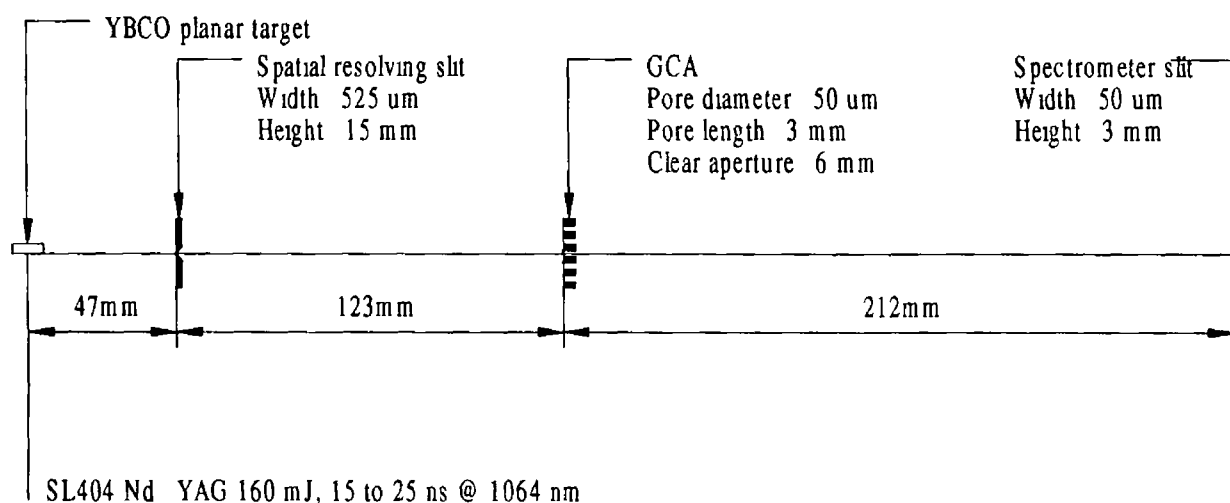
Figure 3-21   Schematic of positions of the source, spatial resolving slit, GCA and spectrometer slit used in the recording of spatially resolved emission from a laser produced $YBa_3Cu_5O_7$ plasma

In order to characterize the spatial resolution of the system with the introduction of the pre-slit the YBCO target was temporarily replaced with a cylindrical tungsten target The tungsten target was irradiated by ~ 690 mJ Nd YAG using a tight focus at ~ 45 ° and the resulting continuum emitting plasma was aligned to the optical axis of the spectrometer by maximizing the average counts at a central wavelength of ~ 39 nm The spatially resolving slit was now introduced by simple rotation of the slit holder and emission spectra were recorded for various positions of the spatial resolving slit The position of this slit was set at the location which yielded optimum flux and remained at this optimized position for the remainder of the experiment The extent of the emission from the tungsten plasma was recorded by moving the target relative to the fixed slit in 0 5 mm increments and recording the average counts at each position Considering the geometry of the arrangement a maximum dimension of approximately 1 45 mm in diameter is placed on the

tungsten plasma emission at a wavelength of ~ 39 nm with the portion emitting the

most of this emission being somewhat smaller than this dimension
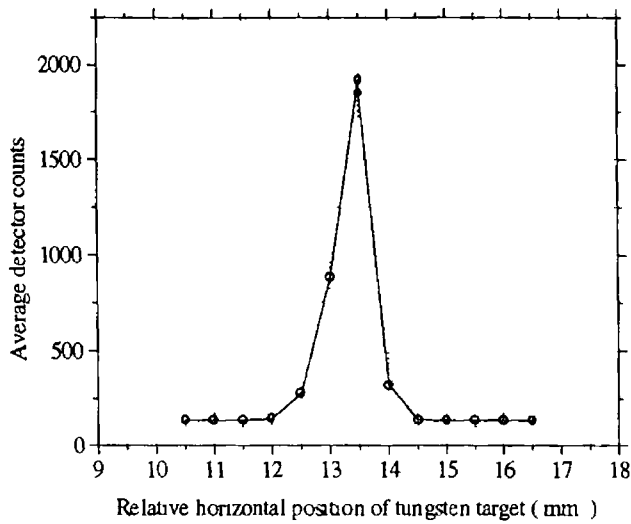
Figure 3-22   Average counts of tungsten emission plasma at a central wavelength of 38 nm versus relative horizontal position of tungsten target with spatial resolving slit 525 µm in width at a distance of 47 mm from tungsten source

The tungsten target was now replaced with the planar YBCO sample and the position of the plasma emission was optimized (both vertical and horizontal directions) so that maximum average counts were obtained By moving the YBCO target horizontally the emission from a spatially resolved chord ~ 580 µm was recorded at various distances from the target surface (see figure 3-16) The transition from continuum dominated emission close to the target surface to line dominated emission at the cooler regions further from the target surface is clearly seen in figure 3-17

Distance from target
surface 2 5 mm

Distance from target
surface 3 5 mm

PDA detector counts

AlO
110

110
AlO
AlO
AlO

OI
110
OI
110
IIIO
OIIIO
OIIIO
OIIIO
OIIIO

IIIO
OI
OI
AlO
OV
OIV
OV
AlO
OIV
OIV

OIIIO
OIIIO

OI

Distance from target
surface 4 5 mm

Distance from target
surface 5 5 mm

Wavelength (nm)

Figure 3-23   Spatially resolved YBCO emission spectra at various distances from target
surface (2 5, 3 5, 4 5 and 5 5 mm)   The spatially resolving slit (of ~ 525 μm in width) was
positioned a distance 47 mm from the source   The GCA to source distance was 170 mm and
the spectrometer slit to source distance was 382 mm

The observed spectra at distances of $\geq 3\,5$ mm from the target are seen to be dommated by oxygen lines, OII, OIII, OIV and OV, superimposed on a weak continuum with the most intense being OIV A limit of $5\,5$ mm was placed by the target holder movement The integration time for the PDA detector was set at 30 ms and therefore the spectra are the integrated emission within this time Some of the more intense lines show signs of self absorption resulting from the optically thick plasma plume at distances close to the YBCO target

Chapter 4   Further system development.

The present chapter discusses the design, construction and part characterisation of a vacuum-optical beam line which serves to focus the plasma plume onto the entrance slit The development has the following benefits, (1) One can study emission from various parts of the plasma plume by moving the plasma image across the spectrometer entrance slit, (2) in conjunction with an iris of known diameter, a section of the absorbing plasma plume with known conical geometry may be selected in DLP experiments and (3) an increased throughput is obtained over the arrangement used in experiments to date Although no spectral data could be obtained using this set-up because the concave mirror available had a surface coating which resulted in an extremely poor reflectivity in the normal incidence VUV range, work to date is included simply to highlight the advantages of such an addition Estimates of the increase in throughput and spatial resolution are presented using both simple geometric arguments as well as Monte Carlo simulations using the software package 'Shadow' developed by Lea et al [1986] at the Center for X-ray Optics, Wisconsin University

4 1   Introduction

Spectroscopic studies of laser produced plasmas with some form of spatial resolution and / or imaging qualities are important as they can reveal the true nature of laser generated plasmas, i e dynamic systems with parameters which vary with space and time (e g electron and ion density and temperature gradients) Laser generated plasmas generally have symmetry about the axis perpendicular to the target plane and so simple space resolving pre-slits can isolate in a limited section of the plasma plume to be spectroscopically studied Furthermore, if an entrance slit with limited vertical extent (i e pin hole) is used and a two dimensional array detector plane is positioned at the vertical focus, the resulting system can achieve monochromatic spatial imaging of the emission source with a one-to-one correspondence between points on the source plane and points on the detection plane As the system works effectively as a pm hole camera, spatial imaging with magnification of the source is possible [Koog et al, 1996 and Richards et al, 1980]

4.2   Addition of VUV focusing optic.

The Acton™ VM 521 spectrometer is inherently a large f-number instrument (approximately f/10 in the horizontal plane when equipped with 96 * 56 mm grating) and so without any apertures or slits the instrument is unable to discriminate between emission from various regions of a plasma The spectrometer effectively integrates all of the available VUV emission from the plasma which falls within the large acceptance angle of the instrument

Although this experimental arrangement results in a relatively high throughput of flux for extended sources, it nevertheless means that experimental studies are limited to those that do not require spatial information With the addition of the GCA the situation is somewhat changed and the acceptance angle of the combined spectrometer system is considerably reduced to an effectively f/60 instrument As the plasma plume is of small extent and is positioned a distance of ~ 382 mm from the entrance slit of the spectrometer (a consequence of the need for a GCA and support vacuum components) the combined system does not allow for space resolved studies of the plasma plume without the use of a secondary slit

Spatial resolution can be important for photoabsorption studies as the dominant ion stage can be selected somewhat by passing the continuum radiation through a specific portion of the plume and onto the entrance slit of a spectrometer The use of a slit allows for the collection of light from a vertical chord of the plasma plume Usually slits reduce the amount of light coupled into an optical system considerably and therefore the signal to noise ratio of the recorded spectrum suffers Hence it is important that the system be as close to aperture matched as possible

Using a detector with smaller pixel dimensions would increase the resolution capability of the instrument but the reduced entrance slit width necessary may reduce the spectral signal to a level where un-intensified detectors may be insufficient to provide an adequate dynamic range Changing the grating to one which has a higher groove density

108

(1800 or 2400 lines mm ^{1}) would also increase the wavelength resolution achievable but at the expense of the extent of the available spectral range which is determined by the maximum mechanical movement of the grating

Considering the fact that only a small region of the maximum spectral range is observable for reasons such as choice of the blazed wavelength, order sorting problems and availability of a suitable backlight continuum the replacement of the grating with one which has a higher groove density may be the most appropriate way of increasing the wavelength resolution of the instrument

4.3   Vacuum-optical design

In designing the vacuum system to couple to the existing spectrometer instrument the main requirements are for a UHV mirror chamber with a mirror holder enabling angle and focusing adjustments to be made external to the vacuum system A near normal incidence arrangement for the additional optic was chosen to reduce the effect of aberrations The entrance and exit arms of the mirror chamber were therefore set at 15 ° between them A concave focusing optic with focal length of 500 mm and diameter 50 8 mm with an UV enhanced aluminum coating (i e aluminum with MgF_2) was initially used It was thought to be feasible to use such a coating in the VUV ($\lambda \geq 30$ nm) even though the coating is more suited to longer wavelength UV radiation and no reflectivity measurements below $\lambda = 200$ nm were available A schematic diagram showing the main components of the vacuum-optical beam line is displayed in figure 4-1

Entrance slit of spectrometer
Height 3mm
Width 50um typically

218mm

1000mm

88 5mm

35mm

Spherical concave mirror
Focal length 500mm
F/Number 20
Diameter 50 8mm
Coating Aluminium + MgF2 / Iridium

Figure 4-1   Schematic of system arrangement with attached focusing optic and vacuum system. Dimensions between optic elements are shown in mm.
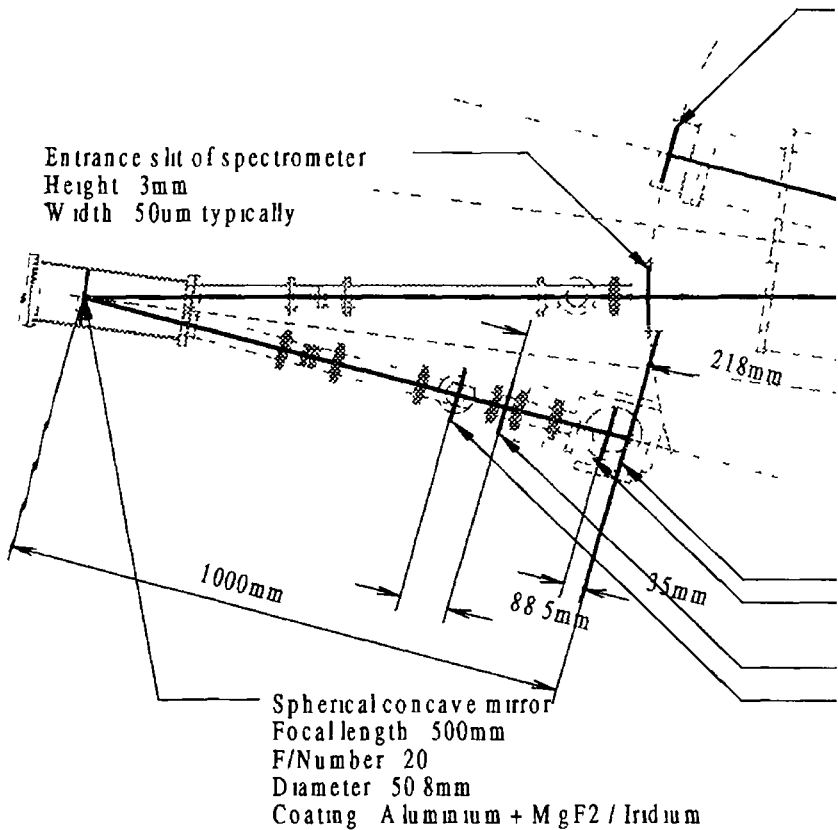
Exit of spectrometer
MCP and PDA detector
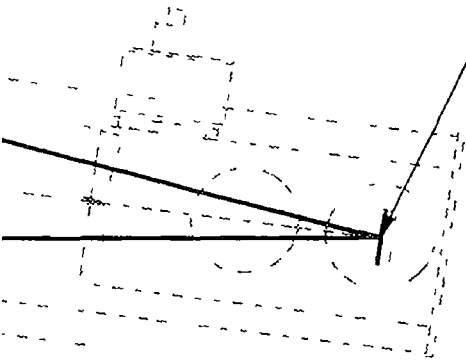
Spectrometer's concave grating
Grooves / mm   1200
Concave radius 995 4mm
Coating   Iridium
Blaze angle   2 75
Blaze wavelength   80nm (First order)
Ruled width   96mm
Ruled height   56mm

Backlight plasma
Target plasma

Glass capillary array
Optional variable aperature

Ideally, the grating should be illuminated to both it's full vertical (56 mm in the direction of the rulings) and horizontal extent (96 mm) without overfilling which would cause stray light problems With the small extent of the laser produced plasma light source and the necessary positioning of such a source a distance from the spectrometer entrance slit some form of aperture matching optics are needed for this criterion to be achieved The further the source is positioned away from the slit, the smaller the width of the grating that is illuminated The throughput also decreases significantly and is proportional to $1/r^2$ where r is the distance from the source to spectrometer entrance slit Although the resolution of the spectrometer is theoretically linearly proportional to the illuminated width, it is found in practice that other factors can effect the limiting resolution such as optical aberrations, entrance slit width and detector spatial resolution Reduction of the spectrometer slit below a certain value in practice gave no appreciable increase in resolution achievable although the throughput was severely decreased An entrance slit width of 50 μm when imaged in the dispersion plane is at best ~ 2 pixels (FWHM) in the case of the back thinned CCD (25 μm pixel dimension) Therefore considering the fact that an array detector such as this needs greater than 2 pixels to provide an accurate representation of the spectral line the observation can be justified

With the addition of the focusing mirror, the plasma light can be focused onto the entrance slit of the spectrometer thereby increasing the throughput of the complete spectrometer system compared to that arrangement used in experiments to date Also, it is possible to study emission from various parts of the plasma plume by moving the plasma image across the spectrometer's entrance slit

Even though the very process of achieving a spatially resolved experimental arrangement inherently reduces the aperture matching of the instrument, it is important that the maximum flux from this selected section of the light source be collected by the spectrometer The GCA, with its intrinsically small acceptance angle limits the extent of the grating which can be illuminated when using a focusing optic On the other hand, in the direct-coupled system the small size of the emitting plasma is the limiting factor Although the reflectivity of most materials

111

(non multi-layer) in the extreme VUV region is poor, the reduced reflectivity is compensated by the fact that the collected VUV radiation is focused onto the spectrometer slit and so even though the flux is reduced the amount of flux entering the spectrometer is increased

However, after the experiment it became apparent that the available mirror did not possess good reflectivity in the 30 to 80 nm spectral range of the grating and was not sufficient to improve the light gathering ability of the combined system over the direct coupled system In view of this, an iridium-coated mirror with the same dimensions and focal length is presently on order and this will directly replace the existing mirror

Two flexible couplings (length 94 5 ± 6 mm) were used at both entrance and exit arms of the mirror chamber (see figure 4-1) These had the primary purpose of allowing for slight misalignments in the vacuum flanges and also served to allow both vacuum arms to be assembled without moving the mirror chamber, target chamber or spectrometer from their aligned positions

A manipulator which permits alignment of the mirror external to the vacuum system was designed and is illustrated in figure 4-2 It consists of two parts, an aluminum flange which connects to a 100CF flange suitable for connection to the mirror chamber rear port (part A) and a stainless steel plate with three Wilson type seals to allow the three 6 mm diameter silver steel bars which could rotate as well as move in and out (part B) One of these bars is rigidly attached to the gimbal optical mount while the other two connect by the use of small chucks to the fine pitch alignment screws of the mirror mount Therefore rotation of the bars external to the vacuum system allows for angular deflections of the attached mirror in two orthogonal planes while translation of the third bar when rigidly fixed to the other bars moved the whole mirror assembly towards or away from the plasma source and entrance slit The aluminum flange had a groove on both sides which facilitated a 4 5 mm o-ring The 100CF flange makes use of a copper gasket seal to provide a vacuum connection to the mirror chamber The stainless steel plate is not rigidly connected to the aluminum flange and is able to slide on the o-ring seal thus allowing the mirror to be moved Horizontal and / or vertical

112

(x, y -axis) movement of the mirror assembly is facilitated by 4 drive screws placed at 90 ° to each other
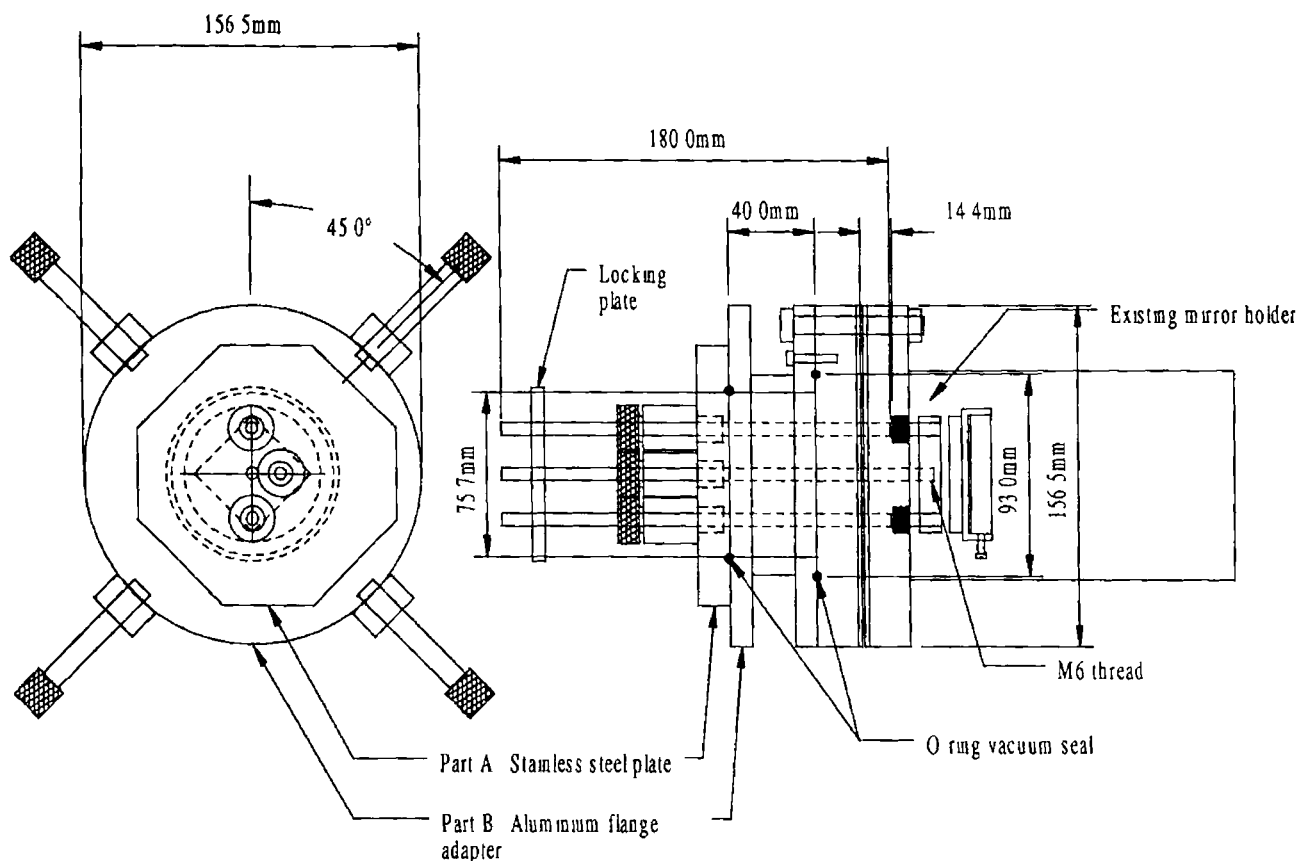
Figure 4-2   Schematic of mirror manipulator with focusing (z-axis), angle and optic axis (x, y -axis) alignment adjustments   The mirror holder facilitates mirrors with 50 8 mm diameter

4.4   Basic flux calculations

Some preliminary calculations were performed in order to estimate the increase in flux with the additional focusing optic incorporated into the system It has been shown that the spectral radiance emitted from laser produced plasma using Q-switched lasers of ~ 1 J per pulse is approximately $2 * 10^5$ J cm^{-2} sr^{-1} s^{-1} nm^{-1} @ 120 nm emitting into 4π steradians [Carroll et al, 1983] This in turn corresponds to a flux of 1 21 $* 10^{23}$ photons cm^{-2} sr^{-1} s^{-1} nm^{-1} The normal incidence VUV duration of a plasma is generally accepted to be a longer than the XUV pulse which lasts for approximately the same duration as the laser pulse Work carried out by Rydén

[1993] on the Acton™ VM-521 spectrometer with photomultiplier based detector indicated that continuum emission from tantalum plasmas produced by a Nd YAG laser (~ 1 J, 15 to 25 ns duration FWHM @ 1064 nm) had a time duration of ~ 200 ns (FWHM) in the long wavelength region ($\lambda \geq 200$ nm) of the normal incidence VUV spectrometer Hence there are ~ 2 42 * 10^{16} photons cm^2 sr^1 nm^1 in a 200 ns (FWHM) VUV pulse Assuming the source has an effective diameter of ~ 1 45 mm at this wavelength one obtains ~ 4 * 10^{14} photons sr^1 nm^1

4.4 1   Original system

The effective acceptance angle of the GCA (defined by the l/d ratio 1/60 radians) is ~ 2/60 radians The GCA has an effective optical transmission of ~ 30 %, principally due to the loss in flux by occlusion of the rays The entrance slit of the spectrometer is located 212 mm from the exit face of the GCA Taking the plasma source to be of point like extent and located 170 mm from the GCA the source footprint on the spectrometer's slit will be ~ 13 mm in diameter Therefore, the flux entering the spectrometer through a slit of 50 µm in width and 3 mm in height is ~ 9 8 * 10^6 photons nm^1

This flux is incident onto the grating which has an iridium coating with an estimated reflectivity of ~ 20 % at the blaze wavelength of 80 nm and therefore the flux focused at the dispersion plane of the instrument with a linear dispersion of ~ 0 83 nm mm^1 is ~ 1 6 * 10^6 photons mm^1 or equivalently,

~ 4 1 * 10^4 photons per pixel,

assuming a detector with pixels 25 µm in width If an extended source is considered (1 45 mm in diameter) the illuminated area of the grating will in this case be approximately ~ 12 mm in height and ~ 4 mm in width

4.4.2   System with additional focusing optic

In the case of the aperture matched system the GCA is positioned 218 mm from the source due to the necessary in-line valve The acceptance angle of the GCA

is therefore ~ 28 * 10^2 radians with the same optical transmission of ~ 30 % The

flux incident onto the concave mirror will be ~ 5 8 * 10^9 photons nm^1 Considering

the reflectivity of the concave mirror to be ~ 20 % @ 80 nm the flux focused on the

spectrometer's entrance slit plane is ~ 1 2 * 10^9 photons nm^1 Assuming the focus is

approximately the same size as the source the slit will have an effective transmission

of ~ 9 % and the flux incident on the grating will be ~ 1 1 * 10^8 photons nm^1 The

grating has a surface reflectivity of ~ 20 % @ 80 nm and so the flux focused at the

dispersion plane of the instrument with a linear dispersion of ~ 0 83 nm mm^1 is

~ 1 8 * 10^7 photons mm^1 or equivalently,

~ 4 4 * 10^5 photons per pixel,

assuming a detector with pixels 25 μm in width If an extended source is considered

(1 45 mm in diameter) the illuminated area of both the spherical concave mirror and

grating will be approximately ~ 28 mm in diameter

The increase in throughput is therefore a factor of ~ 11 assuming the

estimates on reflectivity of the concave mirror are correct and the source can be

accurately modeled as a point source This latter assumption has the effect of

increasing the difference between the calculated throughput of the two arrangements

In reality, the laser produced plasma will emit VUV light within a volume which

depends on the observation wavelength and focus conditions as well as target

material Experiments on a tungsten target with the use of a 525 μm wide spatial

resolving slit indicates that the source size at a wavelength of ~ 50 nm has dimension

which are approximately 1 45 mm in diameter as measured at FWHM of intensity

4 5   Shadow ray trace results

Shadow is a software suite which uses Monte Carlo[†] methods to model ray

traces in optical systems predominately used in the XUV and soft x-ray wavelength

regions It was initially written for the UNIX operating system but has been ported to

other platforms in recent years Through successive application of the physical laws

---

[†] Monte Carlo   Describes a mathematical technique used in modeling of physical systems where the
variable or variables – in this case the source emission features – follow random distributions

of reflection, refraction and attenuation Shadow traces the path of individual rays using vector algebra with a minimum use of trigonometric functions Work was done using Shadow in order investigate the following topics

- General spectrometer understanding
- Throughput calculations and comparisons
- Misalignment errors
- Spatial resolution properties with the use of slits and apertures

The laser produced plasma was assumed to be a spherical light source with diameter 1 45 mm estimated from space resolved measurements on a tungsten plasma and uniform radiance with respect to position in source volume as well as angle of observation Other sizes and types of sources (e g point, disc shaped etc) were used in the initial testing of the ray traced system A conical source divergence was used with a half angle chosen to ensure that as many rays as possible were conserved while still completely filling the effective aperture defined by the GCA The maximum number of individual rays which can be traced is 25000 although a number of results of runs with different random number seeds can be summed together to provide better statistics Although Shadow allows for capillary based optical elements to be included, in practice it was found that the code was more suited to longer length capillaries (i e Kumohov optics etc) and gave inconsistent results when trying to model the GCA directly It was however modeled as an effective circular aperture with a radius of $d/l * r$, where r is the distance to the source ($r = 170$ mm in the case of direct coupled system and 218 mm in the system including the focusing optic) with a maximum radius of 3 mm defined by the iris effect of the GCA holder The transmission of the GCA is estimated to be ~ 30 % for rays which fall within this effective aperture [Lucatorto et al, 1979] The spectrometer was modeled in Shadow using a manual translational, x, of the grating given by E 4-1 (b) and allowing Shadow to calculate the necessary rotational angle internally for the chosen center wavelength on the detector plane

$$\varphi = \sin^{-1}\left(\frac{m\lambda}{2d\cos(D_v)}\right)$$ [E 4-1 (a)]

$$x = R(1 - \cos(\varphi)) \qquad [\text{ E 4-1 (b) }]$$

where R (995 4 mm) is the focal length of the concave grating, m is the spectral order, λ is the central wavelength of interest, d (1/1200 * 10^3 m) is the inter groove spacing of the grating and D_V is the deviation angle of the spectrometer No reflectivity of any optical component was considered explicitly in the ray tracing model Rather it was accounted for in throughput calculations by reducing the number of rays reflected from a mirror surface in accordance with a reflectivity The blaze angle of the grating has no effect on modeling when reflectivity is not taken into account and so was ignored

Shadow also allows for both the rotational and translational movements of the source and optical elements in the system The optical element movements are defined by 6 variables, which describe the translations along the x-, y- and z-axis and rotations around the x-, y- and z-axis Movement of an optical element also moves any succeeding screens, apertures and slits connected to the particular optical element Therefore in order to model a planar detector fixed in space, while allowing the grating to be moved, an optical element consisting of a reflective planar mirror was used which was tangential to the Rowland circle

Shadow uses a Cartesian coordinate system and refers all of the ray components to this reference frame The resulting output data files are in binary format and include columns containing x, y and z axis ray coordinates as well as x', y' and z' coordinates in phase space The coordinates defining rays on a particular mirror, lens or grating optical element may be plotted by use of the data in x and y columns The coordinates for rays intercepting a particular continuation plane, slit, aperture, screen or source may be plotted by use of the data in the x and z columns The phase space (sometimes referred to as momentum space) coordinates contain information on both the vertical and horizontal focusing conditions and also on the astigmatism and other aberrations present in the optical system An ideal focusing system would result in a straight line in phase space, a deviation from this straight line directly indicates the existence of aberrations within the optical system Phase space is composed of co-ordinates which describe the angle the ray makes with the

117

propagation direction, z' in the case of reflecting or refracting optical components

and y' for all others [Shadow User's Guide, 1994]
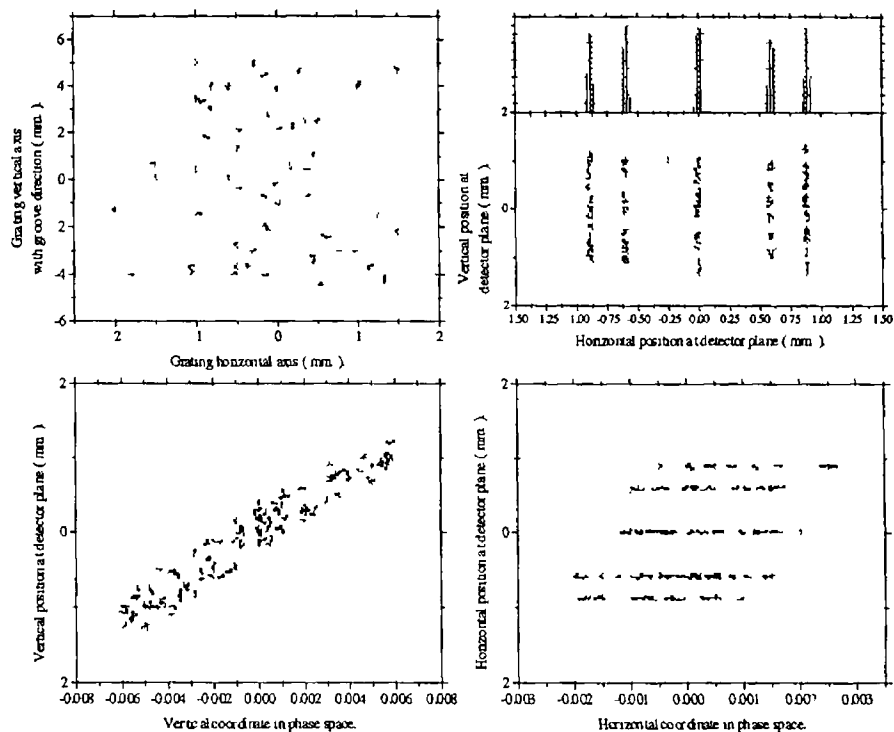
Figure 4-3   Shadow ray trace results with direct coupled system   Source size

1 45 mm spherical diameter, conical half angle divergence   0 004 radians, multi-

line   79 5, 79 25, 80, 80 5 and 80 75 nm and uniform angular radiance   Number of

initial rays   25000 (upper left) Beam footprint on grating and (upper right)

image at dispersion focal plane and histogram with 25 μm bins (lower left) vertical

axis phase space and (lower right) horizontal axis phase space

It can be seen from figure 4-3 (upper left) that the illuminated width of the

grating with the direct coupled system using a slit of width 50 μm and height 3 mm

is approximately 4 mm * 10 mm and is the result of the small source size and

position of GCA and spectrometer slit   This illuminated width did not change

significantly with wavelength although the central position of the illuminated

footprint moved horizontally on the grating   The latter result is the inherent

consequence of the McPherson mount   The optic axis defined by the centre of the

grating to the entrance slit is not fixed but varies slightly with wavelength   This

displacement of the optic axis can be calculated by simple geometry for the McPherson type mount and is given by the following equation,

$$\theta = \sin^{-1}\left(\frac{x\sin(7\,5)}{x^2 + (R\cos(7\,5))^2 - 2xR\cos(7\,5)^2}\right) \qquad [\text{E 4-2}]$$

where R is the radius of curvature, 995 4 mm, and x is the displacement as given by equation 4-1 (b)
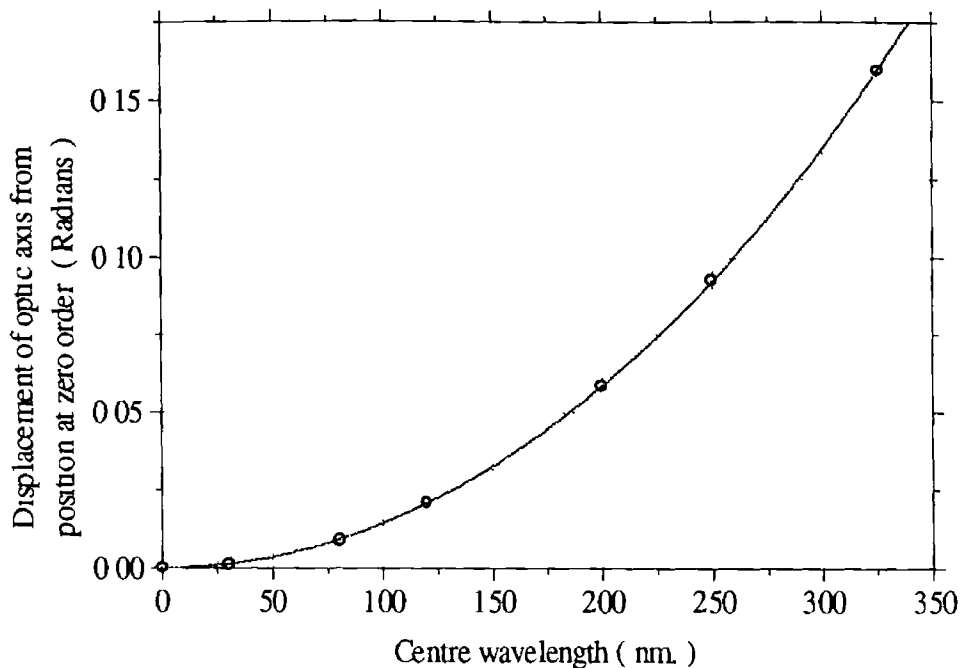
Figure 4-4   Graph showing the displacement of the optic axis from position at
zero order as given by equation 4-2

The height of the spectral lines are dependent on the wavelength for which
the grating is tuned and is ~ 2 6 mm @ 80 nm The stigmatic property of the
instrument is displayed in figure 4-3 (lower left) where the straight line centred at
the origin indicates a linear relationship between the vertical position of a particular
ray on the detector plane and its distance from the vertical focus For a truly
stigmatic instrument the slope of this data represents the reciprocal of the distance to
the vertical focus The optimum horizontal focus (i e that focus that gives sharpest
spectral lines) is very close to the grating position as given by equation 4-1 (a) and
(b) This is evident from the fact that the data points in figure 4-3 (lower right) are
symmetric around the x-axis in horizontal phase space at the position of the detector
plane On the lower wavelength side of the chosen centre wavelength region the
spectral lines are observed to be focused (horizontally) closer to the grating while
on the higher wavelength side the spectral lines are focused (horizontally) further
from the grating It was found that the maximum deviation, as predicted by Shadow,
from optimum horizontal focus across the entire detector plane (of width ~ 25 mm)
was approximately ± 10 μm In practice this small off focus distance for wavelengths

at the edge of the detector does not interfere with the resolution capability of the Acton™ spectrometer when using the CEMA / PDA detector arrangement
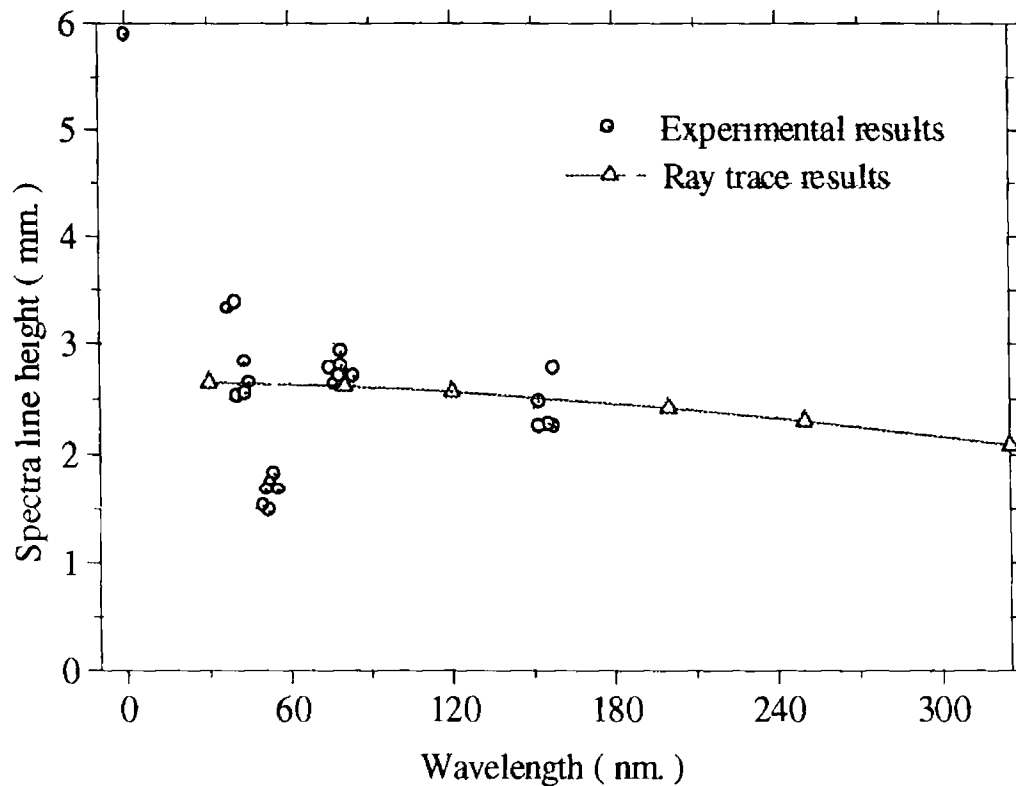
Figure 4-5   (solid line) Graph of spectral line height versus wavelength for direct-coupled system as predicted by ray trace results with 1 45 mm spherical monochromatic source, conical half angle divergence of 0 004 radians and uniform angular radiance   The maximum extent of the ray co-ordinates at the detector plane were used to quantify the height of the spectral line and (circular data point markers) experimental spectral line height for identified lines

In figure 4-5 it is seen that the spectral line height as predicted by the ray tracing varies with regard to the wavelength of the particular line   Although the curvature of such lines is predicted by theoretical considerations, at near normal incidence and with the use of relatively large slit heights, the curvature is not apparent in ray traced or experimental results   The experimental spectral line height was recorded by the use of the direct illuminated back-thinned CCD array detector for the spectral range 30 to 160 nm with the upper wavelength limit set by lack of signal   The zero order spectral line is approximate 6 mm in height, measured as

121

FWHM and being composed of predominantly visible light which is emitted from a larger source size deviates substantially from the trend predicted by the ray traced results Identified spectral line heights versus wavelength were plotted in both first and second and third order Apart from were the lines are very intense at ~ 50 nm the results show a gradual decrease in line height with increasing wavelength which follows that as predicted by the ray trace results indicating that a diameter of ~ 1 5 mm is a good estimate for the average source size in the VUV in the present experimental arrangement

Once the direct coupled spectrometer arrangement was ray traced in Shadow and the focusing condition was confirmed (translational and rotational movements given by E 4-1 (a) and (b)) for the entire spectral range of the instrument the additional mirror was included and the GCA was repositioned 218 mm from the source The spectrometer part of the model was unchanged from that used in the direct coupled system with the exception of the mirror orientation angle of the grating (changed from 0 ° to 180 °) and the planar mirror acting as a detector (changed from 180 ° to 0 °) A schematic of the modeled system showing axis conventions and labels of individual optic components as used by Shadow is displayed in figure 4-6

Rotational movement
around x-axis

Translational movement along z-axis

x

z

y

x

y

z

Spherical concave grating
Mirr 02
Orientation angle 180 °
z-translation and x-rotation given
by equation 4-1 (a) and (b)

Detector plane
Mirr 03
Orientation angle 0 °

x

Spectrometer slit
50 μm * 3 mm
Screen0201 dat

y

z

x

y

z

GCA
Circular aperture
3 mm diameter
Screen 0101 dat

Laser plasma source
Modelled as circular
emitting disc 1 45 mm in
diameter with no depth
Begin dat

x

y

z

Spherical concave mirror
Focal length 500 mm
Diameter 50 8 mm
Mirr 01
Orientation angle 0 °

Figure 4-6   Schematic of optical system showing co-ordinate system as used by
Shadow in the modelling of the system with additional focusing element The system
is composed of three optical elements (mirr 01, mirr 02 and mirr 03 as labelled by
shadow), an entrance slit attached to grating optical element and a circular
aperture (serving to model the GCA) Other apertures were also included in order
to observe the extent of the collected light at various different distances from the
source
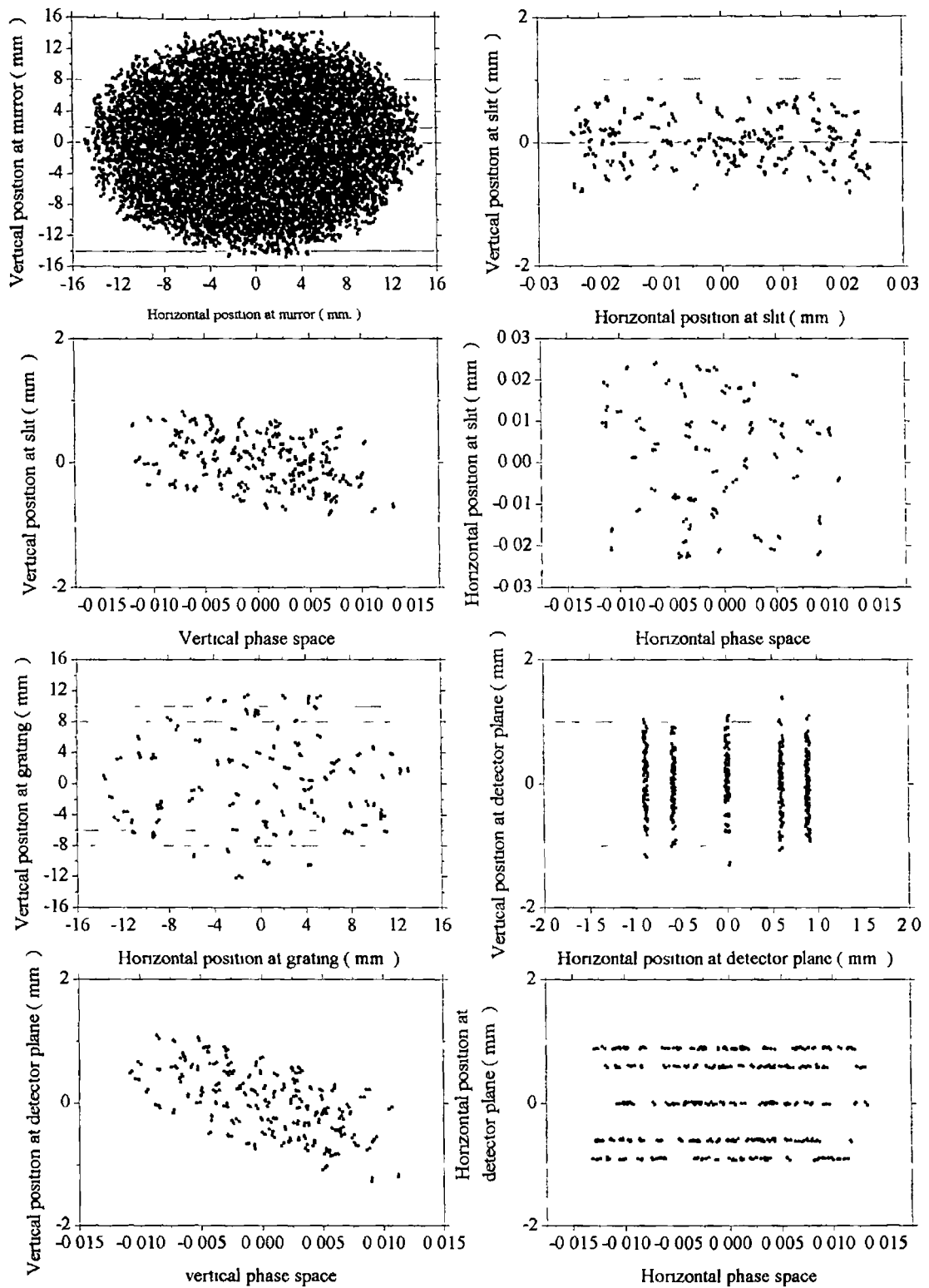
Figure 4 7   Shadow ray trace results with the additional focusing optic Source size 1 45 mm spherical diameter, conical half angle divergence   0 02 radians, multi-line   79 5, 79 25, 80, 80 5 and 80 75 nm and uniform angular radiance Number of initial rays   25000 Working from left to right, top to bottom (a) Footprint on spherical concave mirror, (b) foot print on slit showing only accepted rays, (d) vertical phase space at slit plane, (e) horizontal phase space at slit plane, (f) foot print on grating, (g) foot print on detector plane, (h) vertical phase space at detector plane and (i) horizontal phase space at detector plane

From figure 4-7 (a) it can be seen that the illuminated width of the concave mirror is approximately 28 mm in diameter The portion of the slit which is passing light is approximately 50 μm * 1 9 mm The width of the grating illuminated is approximately 27 mm in the vertical direction and 25 mm in the horizontal direction
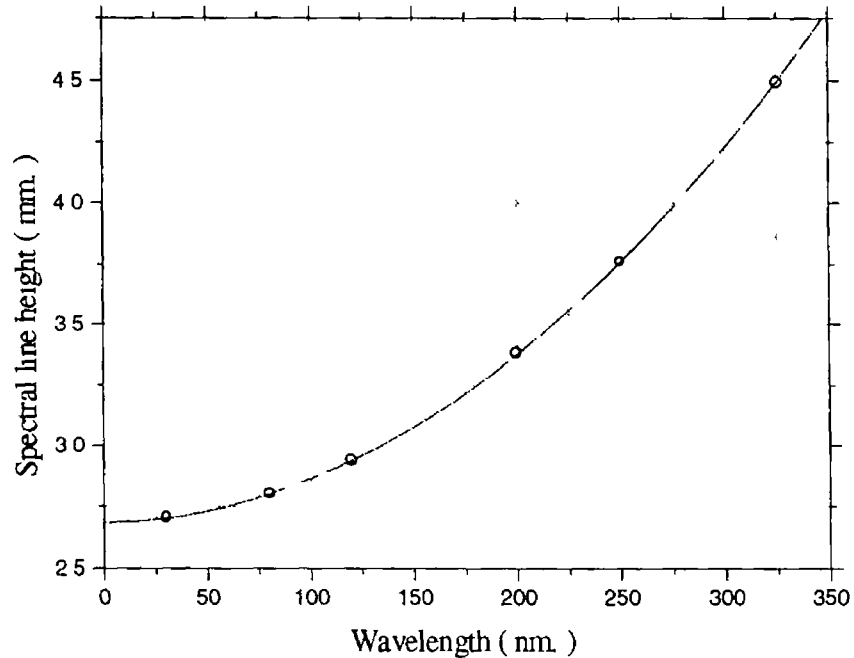
Figure 4-8   Graph of spectral line height versus wavelength for system with additional focusing optic as predicted by Shadow The maximum extent of the ray co-ordinates at the detector plane were used to quantify the height of the spectral line

From figure 4-8 it can be seen that the variation of spectral line height with wavelength displays a different shape than the direct-coupled system In the direct-coupled system the complete entrance slit of the spectrometer was filled The instrument effectively images this slit onto the dispersion plane with unit magnification and the result is a more gradually varying function with respect to wavelength (figure 4-5) In the case of the system with the additional focusing element, the instrument effectively images a point source which achieves better filling of the grating and therefore the astigmatism and curvature due to coma of the instrument is more pronounced

The throughput improvement can be estimated by considering the flux at each optical element and taking account of the surface reflectivity of both the mirror and

grating. The surface reflectivity of the concave mirror was estimated at ~ 20 % for an iridium coating (from reflectivity data from Acton™). The GCA position is 170 mm from the source in the case of the direct-coupled system and 218 mm from the source in the system including the focusing optic.

	Direct coupled system.	Addition of the focusing optic.
Initial number of rays.	25000.	25000.
Rays which pass GCA.	17276.3.	11771.
Rays which reflected from concave mirror.		2354.2.
Rays which pass slit.	20.4.	110.8.

Table 4-9.   Summary of Shadow throughput results. The source parameters remained the same for each system and a number of data-sets (10 in both cases) were averaged to achieve better statistics.

From a comparison of the ray traced results displayed in table 4-9, the throughput of flux with the system incorporating the spherical concave mirror is approximately 5 times that of the direct coupled system. It must be pointed out that this figure represents the maximum one can expect, as the system in practice will contain misalignments and possibly poor focusing. Also the efficiency of the additional mirror and most especially the grating will be a function of wavelength and therefore the increase in flux will also be a function of wavelength.

4.6   Preliminary construction and alignment of system with additional focusing optic.

Before assembling the complete vacuum optical beamline each main section was separately vacuum tested for leaks. When satisfied that no such leaks were present the mirror chamber section was fixed temporally to the supporting table and both the table and the mirror chamber were leveled and adjusted in height to suit the spectrometer entrance arm flange (see figure 4-1). An alignment laser was positioned in the holder attached to the target chamber and was adjusted to make the beam central to 6 mm bore of the GCA holder (the actual GCA was not included in the system at this stage). It was important to ensure that the alignment laser was

normal to the GCA holder flange This was achieved by minimizing the distance between back reflections of a half-silvered mirror and the rear window of the target chamber The target chamber was moved in-order to center it with the optic axis of the mirror chamber and also to locate the source position to 1000 mm distant from the estimated mirror position It was found that a half-silvered mirror when held against the entrance flange of the mirror chamber would allow further alignment to be made by the use of the back reflection thus ensuring that the alignment laser was normal to the front face of the flange

Removal of the CEMA flange allowed an alignment laser to be positioned at the exit arm of the spectrometer by passing it back through the grating and entrance slit defining the optic axis of the spectrometer Further use of the half-silvered mirror allowed the spectrometer alignment laser to be aligned normal to all spectrometer flanges as well as the exit arm flange of the mirror chamber by small adjustments to mirror chamber support table and spectrometer support table At this stage a plane mirror was positioned at the location of the concave mirror and using the half-silvered mirror each alignment laser was verified to lie on the optic axis

The plane mirror was replaced with the concave mirror and the focusing condition was verified by attaching a small light bulb to the target holder and using the filament as an object Any necessary changes to the target chamber to mirror chamber distance and / or mirror chamber to spectrometer distance was followed by a repeat of the above alignment procedure with the plane mirror As the mirror chamber consisted of long 40 mm diameter tubes with 40 KF flanges for convenience, the pump down time was increased greatly It was found that after 3 to 4 days the mirror chamber reached an ultimate pressure of $3 * 10^{-6}$ mBar as measured by a penning gauge positioned on a tee piece close to the spectrometer entrance slit

	Before spectrometer and target to mirror chamber flange opened	After spectrometer and target to mirror chamber flange opened
Target chamber	$1\ 6 * 10^5$ Torr	$7\ 9 * 10^{-6}$ Torr
Mirror chamber	$3\ 5 * 10^{-6}$ Torr	$2\ 9 * 10^{-6}$ Torr
Spectrometer pressure	$1\ 3 * 10^{-6}$ Torr	$1\ 2 * 10^{-6}$ Torr

Table 4-12   Typical target, mirror and spectrometer chamber pressures before and after target chamber to mirror chamber and mirror chamber to spectrometer chamber in-line valves are opened

In the design and construction of an optical system some consideration must be placed on the possible sources of misalignment and sensitivity to such misalignments especially if the optical system is enclosed in a vacuum chamber where adjustment of the optical elements may be difficult to achieve Although some form of initial alignment at atmospheric pressure is crucial if close to optimum conditions are to be reached, the process of pumping the system down may lead to movement of one or more of the aligned components So long as this drift can be compensated for with relative ease, absolute fixture of the optical components may not be of primary importance when considering cost and size of support tables

The initial testing consisted of positioning a laser plasma source on the optic axis of the spectrometer system and moving the grating to the zero order position It was observed that the original alignment was somewhat disturbed upon pump down and therefore it was necessary to scan the resulting focused image of the source across the spectrometer's entrance slit horizontally by rotation of the concave mirror Once the zero order spectrometer image was observed the concave mirror was scanned in the vertical direction to optimize the detectors counts Although the zero order signal displayed high intensity it was found to be predominantly of visible light This was confirmed by use of a glass plate on the second target holder to attenuate the VUV portion ($\lambda < 200$ nm) of the zero order signal Movement of the glass microscope slide to a position between the source and mirror resulted in little

change to the zero order signal strength The zero order signal is displayed in figure
4-13 with and without the glass microscope slide attenuating the source emission
The amount of VUV light contained in the un-attenuated emission is estimated to be
6 %

A mercury spectral lamp was also used and allowed for the testing of the
experimental arrangement at the longer wavelength extreme ($\lambda > 270$ nm) The rear
window of the target chamber was replaced by a quartz window and a quartz lens
was used to couple the visible and UV light to the spectrometer slit Although the
spherical concave mirror should have a high reflectance in this spectral region no
mercury emission lines were observed This was due to the extremely poor efficiency
of the grating in this region which is far from the blazed wavelength Therefore, the
spectral region were the grating is efficient ($\lambda < 100$ nm) and that spectral region
were the spherical concave mirror is efficient ($\lambda > 160$ nm) do not overlap and so
no spectral signal can be observed

With glass microscope slide
Peak counts 3535

Without glass microscope slide
Peak counts 3748

PDA detector counts

Pixel address

Pixel address
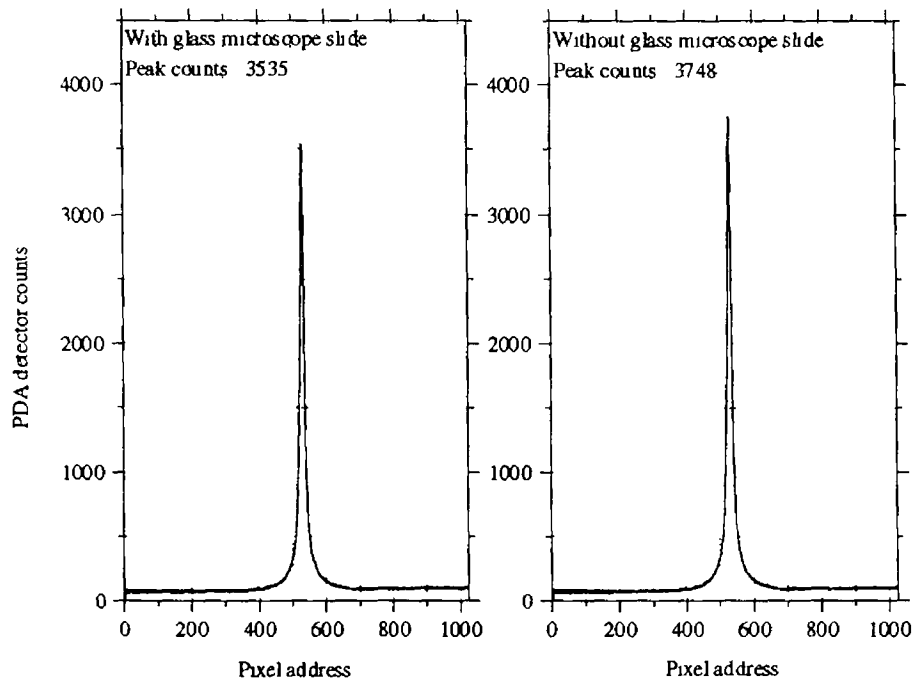
*Figure 4-13   Single shot zero order signal recorded by the system arrangement
including the mirror chamber and using the emission from a polyethylene plasma
with (a) and without (b) attenuation of the VUV emission by a glass microscope
slide Spectrometer slit 20 μm.*

4 7   Concluding remarks on system modeling.

The focusing of collected VUV radiation onto the slit has been shown to increase system throughput even though the additional focusing optical element has relatively low reflectivity of approximately 20 % The increase has been estimated using both simple geometric arguments and also through the use of a ray tracing modeling software The increase predicted by the simple preliminary calculations (~ 11) is found to be much higher than that predicted by the ray tracing experiments (~ 5) This can be attributed to the fact that a point source is an over simplification which does not correspond to the source used in the ray traced model

In practice the reflectivity of the additional mirror will be a function of wavelength and will also have misalignment errors in position and so the increase might well be lower than the ray trace results suggest The efficiency of the grating will vary more with wavelength than the spherical concave mirror due to the fact that the grating is blazed for a single wavelength

The height of the resulting spectral lines have been shown to follow quite different trends in the case with the source positioned a distance 382 mm away from the spectrometer entrance slit and that with the an additional concave mirror focusing the source object on to the spectrometer In the former case the height of the spectral lines as predicted by Shadow decreases gradually with increasing wavelength, 2 6 mm @ 30 nm to 2 1 mm @ 325 nm When the source object is focused onto the spectrometer entrance slit the spectral line height changes dramatically from 2 7 @ 30 nm to 4 5 mm @ 325 nm By using an array detector the resulting intensity reduction at the detector plane can be compensated by binning the pixels in the vertical direction Experiments using an array detector similar to the Andor™ back thinned CCD yielded spectral line heights for the wavelength range 30 to 160 nm similar to that predicted by the ray trace model It was not possible to get accurate spectral line height measurements above 160 nm due to level of spectral signal The similarity in spectral line height between that of the ray trace results and also from experimental measurements indicates that the source size used in the ray trace results (~ 1 45 mm) is indeed close to the emitting source size in the experiments

The translational movement of the grating displaces the optic axis of the spectrometer instrument from its position at zero order given by equation 4 2 Although the displacement is relatively small and does not interfere with experiments using the direct-coupled arrangement, the displacement may in fact cause problems when the system is used with an additional focusing optic and precise alignment of the optical components is necessary

The misalignment error associated with the additional focusing optic with respect to position relative to optic axis (x-y plane in figure 4-4) and displacement of mirror from ideal focusing position (z-axis in figure 4-4) have a dramatic effect on the flux throughput of the system This is mainly due to the long lever arm effect of the beamline and therefore accurate angle movement of the mirror is critical

Although an intense zero order signal was recorded it was mainly composed of visible light and so there was insufficient flux throughput in the entire spectral range covered by the instrument In the short wavelength extreme of the spectral range of the instrument, $\lambda < 100$ nm the grating is efficient due to operation close to the blazed wavelength The quantum efficiency of the Galileo™ CEMA / EG&G™ PDA decreases rapidly at wavelengths longer than approximately 180 nm The reflectivity of the spherical concave mirror available at the time of the experiments is now known to have negligible reflectivity in this region Therefore no region exist where both the grating and spherical concave mirror is efficient

Chapter 5. Concluding remarks

A multichannel normal incidence VUV spectrometer system has been described which enables both emission and absorption studies to be made on laser produced plasmas Two detection configurations were used in the experiments, one a Channel Electron Multiplier Array / Photo Diode Array (CEMA / PDA) combination, the other a direct illuminated back thinned charge coupled device (CCD) Various emission studies were performed on line as well as continuum dominated plasmas in order to characterise the instrument's wavelength range, extent of order overlapping and wavelength resolution The suitability of the spectrometer system for photoabsorption measurements was accessed by such experiments as absorption by gas as well as by a secondary plasma plume as in the DLP technique The design, construction and preliminary testing of a normal incidence focusing optic was presented in chapter 4 The improvement in terms of light gathering ability has been illustrated by both simple geometric calculations as well as by ray tracing

5 1   Conclusions and observations

Although the wavelength range possible with the present grating and mount extends from 30 to 325 nm the poor efficiency of the grating and problems with order sorting limits absorption studies to approximately 35 to 80 nm without the use of filters however emission studies in the range 35 to 325 nm are possible and the instrument is routinely used up to 220 nm for this purpose

The Galileo™ CEMA intensifier and EG&G™ PDA detector arrangement provide reasonable wavelength resolution The spectral lines from line dominated emission spectral are typically 6 to 7 pixels (FWHM) with a corresponding linear dispersion of ~ 0 021 nm pixel^{1} m first order Spectra obtained using the Andor™ back thinned CCD had spectral lines typically 3 to 4 pixels in width (FWHM) with a corresponding linear dispersion of ~ 0 022 nm pixel^{1} in first order The binning of the pixels of the CCD array in the vertical direction did not decrease the wavelength resolution achievable

Generally speaking, the comparison of the detector sensitivity is rather crude because many of the factors involved, such as gain and efficiency of the detection

device, are strong functions of other parameters Since the gams on both the MCP and of the phosphor screen stages of the CEMA are steep functions of applied voltage, and the CCD dark noise also depends on the operation temperature, an estimate of the sensitivity is more qualitative than quantitative The CEMA / PDA detector arrangement with a CEMA bias of 2500 / 800 V (V_{Gap} / V_{Plate}) showed a similar sensitivity range as that of the Andor™ back thinned CCD over the entire range of the spectrometer Both detectors show good single shot sensitivity at wavelengths below about ~ 140 nm The back thinned CCD with it's inherently low noise and 16 bit ADC has a higher dynamic range than the CEMA / PDA based detector

Photoabsorption measurements on both gas and secondary plasma plumes are possible in the wavelength range approximately from 30 to 80 nm with the upper limit determined by the falloff in efficiency of grating Both samarium and tungsten plasma prove to be good backlight sources for reproducible continuum emission The samarium plasma emission in the normal incidence VUV region is essentially 'line free' with some spectral lines arising from lower ion stages and also from oxygen present as a surface contaminant The reproducibility of these low ion stage features is excellent and it is the oxygen line emission which is responsible for some of the peaks in the ratio plots

The average flux of the emission (centred at ~ 50 nm) from a samarium plasma is reproducible to ~ 2 % when the Spectron™ SL803 laser is used in contrast to ~ 16 % with use of the JK Lasers™ Ruby laser Although the tungsten emission is characterised by numerous lines, the reproducibility of these lines is excellent Therefore, a tungsten plasma is also ideal for use as a backlight as the collected emission is stable over hundreds of shots without rotation to a fresh surface The reproducibility of the continuum emission is improved by incorporating a secondary slit of suitable width between the spectrometer slit and the source This reduces the effect which the variation of source size has on the collected flux The use of a secondary slit is also important in DLP photoabsorption studies for limiting the region through which the collected continuum backlight passes

The inclusion of such a secondary slit has numerous advantages These include, (1) limiting the amount of front plasma emission collected by the

spectrometer, (2) limiting the range of species present in photoabsorption measurements and (3) reducing the amount of continuum signal collected which has not passed through the absorption plume and also reducing the scattered light present in general

Also it is important to note that saturation in photoabsorption measurements reduces the wavelength resolution achievable as well as increasing the effect the underlying noise has on the relative photoabsorption cross sections. The system parameters which determine the saturation level include (1) detector noise, (2) stray light, (3) higher order light present and (4) strength and reproducibility of backlight emission, I_0.

Higher order contributions have been observed to dominate at wavelengths above ~ 100 nm. By use of a gas such as helium or argon this upper limit may be extended to ~ 140 nm. Solid state filters are limited by their high absorption of VUV light above about ~ 100 nm.

In chapter 4 the design, construction and preliminary testing of the spectrometer system with an additional focusing element is described as well as the benefits of such a system. Although both the simple geometric calculations as well as ray trace results suggested that the throughput would be increased with the introduction of the focusing optic, no spectral data could be obtained in experiments to verify this. The main difficulty encountered was the poor reflectivity of the aluminium mirror with MgF_2 coating. It was evident that the wavelength range were the grating was efficient (30 to approximately 120 nm) did not overlap that range for which the additional concave mirror (aluminium with MgF_2) had an adequate reflectivity. In view of this an iridium coated mirror is presently on order from Acton™.

The focusing of collected VUV radiation onto the spectrometer slit has been shown to increase system throughput even though the additional focusing optical element has relatively low reflectivity of approximately 20 %. The increase has been estimated using both simple geometric arguments and also through the use of a ray tracing modelling software. The increase predicted by the simple preliminary calculations (~ 11) is found to be much higher than that predicted by the ray tracing

experiments (~ 5) This can be attributed to the fact that a point source is an over simplification which does not correspond to the source used in the ray traced model

Spatial resolution can be important for photoabsorption studies as the dominant ion stage can be selected somewhat by imaging a specific portion of the plume onto the entrance slit of a spectrometer The use of a slit allows for the collection of light from a vertical chord of the plasma plume Usually slits reduce the amount of light coupled into an optical system reduces considerably and therefore the signal to noise ratio of the recorded spectrum suffers Hence it is important that the system is as close to aperture matched as possible

In practice the reflectivity of the additional mirror will be a function of wavelength and will also have misalignment errors in position and so the increase might well be lower than the ray trace results suggest The efficiency of the grating will vary more with wavelength than the spherical concave mirror due to the fact that the grating is blazed for a single wavelength

Although an intense zero order signal was recorded it was mainly composed of visible light and so there was insufficient flux throughput in the entire spectral range covered by the instrument In the short wavelength extreme of the spectral range of the instrument, $\lambda < 100$ nm the grating is efficient due to operation close to the blazed wavelength The quantum efficiency of the Galileo™ CEMA / EG&G™ PDA decreases rapidly at wavelengths longer than approximately 180 nm The reflectivity of the spherical concave mirror available at the time of the experiments is now known to have negligible reflectivity in this region Therefore no region exist where both the grating and spherical concave mirror is efficient
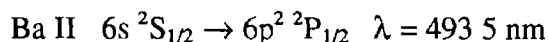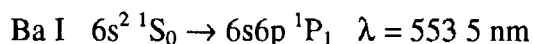
5.2   Future developments

Some of the planned applications of this normal incidence VUV spectrometer instrument are briefly described below

5 2 1   Laser driven ionization of a laser generated barium plasma

When a DYE laser with a pulse energy of greater than ~ 200 mJ and pulse duration of typically 500 ns is tuned to a resonance or intercombination transition of an atomic species, it will produce almost complete ionization of a metal vapour within typically a microsecond of the initial irradiation [Lucatorto and McIlrath, 1980 and Kent *et al*, 1987] The ability to form a controlled ionized sample of a metal vapour with all of the ions residing in the ground state makes RLDI ideally suited to absorption studies

The RLDI technique was first performed by both Lucatorto and McIlrath, [1976] to study the absorption spectra of various metal vapours including lithium, sodium, manganese and barium These results permitted temporal measurements on the state of ionization of the sample and also provided data on the mechanisms involved in the ionization

Some of the necessary pumping transitions are shown below all of which are readily obtainable with a DYE laser [Kallenbach *et al*, 1986]

$$Ba\ I\quad 6s^2\ {}^1S_0 \rightarrow 6s6p\ {}^1P_1\quad \lambda = 553\ 5\ nm$$
$$Ba\ II\quad 6s\ {}^2S_{1/2} \rightarrow 6p^2\ {}^2P_{1/2}\quad \lambda = 493\ 5\ nm$$

5.2 2   Gating of channel electron multiplier array

XUV and VUV imaging of laser produced plasmas have often used channel electron multiplier array (CEMA) devices because of their high spatial resolution (typically 40 lp mm ^{1} for 10 μm pore diameters) and high gain (typically 10^5 for a single stage device) [Galileo™, 1986] Normally a steady state dc voltage is used to bias the intensifier thus producing time-integrated images of the plasma In photoabsorption studies, it is possible to use a second plasma as a continuum source

This allows for the 'natural' gating of the photoabsorption of the front sample plasma with a temporal resolution of the order of the duration of the continuum back-light. In the XUV region, the continuum emission duration follows that of the excitation laser pulse duration. At longer wavelengths, the continuum emission is significantly longer. In the case of temporally resolved emission studies some form of intensifier or detector gating is required.

Time resolution in the nanosecond or sub nanosecond range may be achieved using uni-dimensional streak cameras. Quite often the plasma displays axial symmetry and so the spatial resolved image of a single dimension is acceptable. A detector which exhibits bi-dimensional spatial resolution and very short time resolution would be advantageous in viewing the complete plasma in both spatial dimensions [Luppi *et al*, 1984].

One way such a bi-dimensional detector could be realised would be to gate the bias voltage of a CEMA based intensifier. Producing a transient high potential pulse with sharp transition times is difficult because component and stray capacitance must be kept to a minimum and also devices must be used that can both handle the high voltage and high peak power of the pulse. Circuits for such gating usually consist of power MOSFETS or avalanche bipolar transistors [Fulkerson and Booth, 1994].

On avalanching, a bipolar transistor can be made to produce extremely fast, high peak current pulses. Most transistors are capable of producing an avalanche response but only a few are able to produce a reproducible and sustained operation. Recently a number of transistors which are characterised specifically for avalanche pulse operation have become available, namely the ZTX415 from Zetex Semiconductors™. The avalanche transistor depends for its operation on the negative resistance characteristic at the collector. When the collector voltage exceeds a certain level, somewhere between V_{ceo} and V_{cbo}, depending on the circuit configuration, the voltage gradient in the collector region exceeds the sustained field strength, and electron-hole pairs are liberated. These are accelerated by the field, liberating others in their turn. Consequently, the current increases rapidly, although the voltage across the device is actually falling [Zetex Semiconductors™, 1996 and Hickman, 1996].

5.2.3 Application to FEL characterisation.

It has been decided that the Acton™ VM 521 normal incidence VUV spectrometer will be used in the characterisation of the free electron laser (FEL) experiment located at DESY synchrotron facility Hamburg in Germany. In a conventional laser, the emission of photons results from the transitions of atom-bound electrons from a higher to lower quantum state. In the free electron laser, the electrons that produce the photons are not bound to any atom but are free; they are generated in an electron accelerator and emit coherent radiation as they undergo periodic oscillations within an insertion device such as an undulator. Although the emission from insertion devices presently in use is coherent it is not monochromatic and the radiation and therefore the power is distributed across a broad wavelength range (IR to VUV).

By increasing the length of the undulator it becomes possible to amplify a desired wavelength which can be tuned by varying the period between the magnets in the undulator or varying the energy of the electrons entering the undulator. The operation of the proposed FEL will be based on self amplification of spontaneous emission (SASE) and therefore will not require a seed laser to initiate lasing action. As the proposed design uses a single pass of the undulator to provide adequate amplification it removes the necessity of obtaining efficient mirrors suitable for operation at short wavelengths.

The grating in the Acton™ spectrometer will be replaced with one which has a higher groove density (either 2400 or 3600 lines mm^{-1}) thereby increasing the wavelength resolution of the instrument. It is proposed to incorporate a wedge behind the new grating to extend this coverage to 130 nm. Another possibility would be to get Acton™ to modify the grating mount to achieve the necessary coverage. A Photonics™ back thinned direct illuminated CCD detector similar to the Andor™ model described in previous chapters will be used to record the diffracted spectrum. Initial testing and alignment has shown that with the 1200 lines mm^{-1} grating a FWHM line width of just 2 pixels (approximately 0.2 nm pixel^{-1}) is readily possible with this detector. Calibration of the spectrometer instrument will be made through the use of a calibrated ECR source. This will provide both wavelength as well as

absolute efficiency across the entire range of the instrument The output from the

FEL will be coupled to the spectrometer with one of two arrangements, either a plane

mirror or a spherical concave iridium mirror

139

References.

Adams and Manley, 1965	Adams, J and Manley, B W 1965 *Electron Eng* Vol 37, Page 180
Adams and Manley, 1966	Adams, J and Manley, B W 1966 *IEEE Trans Nucl Sci* Vol 13, Page 88
Ballofet *et al*, 1961	Ballofet, G , Romand, J and Vodar, B 1969 *C R Acad Sci* Vol 252, Page 4139
Bekefi, 1976	Bekefi, G A 1976 *Principles of Laser Plasmas* Edition Wiley-Interscience
Bell, 1959	Bell, E E 1959 Radiometric Quantities, Symbols, and Units *Proceedings of the IRE* Paper 3 1 1 Page 1432
Bibinov *et al*, 1997	Bibinov, N K , Bolshukhin, D O , Kokh, D B , Pravilov, A M , Vinogradov, I P and Wiesemann, K 1997 Absolute calibation of the efficienc of a VUV monochromator / detector system in the range 110 - 450 nm *Meas Sci Technol* Vol 8 Page 773
Cantù and Tondello, 1975	Cantù, A M and Tondello, G 1975 Continuum source and focusing technique for the 80-500 Å spectral range Improvements *Applied optics* Vol 14 No 4, Page 996
Carillon *et al*, 1970	Carillon, A , Jaégle, P and Dhez 1970 *Phys Rev Lett* Vol 25, Page 140
Carroll and Kennedy, 1977	Carroll, P K and Kennedy, E T 1977 Doubly excited autoionization resonances in the absorption spectrum of Li$^+$ formed in a laser-produced plasma *Physics Review Letters* Vol 38, No 19 Page 1068
Carroll *et al*, 1980	Carroll, P K , Kennedy, E T and O'Sullivan, G 1980 Laser-produced continua for absorption spectroscopy in the VUV and XUV *Applied Optics* Vol 19, No 9, Page 1454
Carroll *et al*, 1981	Carroll, P K and Kennedy, E T 1981 Laser produced plasmas *Unpublished*
Carroll *et al*, 1983	Carroll, P K , Kennedy, E T and O'Sullivan, G 1983 Table-top EUV Continuum Light Source *IEEE Journal of Quantum Electronics* Vol 19, No 12, Page 1907
Celliers *et al*, 1995	Celliers, P , Mrowka, S , Matthews, D 1995 Optization of X-ray sources from a high-average power Hd Glass laser produced plasma for proximity lithography *UCRL-LR-105821-95-3*
Colombant and Tonon, 1973	Colombant, D and Tonon G F 1973 X-ray emission in laser-produced plasmas *J Applied Physics* Vol 44, No 8, Page 3524
Costello *et al*, 1991	Costello, J T , Mosnier, J P , Kennedy, E T , Carroll, P K and O'Sullivan, G 1991 X-UV absorption spectroscopy with laser produced plasmas A review. *Physica Scipta* Vol T34, 77-92
Cromer *et al*, 1985	Cromer, C L , Bridges, J M , Roberts, J R and Lucatorto, T B 1985 High-resolution VUV spectrometer with multichannel detector for absorption studies of transient

	species. *Applied Optics.* Vol. 24, No. 18, Page 2996.
Davidson *et al*, 1990.	Davidson, S.J., Neely, D., Lewis, C.L.S. and O'Neil, D. 1990. Rutherford Appleton Laboratory Report. No. RAL-90-026, 13.
Doyle, 1995.	Doyle, B. 1995. *A 1 m Normal Incidence Multi-Channel Spectrometer For Laser Plasma Spectroscopy.* M.Sc. Thesis. DCU. Unpublished.
Dyer *et al*, 1990.	Dyer, P.E., Issa, A. and Key, P.H. 1990. Dynamics of excimer laser ablation of superconductors in an oxygen environment. *Appl. Phys. Lett.* Vol. 57. No. 2. Page 186.
Echart *et al*, 1986.	Echart, M.J., Hanks, R.L., Kilkenny, J.D., Pasha, R. and Wiedwald, J.D. 1986. Large-area 200 ps gated microchannel plate detector. *Rev. Sci. Instrum.* Vol. 57, No. 8, Page 2046.
EG&G Princeton Applied Research™.	EG&G Princeton Applied Research. Models 1452, 1453 and 1454 silicon photodiode detectors. Operating and service manual. USA.
Ehler and Weissler, 1966.	Ehler, A.W. and Weissler, G.L. 1966. Vacuum ultraviolet radiation from plasmas formed by a laser on metal surfaces. *Applied Physics Letters.* Vol. 8, No. 4.
Fawcett *et al*, 1966.	Fawcett, B.C., Gabriel, A.H., Irons, F.E., Peacock, N.J. and Saunders, P.A.H. 1966. *Proc. Phys. Soc.* Vol. 88, Page 1051.
Fischer and Kühne, 1983.	Fischer, J. and Kuhne, M. 1983. Time duration of VUV-radiation emission of laser produced plasmas as a function of laser pulse length and wavelength of observation. *Applied Physics B.* Vol. 32, Page 157.
Fischer *et al*, 1984.	Fischer, J. Kühne, M and Wende, B. 1984. Spectral radiant power measurements of VUV and soft x – ray sources using the electron storage ring BESSY as a radiometric standard source. *Applied Optics.* Vol. 23, No. 23, Page 4252.
French, 1989.	French, R.H. 1989. Laser-plasma sourced, temperature dependent, VUV spectrophotometer using dispersive analysis. In. *Proceedings of the ninth Int. Vacuum Ultraviolet Radiation Physics Conference.* 1989. Hawaii.
Fried *et al*, 1991.	Fried, D., Jodeh, S., Reck, G.P., Rothe, E.W. and Kushida, T. 1994. Internal state populations and the time-of-flight of ground-state species ejected after the 193 nm excimer laser ablation of CuO, BaO_2, Y_2O_3. *J. Appl. Phys.* Vol. 75. No. 1. Page 522.
Fried *et al*, 1991.	Fried, D., Reck, G.P., Kushida, T. and Rothe, E.W. 1991. Time resolved emission spectra following the 193 nm photoablation of CuO, BaO_2, Y_2O_3, and $YBa_2Cu_3O_{7-x}$ in vacuum and oxygen. *J. Appl. Phys.* Vol. 70. No. 4. Page 2337.
Fulkerson and Booth, 1994.	Fulkerson, E.S. and Booth, R. 1994. Design of Reliable High Voltage Avalanche Transistor Pulsers. Lawrence Livermore National Laboratory. http://www-dsed.llnl.gov/documents/pulser_tech/esfpms94.html. [

	Accessed date 05/04/96]
Galileo™, 1985	Galileo™ 1985 MCP tech notes Vol 4
Geohegan, 1992	Geohegan, D B 1992 Fast intensified-CCD photography of YBa₂Cu₃O₇ δ laser ablation in vacuum and ambient oxygen Applied *Appl Phys Lett* Vol 60 No 22 Page 2732
Gohill *et al*, 1986	Gohill, P , Kaufman, V and McIlrath, T J 1986 High-resolution spectra of laser plasma light sources in the grazing incidence region *Applied Optics* Vol 25, No 13
Goodrich and Wiley, 1962	Goodrich, G W and Wiley, W C 1962 Continuous channel electron multiplier *Rev Sci Instr* Vol 33 Page 761
Gupta, 1993	Gupta, A 1993 Gas-phase oxidation chemistry during pulsed laser deposition of YBa₂Cu₃O₇ δ films *J Appl Phys* Vol 73 No 11 Page 7877
Hickman, 1996	Hickman, I 1996 Working with avalanche transistors *Electronics World* Issue March 1996 Page 219
Hill III, 1985	Hill III, W T 1985 Non-resonant laser-driven ionization of condensing vapours A mechanism based on cluster fragmentation *Optics Communications* Vol 54 No 5 Page 283
Hill III, 1986	Hill III, W T 1986 Quenching of resonant laser-driven ionization at high buffer gas pressures *J Phys B At Mol Phys* Vol 19 Page 359
Howes and Morgan, 1985	Howes, M J and Morgan, D V 1985 *Charge-coupled devices and systems* University of Leeds Wiley-Interscience Publications
Hughes, 1975	Hughes, T P 1975 *Plasmas and laser light* Edition Adam Hilger
Hunter *et al*, 1985	Hunter, E P L , Simic, M G and Michael, B D 1985 Use of an optical multichannel analyzer for recording spectra of short-lived transients *Rev of Sci Instrum.* Vol 56, No 12, Page 2199
Janesick *et al*, 1985	Janesick, J , Elliot, T , Daud, T , McCarthy, J and Blouke, M 1985 Backside charging of the CCD *Proceedings SPIE* Vol 570, Page 46-80
Jannitti *et al*, 1985	Jannitti, E , Mazzoni, M , Nicolosi, P , Tondello, G and Yongchang, W 1985 Photoabsorption spectrum of Be⁺ *Journal of the Optical Society of America B* Vol 2, Page 1078
Janmtti *et al*, 1986	Jannitti, E , Pinzhong, F and Tondello, G 1986 The absorption spectrum of B II in the vacuum ultraviolet *Physica Scripta* Vol 33, Pages 434-441
Kelly, 1987	Kelly R L 1987 Atomic and ionic spectrum lines below 2000 Angstroms Hydrogen through Krypton. *J. of Physics & Chemical Reference Data* Vol 16, No 1
Kennedy *et al*, 1996	Kennedy, E T , Costello, J T and Mosnier, J P 1996 New experiments in photoabsorption studies of singly and multiply charged ions *Journal of Electron*

	Spectroscopy and Related Phenomena Vol 79, Pages 283-288
Kent *et al*, 1987	Kent L W J , Connerade J P , and Thorne A P 1987 The 5p absorption spectrum of laser-excited barium *J Phys B At Mol Phys* Vol 20, Page 2947
Kieffer and Chaker, 1994	Kieffer, J C and Chaker, M 1994 X-Ray Sources Based on Subpicosecond-Laser-Produced Plasmas *Journal of X-Ray Science and Technology* Vol 4 Page 312
Koog *et al*, 1996	Koog, J , Iwasaki, K , Sato, K , Hamada, Y , Toi, K and the JIPP T-IIU Group 1996 Development of an imaging vacuum-ultraviolet monochromator in the normal incidence region *Rev Sci Instrum.* Vol 67, No 11, Page 3871
Kuhne and Wende, 1985	Kuhne, M and Wende, B 1985 Vacuum uv and soft x-ray radiometry Review article *The institute of Physics* 0022-3735/85/080636 Page 637
Kuhne, 1982	Kuhne, M 1982 Radiometric comparison of a laser-produced plasma and BRV-source plasma at normal incidence *Applied Optics* Vol 21, No 12, Page 2124
Lai and Cerrina, 1986	Lai, B and Cerrina, F 1986 *Nucl Istrum Methods Phys Res A* Vol 266, Page 337
Lai *et al*, 1988	Lai, B Chapman, K and Cerrina, F 1988 *Nucl Instrum Methods Phys Res A* Vol 266, Page 544
Lerner and Therenon, 1988	Lerner, J M and Thevenon, A 1988 *The Optics of Spectroscopy A tutorial V 2 0* Edition 2 Jobin Yvon Optical Systems Instruments SA http //www [Accessed date 8/12/96]
Lucatorto and McIlrath, 1980	Lucatorto T B and McIlarth T J 1980 Laser excitation and ionization of dense atomic vapours *Applied optics* Vol 19, No 23, Page 3948
Lucatorto *et al*, 1979	Lucatorto, T B , McIlrath, T J and Roberts, J R 1979 Capillary array a new type of window for the vacuum ultraviolet *Applied Optics* Vol 18, No 14, Page 2505
Luppi *et al*, 1984	Luppi, R , Pecorella, F and Cerioni, I 1984 Pulsed microchannel-plate mounting for subnanosecond x-ray image intensifiers *Rev Sci Instrum.* Vol 55, No 12, Page 2034
Maiman, 1960	Maiman, T H 1960 Stimulated optical radiation in Ruby *Nature* Vol 187, Page 493
Meighan *et al*, 1997	Meighan, O , Costello, J T Lewis, C L S and MacPhee, A 1997 Short-pulse, extreme-ultraviolet continuum emission from a table-top laser plasma light source *Appl Phys Lett* Vol 70, No 12, Page 1497
Mizushima and Okamoto, 1967	Mizushima Y and Okamoto Y 1967 Properties of Avalanche Injection and it's Applications to Fast Pulse Generation and Switching *IEEE Transactions on Electron Devices* Vol 14, No 3, Page 146
Nagel *et al*, 1984	Nagel, D J Brown, C M , Peckerar, M C , Ginter, M L , Robinson, J A , McIlrath, J T and Carroll, P K 1984 Repetivity pulsed-plasma soft X-ray source *Applied*

	Optics Vol 23, No 9, Page 1428
Namioka, 1959	Namioka, T 1959 Theory of the concave grating I *J of the Opt Soc of America* Vol 49, No 5, Page 446
Namioka, 1961	Namioka, T J 1961 *Opt Soc Of America* Vol 51 Page 4
NSRDS-NBS 60	*Atomic Energy Levels The Rare-Earth Elements* U S Department of Commerce / National Bureau of Standards NSRDS-NBS 60
O'Sullivan, 1983	O'Sullivan, G 1983 The origin of line free X-UV continuum emission from laser produced plasmas of the elements $62 \leq Z \leq 74$ *J Physics B Atomic and Molecular Physics* Vol 16, Pages 3291-3304
Ohchi et al, 1996	Ohchi, T , Aoki, S and Sugisaki, K 1996 Micro x-ray photoelectron spectroscopy of the laser ablated silicon surface with laser-produced plasma x-ray source *Journal of electron spectroscopy and related phenomena* Vol 80, Pages 37-40
Orth et al, 1986	Orth, F B , Ueda, K , McIlrath, T J and Ginter, M L 1986 High-resolution spectra of laser plasma light sources in the normal incidence XUV region *Applied Optics* Vol 25, No 13
Oshephov et al, 1960	Oshephov, P K , Skvortsov, B N , Osanov, B A and Siprikov, I V 1960 *Pribory Tekh Eksper* Vol 4, Page 89
Photometrics™	Photometrics Ltd™ Image intensifiers Photek http // www photomet com/ref/ref backCCD html [Accessed date 03/06/97]
Reader et al	Reader, J , Caliss, C H *Wavelengths and transition probabilities for Atoms and Atomic Ions Part I Wavelengths* Centre for Radiation Research National Measurement Laboratory National Bureau of Standards Washington DC 20234
Rose et al, 1978	Rose, S J , Pyper, N C , and Grant, I P 1978 *J Phys B At Mol Phys* Vol 11, Page 755
Ryden, 1993	Ryden, A 1993 *Installation of a 1 meter normal incidence spectrometer for spectroscopic diagnostics of laser produced plasmas* M Sc Thesis DCU Unpublished
Samson, 1967	Samson, J A R 1967 Techniques of VUV spectroscopy Wiley-Interscience New York
Schawlow and Townes, 1958	Schawlow, A L and Townes, C H 1958 Infrared and optical masers Physical Review Vol 112, No 6, Page 1940
Shadow User's Guide, 1994	Shadow User's Guide 1994 Centre for X-ray Lithography, University of Wisconsin USA
Shevelko and Vainshtein, 1993	Shevelko, V P and Vainshtein, L A 1993 *Atomic physics for hot plasmas* Institute of Physics Publishing The Russian Academy of Sciences, Moscow, Russia
Steingruber et al, 1996	Steingruber, J , Borgstrom, S , Starczewski, T and Latzen, U 1996 Prepulse dependence of X-Ray emission from plasmas created by IR femtosecond laser pulses on

	solids *J Phys B At Mol Opt Phys* Vol 29 Page L75
Tang *et al*, 1991	Tang, Z , Xu, Z and Kevan, S 1991 A normal incidence vacuum ultrviolet emission spectrometer Rev Sci Instrum Vol 63 No 3 Page 1896
Tebo, 1994	Tebo, A 1994 Kumakhov optics provide new way to deal with x-rays SPIE Available from http //www spie org/web/oer/november/kumakhov html [Accessed date 8/12/96]
Teubner *et al*, 1992	Teubner, U , Kuhnle, G and Schafer, F P 1992 Detailed Study of the Effect of a Short Prepulse on Soft X-Ray Spectra Generated by a High-Intensity KrF Laser Pulse *Appl Phys B* Vol 54 Page 493
Thomas *et al*, 1994	Thomas, S , Shimkunas, A R and Mauger, P E 1994 Sub-nanosecond intensifier gating using heavy and mesh cathode underlays http //www-dsed llnl gov/documents/diags/stspie90A html [Accessed date 04/02/96]
Tom and Wood, 1988	Tom, H W K and Wood, O R 1989 *Appl Phys Lett* Vol 54, No 6, Page 517
Tracy, 1977	Tracy, D H 1977 Photoabsorption structure in lanthanides 5p subshell spectra of Sm I, Eu I, Dy I, Ho I, Er I, Tm I and Yb I *Proc R Soc Lond A* Vol 357, Page 485
Wiese *et al*	Wiese, W L and Martin, G A *Wavelengths and transition probabilities for Atoms and Atomic Ions Part I Wavelengths* Centre for Radiation Research National Measurement Laboratory National Bureau of Standards Washington DC 20234
Wiese, 1993	Wiese, W L 1993 *Atomic spectroscopic databases* Edition Place of publication Elsevier Science Publishers B V
Wilkins *et al*, 1989	Wilkins, S W , Stevenson, A W , Nugent, K A , Chapman, H and Steenstrup, S 1989 On the concentration, focusing, and collimation of x-rays and neutrons using microchannel plates and configurations of holes *Rev Sci Instruments* Vol 60, No 6, Page 1026
Wiza, 1979	Wiza, J L 1979 Microchannel plate detectors *Nuc Instr and Methods* Vol 162, Page 587
Wuilleumier, 1992	Wuilleumier, F J 1992 Photoionization of atomic ions In Proceedings, International conference on atomic spectroscopy
Zetex Semiconductors™, 1996	Zetex Semiconductors™ http //www zetex co uk [Accessed date 20/03/96]

Appendix I Acton™ VM-521 1 metre normal incidence spectrometer specifications

Model   VM - 521

Focal length   0 9954 m

Optical system   Near normal incidence 7 5 ° / 7 5 °

Horizontal aperture ratio   F / 10 4 with 96 mm wide grating

Grating

    Manufacturer   Bausch & Lomb

    Type   Concave reflective

    Grooves mm [1]   1200

    Concave radius   995 4 mm

    Coating   Iridium

    Blaze angle   2 75 °

    Blaze wavelength   80 nm (First order)

    Ruled width   96 mm

    Ruled height   56 mm

    Wavelength range   30 - 325 nm (Max mechanical movement)

Resolution capability   0 014 nm (Entrance and exit slit width 10 µm)

Reciprocal linear dispersion   0 83 nm mm [1]

Nominal wavelength coverage   ~ 21 nm for both CEMA / PDA and back thinned

                          CCD based detectors

Wavelength accuracy   ± 0 05 nm (mechanical mount movement)

Wavelength reproducibility   ± 0 005 nm (mechanical mount movement)

Scanning mechanism   Sine drive mechanism with precision lead

                          screw external to the vacuum system

Focusing   Cam controlled translation motion with

                          Micrometer adjustments external to vacuum

system for both short and long wavelength focus adjustments Long

wavelength adjustment micrometer closest to spectral drive

Micrometer settings for Galileo™ CEMA and Andor™ back thinned

CCD detector using present flanges
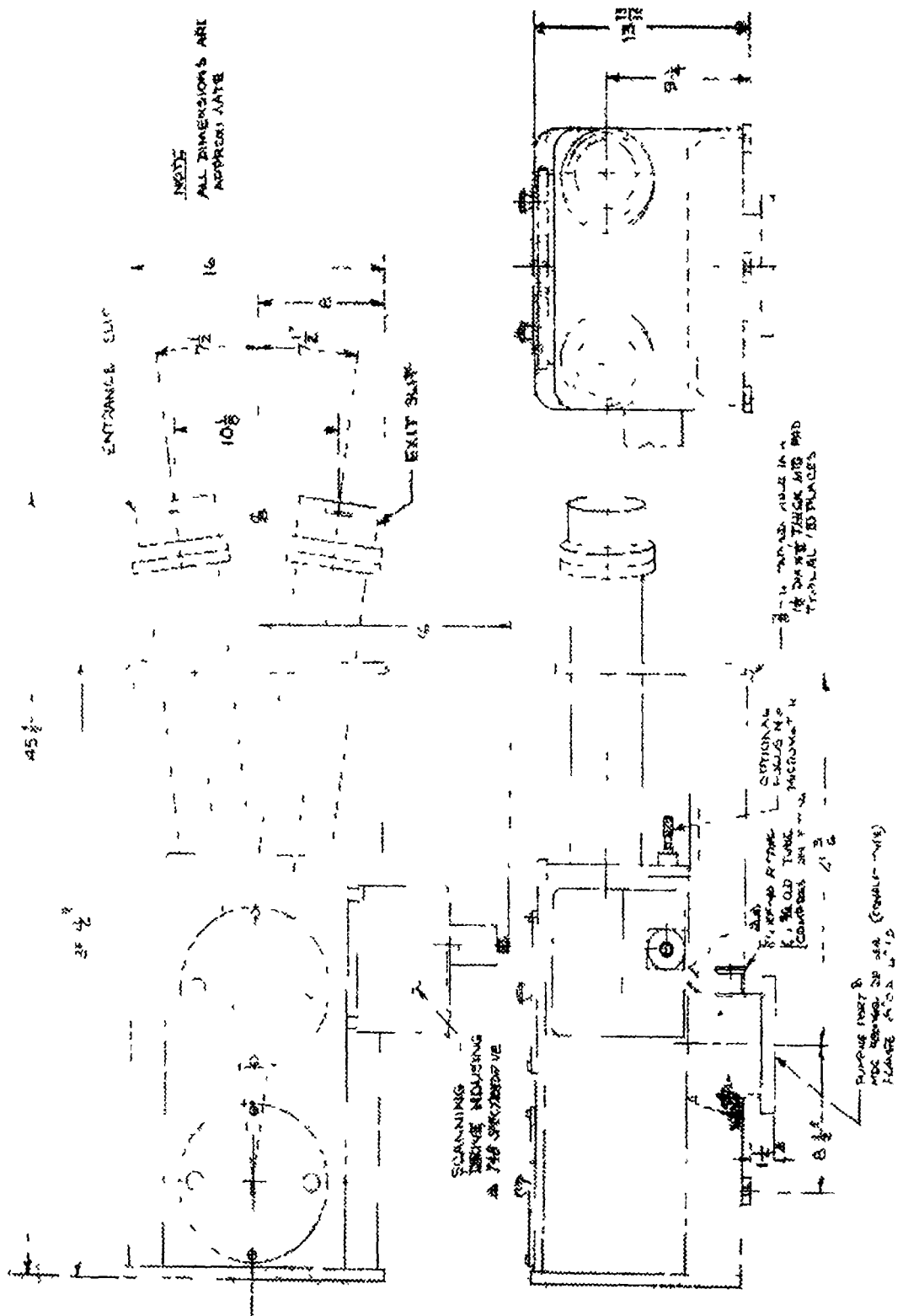
Short wavelength 2 21

Long wavelength 1 85

Figure AI-1   Schematic of Acton™ VM-521 normal incidence spectrometer showing approximate external dimensions in inches

A-2

Appendix II. EG&G™ photo diode array (PDA) detector specifications[†]

PDA model	1453A
Interface model	1471A.
Detector type	Silicon photodiode array
	Silicon behind fused silica face plate
Wavelength range	180 nm to 1100 nm
Quantum efficiency	70 % @ 650 nm
Gain	1350 photo electrons / count
Sensitivity	1960 photons / count @ 550 nm
Maximum deviation from linear response	1 %
Dynamic range	32768 @ 15 - bit
Uniformity of sensitivity	± 5 %
Maximum geometric distortion	1 channel
Line width	2 channels FWHM
Array length	25 mm
Pixel number and array size	1024 pixels, 25 6 mm * 2 5 mm
Centre to centre spacing	25 μm
Dark current in counts	1024 (800 ms @ 5 °C)
	120 (1 s @ - 20 °C)
Maximum system noise	1 5 (counts / scan)$^{1/2}$
Temperature range	- 40 °C to 18 °C
Gas requirements	Must be flushed with dry nitrogen for temperatures lower than room temperature during operation and after operation until detector system has reached room temperature

[†] Specifications taken from 'Models 1452, 1453, and 1454 silicon photodiode detectors" Operating and service manual E G & G Princeton Applied Research

Appendix III Andor Technology™ back thinned CCD specifications.

CCD head model	DH 425 -V
Serial number	CCD - 359
Array number	1024 * 256
Pixel size	26 μm^2
Thermal electric cooling	3 - stage
Controller card	CC100 (1 MHz)
A/D resolution	16 - bit
Readout speed	1, 2, 16, 32 us per pixel

Readout noise

A/D rate	R/S	CCD gain	Single pixel	Full vertical binning
1 MHz	1 μs	10	40	40 6
500 kHz	2 μs	10	38	37 9
62 kHz	16 μs	10	8 4	9 1
31 kHz	32 μs	5	6 4	7 7

Base mean level

A/D rate	R/S	Counts
1 MHz	1 μs	555
500 kHz	2 μs	460
62 kHz	16 μs	210
31 kHz	32 μs	234

CCD dark current	Please refer to user manual for graph
Minimum dark current achievable	0 37 @ -54 3 °C with 12 °C water cooling
CCD dark current uniformity	Better than 0 07 electrons / pixel / sec
Linearity	Better than 1 % over 16 bits
Response uniformity	Better than 3 3 %
Dark current defects	No hot spots

Response defects (Dark pixels)

335,30	841,158
164,32	315,162
710,36	862,172
30,80	740,197
866,147	542,223
864,154	

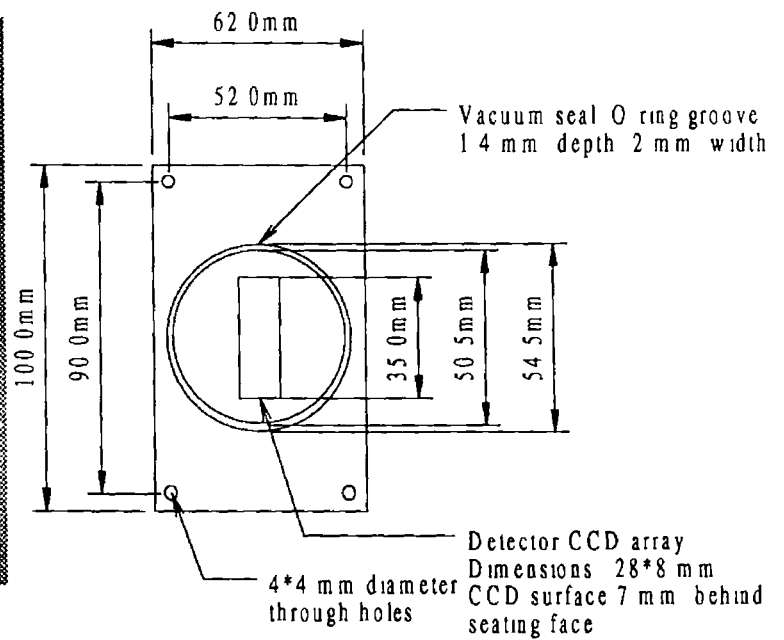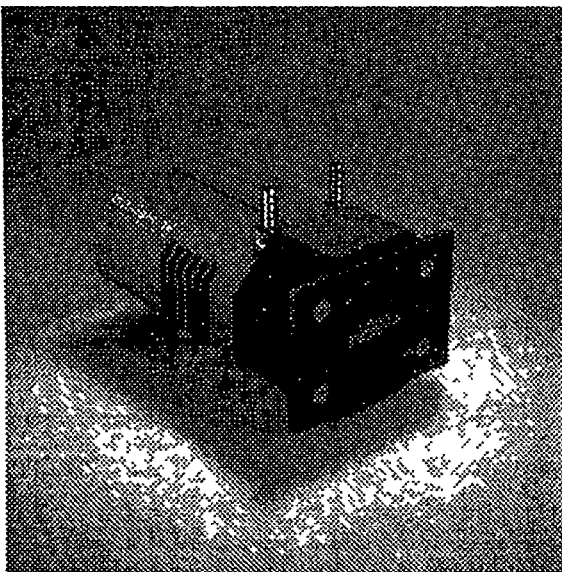|	
Power supply unit	PS 150
Multi I/O box	IO 159
CCD chip	EEV CCD30 - 11
CCD chip serial number	A4593 - 13 - 11
Format	Back illuminated
Coating	None

Figure A III-1   *(a) Andor Technology™ back thinned CCD and (b) drawing*
showing main dimensions of front flange

Appendix IV Galileo™ Channel Electron Multiplier Array (CEMA) specifications

|	
MCP model	Galileo 6025 - FM MCP
Plate outside diameter	32 74 mm
Plate thickness	0 43 mm
Active area	4 9 cm^2
Electrode material	Inconal or nichrome
Pore size	10 µm
Centre to centre spacing	12 µm
Open area ratio	55 %
Bias angle	12 °
Solid glass border	Yes
Minimum electron gain	3 3 * 10^4
MCP / phosphor gap distance	1 2 mm
Bias current	4 * 10^{16} µAmps per plate
Maximum linear output density	10 % of bias current density
Fibre optic phosphor	P20
Coating	MgF$_2$ Magnesium fluoride
Maximum bakeable temperature	350 °C
VUV wavelength range (detection efficiency > 10 %)	20 - 180 nm
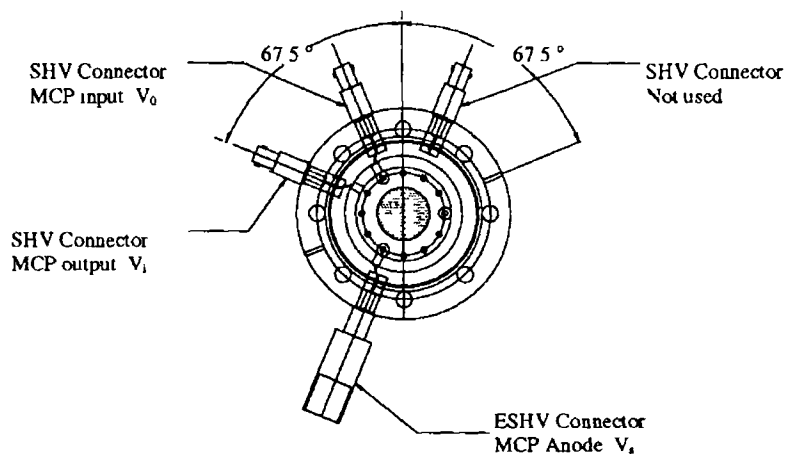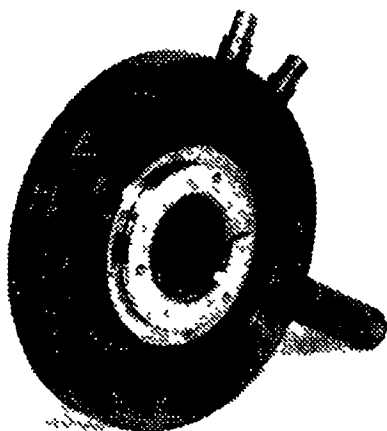
Figure A IV-1 (a) Galileo™ CEMA and (b) vacuum assembly showing position of feedthroughs with vacuum side showing

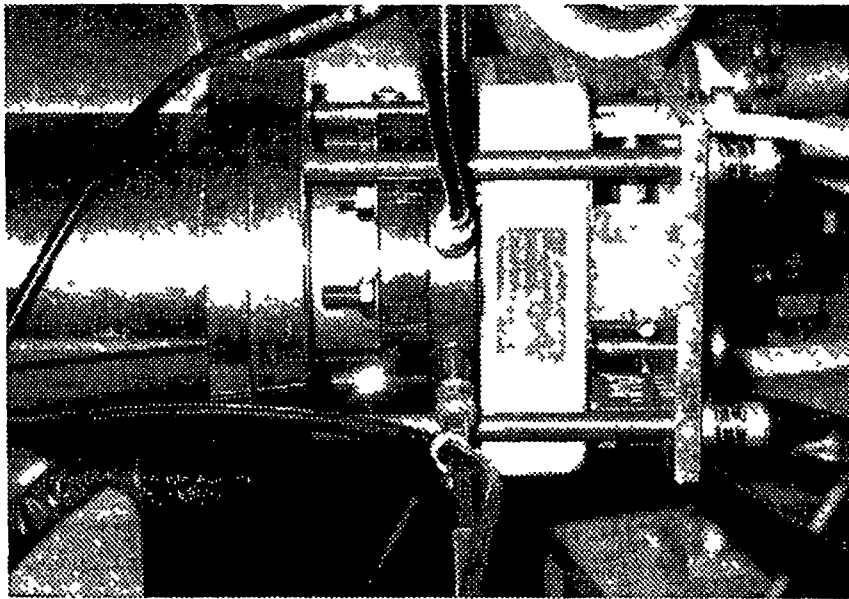## Appendix V. Galileo™ glass capillary array (GCA) specifications.

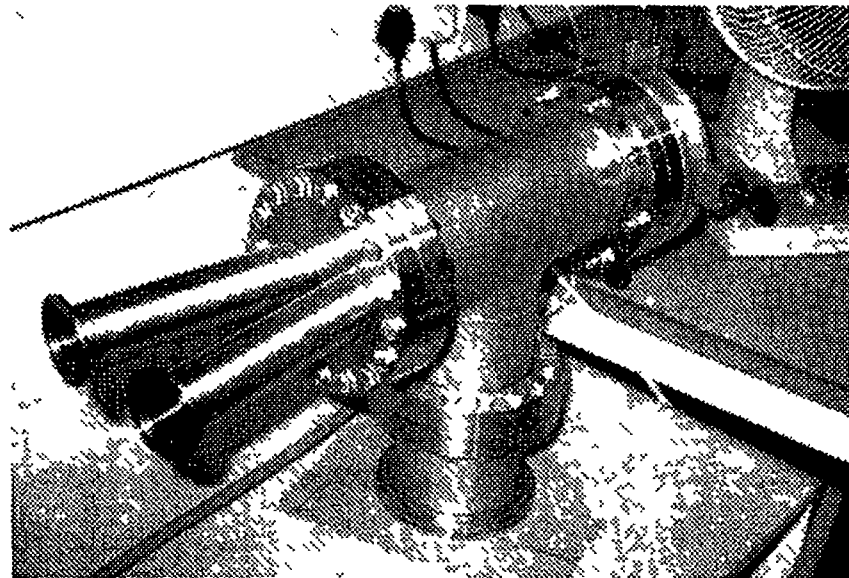|	
Individual pore size	50 μm diameter
Percentage open area	60 %
Thickness	3 mm
Diameter	25 mm
Glass material	Soda lime glass

Appendix VI. Photographs of system.
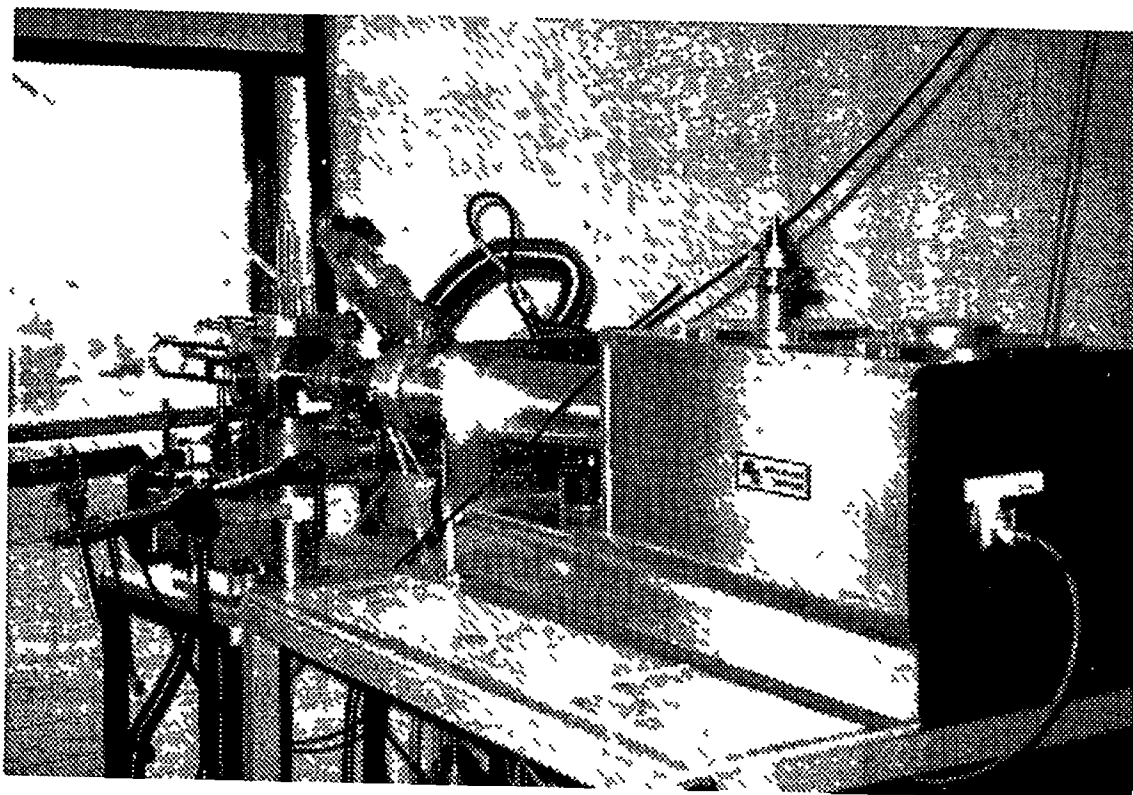
Figure AIX-1   *Photograph showing system configuration used in helium gas photoabsorption and barium photoabsorption*

Figure AIX-3
CEMA / PDA detector
arrangement

Figure AIX-4
(a) Mirror chamber
showing 40KF flanges at
15 ° and (b) mirror
holder and positioner for
both focusing and angle
alignment